MASTER COPY - FOR REPRODUCTION PURPOSES (2)

AD-A214 246

DTIC ELECTE NOV 02 1989 B

REPORT DOCUMENTATION PAGE

1b. RESTRICTIVE MARKINGS	
2a. SECURITY CLASSIFICATION AUTHORITY	3. DISTRIBUTION/AVAILABILITY OF REPORT
2b. DECLASSIFICATION/DOWNGRADING SCHEDULE	Approved for public release; distribution unlimited.
4. PERFORMING ORGANIZATION REPORT NUMBER(S)	5. MONITORING ORGANIZATION REPORT NUMBER(S) ARO 24007.8-PH
6a. NAME OF PERFORMING ORGANIZATION: Lehigh University	6b. OFFICE SYMBOL (If applicable)
7a. NAME OF MONITORING ORGANIZATION: U. S. Army Research Office	
6c. ADDRESS (City, State, and ZIP Code): Bethlehem, PA 18015	7b. ADDRESS (City, State, and ZIP Code): P. O. Box 12211, Research Triangle Park, NC 27709-2211
8a. NAME OF FUNDING/SPONSORING ORGANIZATION: U. S. Army Research Office	8b. OFFICE SYMBOL (If applicable)
9. PROCUREMENT INSTRUMENT IDENTIFICATION NUMBER: DAAL03-86-K-0161	
8c. ADDRESS (City, State, and ZIP Code): P. O. Box 12211, Research Triangle Park, NC 27709-2211	10. SOURCE OF FUNDING NUMBERS

PROGRAM ELEMENT NO.	PROJECT NO.	TASK NO.	WORK UNIT ACCESSION NO.

11. TITLE (Include Security Classification): Excimer Emission From Alkali Diatomic and Alkaline-Earth-Noble-Gas Molecules

12 PERSONAL AUTHOR(S): John P. Huennekens

13a. TYPE OF REPORT	13b. TIME COVERED	14. DATE OF REPORT (Year, Month, Day)	15. PAGE COUNT
Final	FROM 9/1/86 TO 8/31/89	October 1989	

16. SUPPLEMENTARY NOTATION: The view, opinions and/or findings contained in this report are those of the author(s) and should not be construed as an official Department of the Army position, policy, or decision, unless so designated by other documentation.

17. COSATI CODES		
FIELD	GROUP	SUB-GROUP

18. SUBJECT TERMS (Continue on reverse if necessary and identify by block number): Coherent Light Sources, Atomic Systems, Molecular Systems, Lasers, High-Power Lasers, Alkaline-Earth Molecules, Alkaline-Earth Atoms

19. ABSTRACT (Continue on reverse if necessary and identify by block number)

Experimental studies involving the interaction of high-power lasers with alkali and alkaline-earth atoms and molecules have been carried out. The motivation for this work has been to evaluate proposed methods for using these systems to create tunable coherent light sources in the near-infrared spectral region. In addition, much fundamental information has been obtained about these atomic and molecular systems, and on their interactions with light. The work can be divided into three areas: studies of bound-free triplet emission from alkali molecules, studies of wave-mixing processes, and experiments on barium-noble-gas mixtures. In addition, several smaller projects were carried out in closely related fields.

20. DISTRIBUTION/AVAILABILITY OF ABSTRACT	21. ABSTRACT SECURITY CLASSIFICATION
☐ UNCLASSIFIED/UNLIMITED ☐ SAME AS RPT. ☐ DTIC USERS	Unclassified
22a. NAME OF RESPONSIBLE INDIVIDUAL	22b. TELEPHONE (Include Area Code) / 22c. OFFICE SYMBOL

DD FORM 1473, 84 MAR — 83 APR edition may be used until exhausted. All other editions are obsolete.

SECURITY CLASSIFICATION OF THIS PAGE: UNCLASSIFIED

89 10 30 132

ARO 24007.8-PH

Final Report - ARO grant DAAL03-86-K-0161

During the past three years, we have carried out experimental studies involving the interaction of high-power lasers with alkali and alkaline-earth atoms and molecules. The motivation for this work has been to evaluate proposed methods for using these systems to create tunable coherent light sources in the near-infrared spectral region. In addition, we have obtained much fundamental information about these atomic and molecular systems, and on their interactions with light. Our work, during this time period, can be divided into three areas: studies of bound-free triplet emission from alkali molecules, studies of wave-mixing processes, and experiments on barium - noble-gas mixtures. In addition, we have carried out several smaller projects in closely related fields. We will describe each of these projects in the following paragraphs and in the attached appendices.

The lowest triplet state of all alkali diatomic molecules is of $^3\Sigma^+$ symmetry, and is repulsive except for a shallow van der Waals minimum at large internuclear separation. Because of this unbound nature, emissions to the $^3\Sigma^+$ state form true continua, which may eventually form the basis for continuously tunable near-infrared lasers. We have focussed our attentions on the lowest triplet band, $1^3\Pi \rightarrow 1^3\Sigma^+$, of the heteronuclear molecule NaK, which we have studied in the range 1.0 to 1.6 μm. Alkali triplet bands have, in general, been difficult to study, due to the dipole selection rule on spin, $\Delta S = 0$, and the fact that the ground state is a singlet. In the present case, we have populated the $1^3\Pi$ state of NaK by taking advantage of spin-orbit induced perturbations between levels of the $1^3\Pi$ and those of the nearby $2^1\Sigma^+$ state. Such perturbations mix nearly degenerate singlet and triplet levels with the same J value. This results in certain levels having both singlet and triplet amplitudes, allowing radiative coupling to both the ground ($1^1\Sigma^+$) and repulsive $1^3\Sigma^+$ states. The resulting bound-free triplet emission appears in the form of an oscillating continuum in the near-infrared. The oscillations can be shown to relate directly to the square of the vibrational wavefunction in the bound upper state, and thus represent one of the clearest

demonstrations of the wave-nature of matter. Bound-free emission spectra of this type are described in detail in Appendix 1 of this report.

Using a narrow-band, single-mode cw ring dye laser as a pump source, we were able to selectively populate single ro-vibrational levels of the upper $1^3\Pi$ state. The specific level could be accurately identified by analysis of the associated singlet spectrum. Since the bound $1^1\Sigma^+$, $1^3\Pi$, and $2^1\Sigma^+$ states of NaK have previously all been accurately characterized by Fourier-transform spectroscopy, we could carry out fully quantum-mechanical simulations of the oscillatory bound-free triplet emission produced by each upper ro-vibrational level. The lower repulsive triplet state in these simulations was represented by an exponential function with two free parameters. These parameters were varied to give a good match between the positions of the intensity maxima and minima in the experimental and theoretical spectra. In this way, we were able to obtain an accurate mapping of the $1^3\Sigma^+$ repulsive wall. Note that bound states have been accurately mapped for many years by fitting the positions of hundreds or thousands of discrete lines. Repulsive states, which are important in scattering, dissociation processes, and as the lower level in excimer lasers, have proven difficult to map since their emission tends to form relatively featureless continua. However, the bound-free emission which can be produced from selective excitation of particular ro-vibrational levels of the upper state, produces tens or hundreds of intensity maxima and minima which can be fit to yield the potential. Thus we can now map some of the repulsive states with an accuracy approaching that with which bound states can be obtained. In addition, the relative intensities of the maxima allow a fitting of the transition dipole moment as a function of internuclear separation. Our work on the determination of the $1^3\Sigma^+$ state potential, and on the $1^3\Pi \rightarrow 1^3\Sigma^+$ transition dipole moment are described in Appendix 2 which is a manuscript being prepared for submission to the Journal of Chemical Physics.

We have carried out gain calculations on this NaK $1^3\Pi \rightarrow 1^3\Sigma^+$ band which show that this bound-free emission may be a good candidate for tunable laser applications. Unfortunately, these calculations cannot take into account absorption to higher lying states, about which little is known. We have measured the gain at 1.15 μm, using a helium-neon laser, and found net

absorption at this wavelength. However, we hope to extend these gain measurements to other wavelength regions (around 1.3 μm) using a tunable diode laser. We also plan to study in detail the heavier heteronuclear molecule RbCs, in which the spin-orbit interactions should be much stronger, thus improving access to the triplet manifold.

A second area of interest for us has been the generation of coherent light in the near-IR through non-linear wave-mixing processes. When potassium vapor is excited with a high-power pulsed laser tuned near the 4S → 6S two-photon transition frequency, a very intense violet beam (λ = 404 nm) is generated in the forward direction. This strong coherent emission can be shown to be a four-wave mixing process. Under the same conditions, several other coherent emissions in the near-infrared region can also be observed. Most of these occur at or near the wavelengths of allowed atomic transitions, and are due to a combination of amplified spontaneous emission (resulting from real population inversions) and various wave-mixing processes. A particularly interesting set of processes involves the production of coherent emission at 1.28 and 1.37 μm (which do not correspond to any known potassium atomic transitions). These processes can be shown to be due to six-wave mixing following the scheme: $\omega_{1.28(1.37)} = 2\,\omega_{laser} - [\omega_{6S\rightarrow 5P} + \omega_{5P\rightarrow 3D(5P\rightarrow 5S)} + \omega_{laser}]$. We are currently setting up an experiment, in which two lasers will be used, to demonstrate that this coherent near-infrared emission can be made broadly tunable. Our work in this area is described more completely in Appendices 3 and 4.

An even more intriguing process was observed in mixed sodium-potassium vapors when the laser was detuned considerably from the 4S → 6S potassium two-photon transition. Again we observed coherent emission in the forward direction, corresponding to the potassium $3D_{3/2} \rightarrow 3P_{1/2}$ transition. However, under these circumstances, no other coherent emissions were observed. Surprisingly, this emission was observed only on the weaker component of the fine-structure doublet. Additionally, it could not be observed in pure potassium vapor. We believe the emission involves a two-step photodissociation of the NaK molecule, where the final unbound state dissociates to the Na(3S) + K($3D_{3/2}$) limit. It is known that such photodissociation processes can be highly selective in terms of final state

fine-structure level. Still, we do not understand the forward-backward asymmetry (~25:1), or the observed fact that the coherent emission temporally follows the pump laser pulse. Our work in this area is detailed in Appendices 3 and 4. We are hoping to resolve some of the remaining questions with a set of two-laser experiments planned for the near future.

A side note to this work with the sodium-potassium mixtures involves the observation of NaK $2^1\Sigma^+ \rightarrow 1^1\Sigma^+$ band stimulated emission near 1.02 μm. This "A band" optically-pumped laser (OPL) is similar to analogous stimulated processes which have been demonstrated in the homonuclear alkali diatomics over the last several years. However, the present case is the first demonstration of OPL emission in NaK, and only the second reported case involving a heteronuclear alkali molecule. In addition, these observations extend the range of known alkali OPL emission into the 1 μm region. Our results are reported in Appendix 5.

Finally, we report one other experimental result that falls in the category of "wave-mixing". This involves the intriguing 830 nm emission observed in sodium vapor excited at the 3S → 4D two-photon transition wavelength. This emission was first reported in 1984 by Dinev and coworkers, who attributed it to stimulated emission on the Na_2 $1^3\Sigma_g^+ \rightarrow 1^3\Sigma_u^+$ band. Another coherent emission at 840 nm, found under the same conditions, was assigned to a higher step of a molecular cascade process. The identification was based on the fact that no other sodium atomic or molecular transitions were known to produce radiation in this wavelength region. In 1987, Wellegehausen and coworkers demonstrated that the 840 nm emission was actually a six-wave mixing process similar to the potassium 1.28 and 1.37 μm emissions discussed above. However, their data did not yield any conclusive information on the origin of the 830 nm emission. Nevertheless, they concluded that it was probably another atomic parametric process. Most recently (Dec. 1988), Bajic et. al. presented new data on the 830 nm emission and concluded that it was indeed stimulated excimer emission on the $1^3\Sigma_g^+ \rightarrow 1^3\Sigma_u^+$ band of Na_2. Since the discussion of this interesting process seemed not yet settled, and since the possibility of stimulated emission on the alkali triplet excimer bands was central to our studies under this grant, we began an experiment to establish

the identity of the 830 nm emission once and for all. Recently, we submitted a manuscript to Applied Physics B (Appendix 6) which contains our findings. We have now definitely identified the 830 nm emission as an example of a recently discovered type of wave-mixing process called axially-phase-matched six-wave mixing. In this process, the photons all propogate along the pump laser axis, which maximizes the spatial overlap of the various beams. The vector phase-matching (momentum conservation) equation then reduces to a scalar equation involving only the magnitudes of the various photon wave vectors. In order to satisfy both the momentum and energy conservation equations, the photon frequencies must then adjust themselves to values that can be calculated easily using simple equations. The predicted positions agree well with our observations. The final piece of evidence, which solidified the identification, was the observation of a predicted shift of the 830 nm emission peak to 825 nm when potassium was added to the vapor. The effect of the potassium is to change the index of refraction of the vapor, and thus to change the wavelength which satisfies the phase-matching condition.

Recently, we have begun a new experiment to study the population and depopulation of various excited levels of barium following pulsed laser excitation. Ultimately, we are interested in studying collision-induced far-wing emission on the barium $^3D_J \rightarrow {}^1S_0$ and $^1D_2 \rightarrow {}^1S_0$ forbidden transitions. The metastable D states can be populated efficiently by stimulated Raman processes such as $^1S_0 \rightarrow {}^3P_1 \rightarrow {}^3D_2$. Since there are no allowed radiative decay channels for the final D states, they have very long lifetimes. Eventually, they either decay by quasi-molecular emission induced in collisions with inert buffer gas atoms, are quenched in collisions with impurities, or escape by diffusion. Since the collision-induced emission of interest is expected to be quite weak, it is important to maximize the population in the metastable levels. Therefore, our first project is to develop techniques for monitoring the various level populations in a time-resolved mode. Once this is accomplished, we will be able to maximize these populations by optimizing the pressure, temperature, pump laser power, and laser wavelength.

The population monitoring is accomplished by scanning a single-mode cw laser across an absorption line originating in the state of interest. Using

a transient digitizer or boxcar averager, we can map the full absorption lineshape in a time-resolved mode. Spatial information can also be obtained by moving the probe laser beam with respect to the pulsed pump laser beam. However, difficulties arise in trying to deal with hyperfine structure and the low ionization threshold of barium. We are currently working to incorporate such processes into our model in order to turn this method into a reliable technique for studying the kinetics of this laser excited metal vapor system.

Finally, we carried out an experiment to measure the cross-section for the excitation transfer process, $Cs(5D_{5/2}) + Cs(6S_{1/2}) \rightarrow Cs(5D_{3/2}) + Cs(6S_{1/2})$. Most of the experimental work on this side project was carried out by an undergraduate research participant, Ms. Beta Keramati, who is now in the graduate program at Temple University. The experiment involved pumping the cesium forbidden transition $6S_{1/2} \rightarrow 5D_{5/2}$ with a cw dye laser and then monitoring the cascade fluorescence on the two fine-structure transitions $6P_J \rightarrow 6S_{1/2}$. Since the $5D_{5/2}$ state radiates exclusively to $6P_{3/2}$, only $6P_{3/2} \rightarrow 6S_{1/2}$ fluorescence is observed in the absence of collisional mixing. As the excitation transfer collisions increase in number, more and more $6P_{1/2} \rightarrow 6S_{1/2}$ fluorescence is seen. However, this mixing can take place in either the 5D or 6P manifold. To separate these two cases, a second experiment was carried out under the same conditions. In this, the $6P_{3/2}$ state was populated by cw diode laser pumping. Thus the mixing which occurred strictly within the 6P manifold could be separated out. This experiment is described fully in Appendix 7.

Publications resulting from ARO grant DAAL03-86-K-0161

J. Huennekens, A. Loza, M. Masters and K. M. Sando, "Near-infrared bound-free emission from the NaK molecule", J. Chem. Phys. 88, 6013 (1988).

B. K. Clark, M. Masters, and J. Huennekens, "Wave-mixing processes in sodium-potassium vapor", in Advances in Laser Science Vol. III, ed. A. C. Tam, J. L. Gole and W. C. Stwalley, (American Institute of Physics, New York, 1988) p. 167-169.

B. Keramati, M. Masters and J. Huennekens, "Excitation-transfer collisions in cesium vapor: $Cs(5D_{5/2}) + Cs(6S_{1/2}) \rightarrow Cs(5D_{3/2}) + Cs(6S_{1/2})$", Phys. Rev. A 38, 4518 (1988).

B. K. Clark, M. Masters and J. Huennekens, "Wave mixing and amplified spontaneous emission in pure potassium and mixed sodium-potassium vapors", Appl. Phys. B 47, 159 (1988).

B. K. Clark, W. T. Luh and J. Huennekens, "NaK $2^1\Sigma^+ \rightarrow 1^1\Sigma^+$ band optically pumped laser near 1.02 μm", Appl. Phys. B 49, 155 (1989).

W. T. Luh, Y. Li, and J. Huennekens, "830 nm emission in sodium vapor", Appl. Phys. B 49, 349 (1989).

M. Masters, J. Huennekens, W. T. Luh, L. Li, A. M. Lyyra, K. Sando, V. Zafiropulos, and W. C. Stwalley, "Bound-free $1^3\Pi \rightarrow 1^3\Sigma^+$ emission from the NaK molecule: determination of the $1^3\Sigma^+$ repulsive wall above the dissociation limit", to be submitted to J. Chem. Phys. (manuscript enclosed as Appendix 2).

List of participating scientific personnel - ARO grant DAAL03-86-K-0161

Postdoctoral Research Associates:

Brian K. Clark
Wei-Tzou Luh

Graduate Research Assistants:

Mark Masters
Zeina Jabbour
Ed Ehrlacher
Yan Li
Ed Rothenheber
Derrick Boucher

Undergraduate Research Assistants:

Kurt Gibble
Andy Loza
Beta Keramati
Jeff Seiple
Gene Diveglia

Near-infrared bound–free emission from the NaK molecule

J. Huennekens, A. Loza,[a] and M. Masters
Lehigh University, Department of Physics, Bethlehem, Pennsylvania 18015

K. M. Sando
University of Iowa, Department of Chemistry, Iowa City, Iowa 52242

(Received 17 November 1987; accepted 3 February 1988)

We report the observation of bound–free emission corresponding to the lowest triplet transition $1\,^3\Pi \rightarrow 1\,^3\Sigma^+$ of the NaK molecule. In the experiment, specific levels of the upper triplet state were populated directly from the ground state by virtue of spin–orbit induced perturbations between the $1\,^3\Pi_0$ and $2\,^1\Sigma^+$ states. Oscillations in the fluorescence spectra between 1.1 and 1.6 μm reflect the probability distribution (wave function squared) in the bound upper state. We have also carried out quantum mechanical simulations of the fluorescence spectra, based on recent *ab initio* calculations of the relevant potential curves. These simulations verify the identification of this near-infrared emission and provide a critical test for the calculated potentials.

I. INTRODUCTION

Alkali diatomic molecules have been of interest both as a testing ground of electronic potential energy curve calculations, and as the active medium in many working and proposed laser designs. In particular, a large number of optically pumped laser (OPL) transitions have been observed in Li_2, Na_2, and K_2.[1–10] Recently OPL transitions have also been observed in the heteronuclear molecule NaRb.[11] In the OPLs, molecules in low-lying thermally populated rovibrational levels of the ground ($1\,^1\Sigma^+$) state are pumped to levels of some electronically excited state (see Fig. 1). Lasing then takes place on transitions down to initially unpopulated high lying levels of the $1\,^1\Sigma^+$ state. Besides offering many new fixed-frequency laser transitions, these OPLs have yielded much useful information about the alkali molecules themselves. However, the OPLs are not continuously tunable due to the discrete nature of the bound–bound transitions.

The lowest triplet state $1\,^3\Sigma^+$, of all alkali molecules is unbound except for a shallow van der Waals minimum at large internuclear separation, R (see Fig. 1). Bound–free emission terminating on this repulsive triplet state should form true continua, and it was suggested in 1980 by Konowalow and Julienne that such emission could be used as a source of continuously tunable near-infrared lasers.[12] Since that time, much attention has been given to alkali triplet bands. These studies include observations of the sodium violet bands,[13–27] the potassium yellow bands,[18–20,28–36] and analogous bands of Li_2,[18,19,37–39] Rb_2,[28,40–42] and Cs_2.[19,28,43–45] It is now known these bands involve transitions to the $1\,^3\Sigma^+$ state from a $^3\Pi$ state which correlates at large R to one ground state atom plus one atom in the lowest D state. Near-infrared transitions to the $1\,^3\Sigma^+$ state from the lowest excited $^3\Sigma$ state have also been studied.[46–53] In recent years, Bahns and Stwalley have reported gain on the Na_2 violet bands,[54] while Wu *et al.* observed enhanced fluorescence along the pump laser axis.[22] Very recently, Wang *et al.* reported the observation of stimulated emission on these Na_2 violet bands.[27] Near-infrared stimulated emission on the Na_2 $1\,^3\Sigma_g^+ \rightarrow 1\,^3\Sigma_u^+$ band was reported by Dinev *et al.*,[55] but Wang *et al.*[56] have recently shown that this emission is actually atomic in nature and relates to various parametric processes.

Experimental observation of alkali triplet bands has, in general, been hindered by the dipole selection rule on spin, $\Delta S = 0$, and the fact that the molecular ground state is a *singlet*. Thus it is not easy to selectively excite the molecule to a specific triplet state. Many of the studies mentioned so far have relied on collisions to populate the upper triplet state. However, collisions are a nonselective population mechanism, so that much spectroscopic detail is lost. On the other hand, accurate spectroscopic constants have been obtained for a number of alkali triplet states in experiments

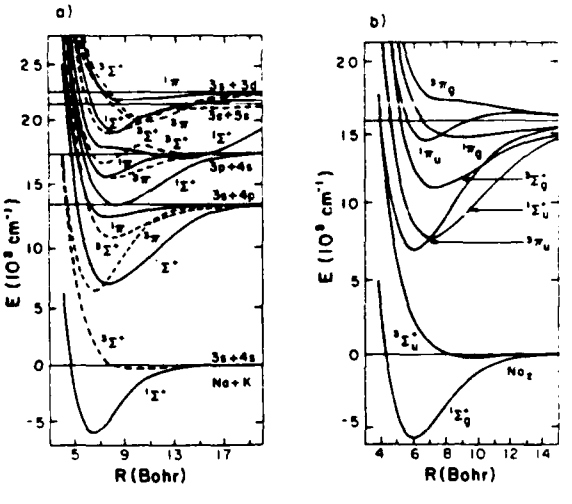

FIG. 1. (a) NaK and (b) Na_2 potential curves taken from Refs. 87 and 112, respectively (figures reproduced with permission from Dr. D. D. Konowalow). Note that throughout the text the notation $2\,^1\Sigma^+$ refers to the second lowest $^1\Sigma^+$ state, etc.

[a] Present address: Department of Physics and Astronomy, University of Pittsburgh, Pittsburgh, PA 15260.

 0021-9606/88/106013-09$02.10

utilizing laser excitation of perturbed or mixed singlet–triplet levels. These mixed levels result from spin–orbit and other types of coupling between nearly degenerate singlet and triplet levels with the same rotational number J. Laser-induced fluorescence experiments involving $2\,^1\Pi$–$2\,^3\Pi$ perturbations in the NaK molecule have yielded important information on the $1\,^3\Sigma^+$ state of that molecule.[57–62] $1\,^1\Sigma_u^+$–$1\,^3\Pi_u$ perturbations in Na_2 and Li_2 have also been studied extensively in recent years.[63–72] Of particular interest is the work of Field and co-workers, who have developed the technique of perturbation-facilitated optical–optical double resonance spectroscopy.[23,73–79] Their work has yielded a wealth of information on many triplet levels of Li_2 and Na_2. These various studies of $1\,^1\Sigma_u^+$–$1\,^3\Pi_u$ perturbations are not only important for the analysis of these states, but provide road maps for gaining access to the triplet manifolds of these molecules.

Ross, Effantin, d'Incan, and Barrow have also taken advantage of singlet–triplet perturbations to gain access to the triplet manifold.[80,81] They and co-workers have obtained accurate spectroscopic constants for various triplet and singlet states by studying bound–bound emission using the techniques of Fourier transform spectroscopy.[80–85] Of direct significance to the present work, they have accurately characterized the NaK $1\,^3\Pi$, $1\,^3\Sigma^+$, and $1\,^1\Sigma^+$ states.[80,81]

In the present work we report bound–free emission corresponding to the NaK $1\,^3\Pi \rightarrow 1\,^1\Sigma^+$ transition (see Fig. 1). This transition was first observed in Ref. 86. However, in that work the upper state was populated through collisions so that most spectroscopic details were washed out. The emission appeared as a featureless continuum that decreased monotonically in intensity as the wavelength increased between 1.1 and 1.6 μm (see Fig. 4 of Ref. 86). Here, we directly populate specific perturbed $1\,^3\Pi$–$2\,^1\Sigma^+$ levels from the $1\,^1\Sigma^+$ ground state (see Fig. 2). We then observe the direct, near-infrared, bound–free emission to the $1\,^1\Sigma^+$ state. The observed spectra consist of a series of oscillations which reflect the probability distribution (wave function squared) in the upper bound state. In this preliminary study, we also present quantum calculations of theoretical spectra based upon recent *ab initio* NaK potential energy curves.[87,88] These calculations verify the proposed explanation of the oscillatory spectra.

We are currently repeating the measurements using single-mode laser excitation. We are also calculating theoretical spectra using the accurate spectroscopic constants for the $1\,^1\Sigma^+$ and $1\,^3\Pi$ states which have been obtained from Fourier transform spectroscopy.[80,81] The idea is to vary parameters of the lower $1\,^3\Sigma^+$ state until we obtain a good match to the observed spectra. Thus we hope to obtain an accurate mapping of the repulsive limb of the $1\,^3\Sigma^+$ state which will smoothly connect to the bound part of the curve obtained in Ref. 81. These results will be presented in a forthcoming publication.[89]

II. THE EXPERIMENT

Figure 3 shows the experimental setup. The vapor containing the NaK molecules is produced in a crossed, stainless steel, heat-pipe oven[90] which was charged with a mixture of potassium and sodium in an approximately 2 to 1 ratio. This mixture was calculated to maximize the NaK concentration relative to other species.[58] The oven was operated at $\sim$360 °C with $\sim$1.5 Torr of argon buffer gas. Thus the conditions were near to, but probably short of, those necessary for heat-pipe mode operation.

The laser is a multimode cw dye laser pumped by 4–5 W from an argon–ion laser. The dye laser output is typically 200–500 mW and is tunable from 680 to 775 nm using the dye LDS 722.

Fluorescence at right angles to the laser beam was dispersed by a 1/3-meter grating monochromator and detected by an intrinsic germanium detector. Longpass filters eliminated second order spectra. Fluorescence spectra were obtained by setting the laser wavelength to a value which yielded a relative maximum in the near-IR emission, and then scanning the monochromator wavelength.

In order to obtain the excitation spectra presented in

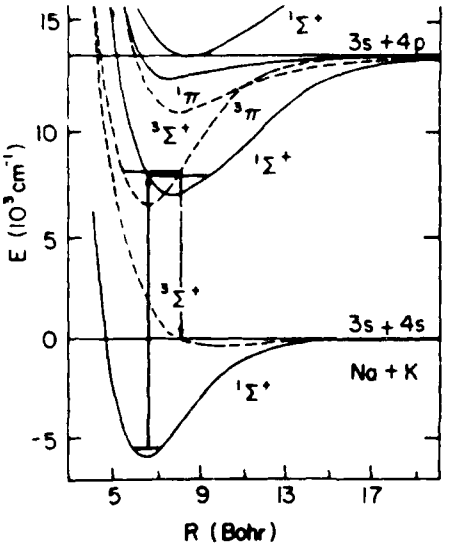

FIG. 2. Nearly degenerate levels of the $1\,^3\Pi_0$ and $2\,^1\Sigma^+$ states with the same rotational quantum number J are coupled by the spin–orbit interaction. The resulting mixed levels have both singlet and triplet character

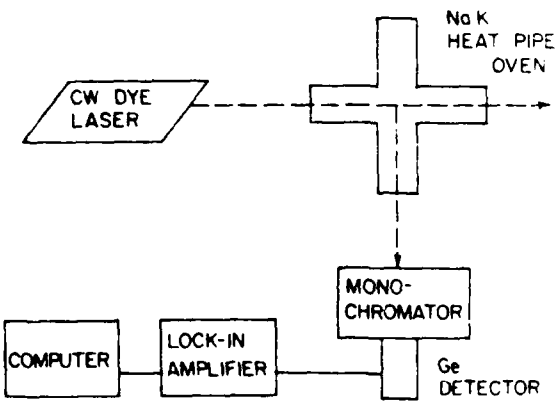

FIG. 3. Apparatus used in the fluorescence experiments

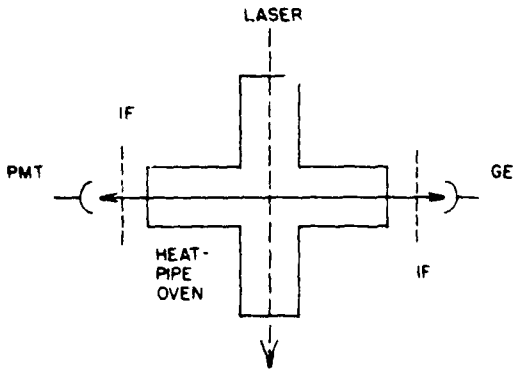

FIG. 4. Apparatus for measuring the $1\,^3\Pi$ excitation spectra. Ge represents the intrinsic germanium detector, while IF and PMT stand for interference filter and photomultiplier tube, respectively. The interference filters were such that, during scan of the laser wavelength, the photomultiplier recorded the total $2\,^1\Sigma^+ \rightarrow 1\,^1\Sigma^+$ emission, while the Ge detector simultaneously recorded the total $1\,^3\Pi \rightarrow 1\,^3\Sigma^+$ emission.

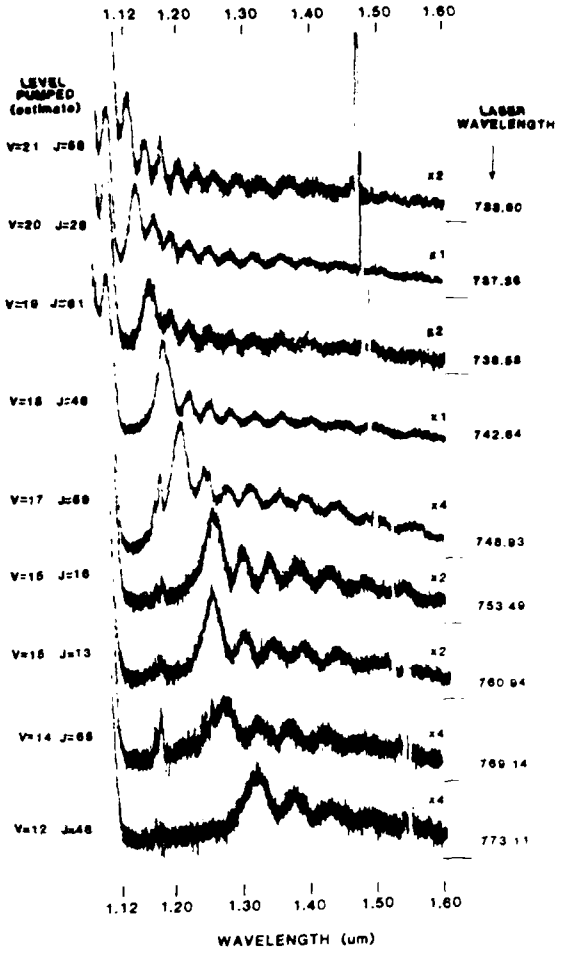

FIG. 5. NaK near-infrared $1\,^3\Pi \rightarrow 1\,^3\Sigma^+$ fluorescence spectra produced by pumping specific $1\,^3\Pi \leftarrow 1\,^1\Sigma^+$ transitions with selected frequencies from the tunable dye laser. The laser wavelength used for each spectrum is given on the right, while the v, J designation on the left is our best estimate of the pumped upper level.

Sec. III C, the monochromator was replaced by an interference filter with a bandpass of 1.1 to 1.6 μm (see Fig. 4). A photomultiplier (*S*-1 response) was placed directly across from the Ge detector and an interference filter with a bandpass of 0.65 to 1.0 μm was placed between the oven and photomultiplier. Thus the germanium detector recorded the total triplet band ($1\,^3\Pi \rightarrow 1\,^3\Sigma^+$) emission, while the photomultiplier recorded the total singlet-band ($2\,^1\Sigma^+ \rightarrow 1\,^1\Sigma^+$) emission. In this experiment, the laser wavelength was scanned with a motorized drive connected to the dye laser birefringent filter. Dye laser wavelengths were measured with a monochromator–photomuliplier arrangment.

In either experiment (fluorescence or excitation spectra), the cw laser beam was chopped and the Ge detector output sent to a lock-in amplifier. The photomultiplier output was processed by an electrometer. Infrared fluorescence scans were recorded directly on a chart recorder, while for excitation spectra the lock-in and electrometer outputs were simultaneously digitized and recorded by a computer.

III. RESULTS

A. Fluorescence spectra

Figure 5 shows the fluorescence spectra obtained for various pump laser wavelengths. The spectra display the bound–free reflection structure first described theoretically by Condon in 1928,[91,92] and later more rigorously by Coolidge *et al.*,[93] and Tellinghuisen and co-workers.[94,95] Over the years, several specific cases of bound–free reflection structure have been studied both experimentally and theoretically (e.g. see Refs. 96–104 and references therein). However, a particularly graphic example of this type of emission has recently been observed in the spectrum of Hg_2 by Niefer and co-workers[105] (see Fig. 4 of Ref. 105).

The origin of the oscillatory structure in the present case can be crudely understood with reference to Fig. 6. The upper state ($1\,^3\Pi$) of the fluorescence forms roughly a harmonic well, so that the wave functions are similar to those of a harmonic oscillator. Of interest to this discussion is the probability distribution, or wave function squared, which is plotted in the figure. According to the classical Franck–Condon principle, neither the internuclear separation R nor the kinetic energy changes in an electronic transition. The first of these criteria requires that arrows representing transitions be vertical in this type of figure, while the second requires that the arrows terminate on the dashed line (the "Mulliken difference potential"[94,95,106]) which represents the $1\,^3\Sigma^+$ potential energy plus the kinetic energy of the initial upper level. As can be seen in this simple classical picture, different R values yield different wavelengths in the fluorescence spectrum, and each wavelength is weighted by the probability [$\chi^*(R)\chi(R)$ where χ is the nuclear wave function] that the atom pair is separated by that particular R. The largest peak in the fluorescence spectrum, which always occurs at the short wavelength end of the band, corresponds to the maximum in the wave function at the outer turning point. The analogous large peak corresponding to the inner turning

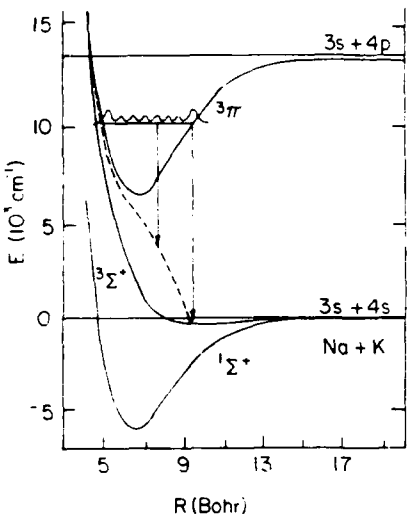

FIG. 6. A crude explanation of the oscillatory spectra can be obtained by applying the classical Franck–Condon principle (CFCP), in which the oscillations simply reflect the probability distribution (which is sketched here qualitatively) in the bound upper state. The dashed curve represents the lower state potential energy, plus the kinetic energy in the upper state (which is conserved according to the CFCP). Transistions at two R values are shown by arrows.

point cannot be observed in our case, because the difference potential becomes quite small at short R and the emission is past the long wavelength edge of our detector response. Since the difference potential is monotonic, there is no interference between contributions at one wavelength from two separate R values, nor do we expect to observe satellite features which commonly result from extrema in difference potentials. (Tellinghuisen and co-workers make a useful distinction between reflection structure, which occurs for a monotonic difference potential, and interference structure, which results when more than one R value can contribute to a single wavelength.[94,95,107]) Also from Fig. 5 we see that the short wavelength edge of the emission moves to longer wavelengths as we increase the pump laser wavelength. This simply reflects the fact that photons of longer wavelength pump lower levels of the upper state, which then radiate at longer wavelengths.

Note that even though Na_2 and K_2 molecules also exist in the sodium–potassium mixture, the emission can unambiguously be assigned to NaK since the analogous $^3\Pi \rightarrow {}^3\Sigma$ transitions are forbidden by symmetry considerations ($u \nleftrightarrow u$) in the homonuclear molecules. Since the signals are linear in laser power, the upper state of the emission must lie in the first excited manifold. Of all the possible transitions of NaK, Na_2 and K_2 involving these states, only the NaK $1\,^3\Pi \rightarrow 1\,^3\Sigma^+$ band lies in this wavelength range.

B. Calculations

Because of the complexity of the excitation spectra (see Sec. III C), it was difficult to determine which rovibrational levels of the $1\,^3\Pi$ state were populated for a given laser wavelength. New measurements, which are currently underway, will hopefully overcome this problem. For the present work, we used the following argument to obtain a reasonable assignment of the pumped levels. As more accurate data becomes available, these assignments will most likely require modification.

Accurate spectroscopic constants exist for the $1\,^1\Sigma^+$ and $1\,^3\Pi_1$ states of NaK.[80,81] By using the value for the $^3\Pi$ fine-structure splitting suggested in Ref. 80, we determined energies for the various levels of the $1\,^3\Pi_0$ state. This is the state which is most strongly perturbed by the spin–orbit interaction. Since the $1\,^3\Pi_0 \leftarrow 1\,^1\Sigma^+$ transitions are made possible by the admixture of $2\,^1\Sigma^+$ probability amplitude into the triplet state, the selection rules will be the same as for $2\,^1\Sigma^+ \leftarrow 1\,^1\Sigma^+$ transitions, namely $\Delta J = \pm 1$. We then matched the laser energy to a list of energies for $1\,^3\Pi_0(v', J'' \pm 1) \leftarrow 1\,^1\Sigma^+(v'', J'')$ transitions. (The search was limited to the most heavily populated levels, i.e., $v'' \leq 5$, $J'' < 150$.) This yielded several possible transitions for each laser wavelength in Fig. 5. However, plausibility arguments could be used to further restrict the list. For instance, looking at Fig. 5 it seems likely from the regular progression of the short wavelength edge of the band that the upper state vibrational number must increase monotonically as we go from bottom to top. However, the close similarity of the 753.49 and 760.94 nm spectra argues that in those two cases we pumped the same upper vibrational state. Additionally we know that J levels near the most probable value [$(J_{max} = (kT/2B)^{1/2} - 1/2 \approx 48)$][106] are favored. Finally we used experimental $2\,^1\Sigma^+$ vibrational constants from Loomis and Arvin,[109] and calculated rotational constants from Stevens *et al.*[87] to predict perturbed level positions. Putting all of this information together allowed us to make an educated guess of the pumped upper level. We are confident that the vibrational numbering is correct at least to within ± 1. The uncertainty in our rotational numbering is much greater and the values we present at this point are strictly for purposes of illustration.

In order to test this proposed explanation of the oscillatory fluorescence emission, we have carried out quantum mechanical simulations of the bound–free $1\,^3\Pi \rightarrow 1\,^3\Sigma^+$ emission. These calculations are based upon the Stevens *et al.*[87] potentials and the Ratcliff *et al.*[88] transition dipole functions. The calculations were carried out for the specific $^3\Pi$ state levels that we estimated were pumped by the laser. Relative intensities were determined at 200 wavelengths covering the range of the observed spectra. Because we are simulating measurements of spontaneous emission power dispersed on a linear wavelength scale, a weighting factor of λ^{-6} was used. The calculated spectra are shown as solid lines in Fig. 7. The bound–free intensity drops abruptly to zero at short wavelengths due to the threshold for bound–free emission. We surmise that bound–bound emission beyond the bound–free threshold is experimentally indistinguishable from bound–free emission due to the resolution of the fluorescence detection (~ 5 nm) and the very close spacing of the $1\,^3\Sigma^+$ vibrational levels (~ 23 cm^{-1}). Therefore, we have calculated intensities of the bound–bound transitions, weighted them by the density of states and plotted them as points in Fig. 7. All calculations were performed with the Iowa library of computer codes for diatomic spectroscopy[110]

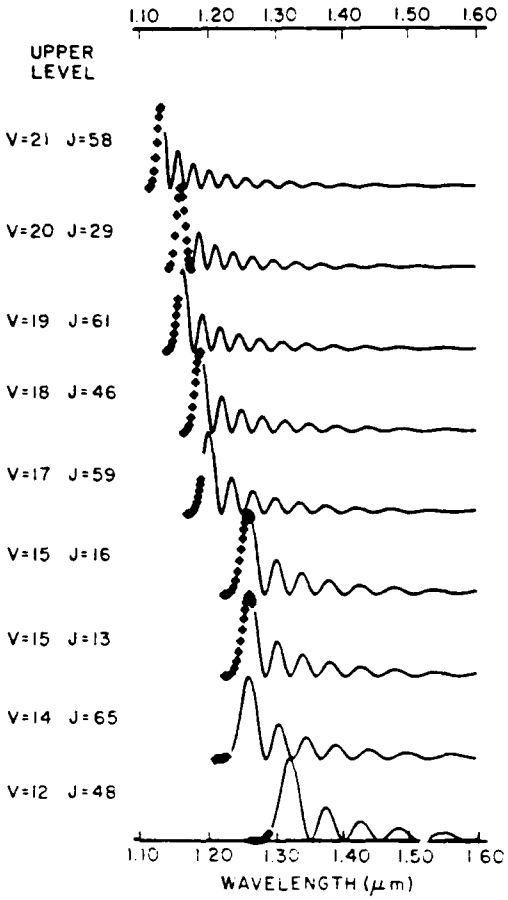

FIG. 7. Quantum mechanical calculations of the NaK bound–free $1\,^3\Pi \rightarrow 1\,^3\Sigma^+$ emission, based on the theoretical potentials of Ref. 87 and the transition dipole moments of Ref. 88. Solid lines represent bound–free emission while dotted lines represent bound–bound emission.

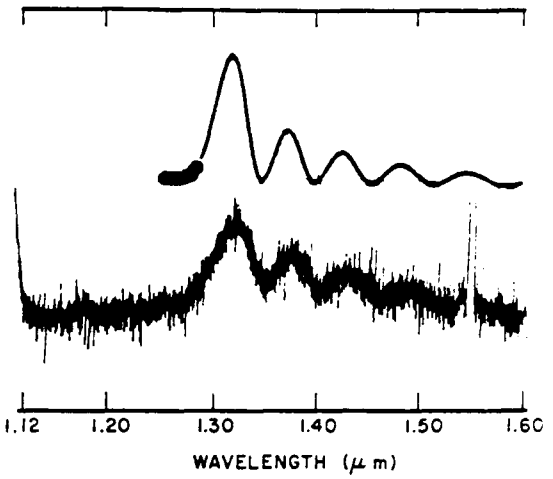

FIG. 8. Experimental and calculated spectra corresponding to excitation at 773.11 nm. We estimate that this laser wavelength populates the $v = 12$, $J = 48$ level of the $1\,^3\Pi$ state. In the calculated spectrum the thin solid line represents bound–free emission, while the thick line at the left represents bound–bound contributions.

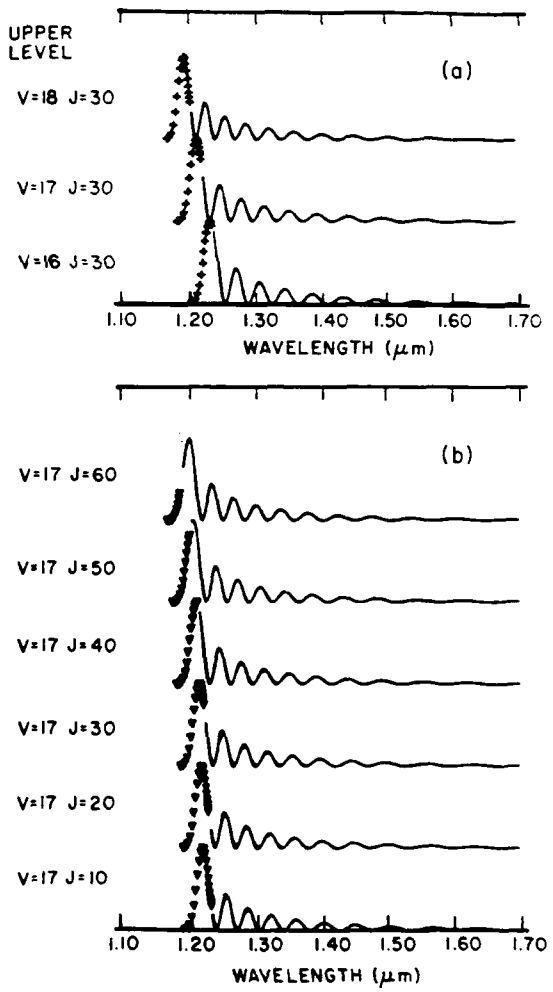

FIG. 9. Variation of the calculated spectrum due to (a) changes in the upper state vibrational quantum number and (b) changes in the upper state rotational quantum number. Solid lines represent bound–free emission and points represent bound–bound contributions.

following methods outlined by Herman and Sando.[111] Only Q-branch transitions were included in these exploratory calculations. The addition of P and R branches would cause a slight broadening of the spectra and nonzero intensities at the "nodes". The density of states was determined as $(dE_{v,J}/dv)^{-1}$ with the derivative determined by a spline interpolation of the vibrational energy vs vibrational quantum number. Intensities of transitions to the two highest bound states (usually quasibound) were discarded because the interpolation gave inaccurate derivatives near the end of its range. Note that this treatment of the bound–bound spectrum as an extension of the bound–free has previously been thoroughly tested (see, e.g., Ref. 103).

The trends in the emission threshold and frequency of oscillations can be seen in Fig. 7 while a detailed comparison to experiment in the case of 773.11 nm excitation is shown in Fig. 8. Figure 9 shows the effects of separately varying the upper state vibrational and rotational quantum numbers in the calculated spectra.

The good agreement between the calculated and observed spectra indicate that the proposed origin of the oscillatory fluorescence spectra is correct. More detailed com-

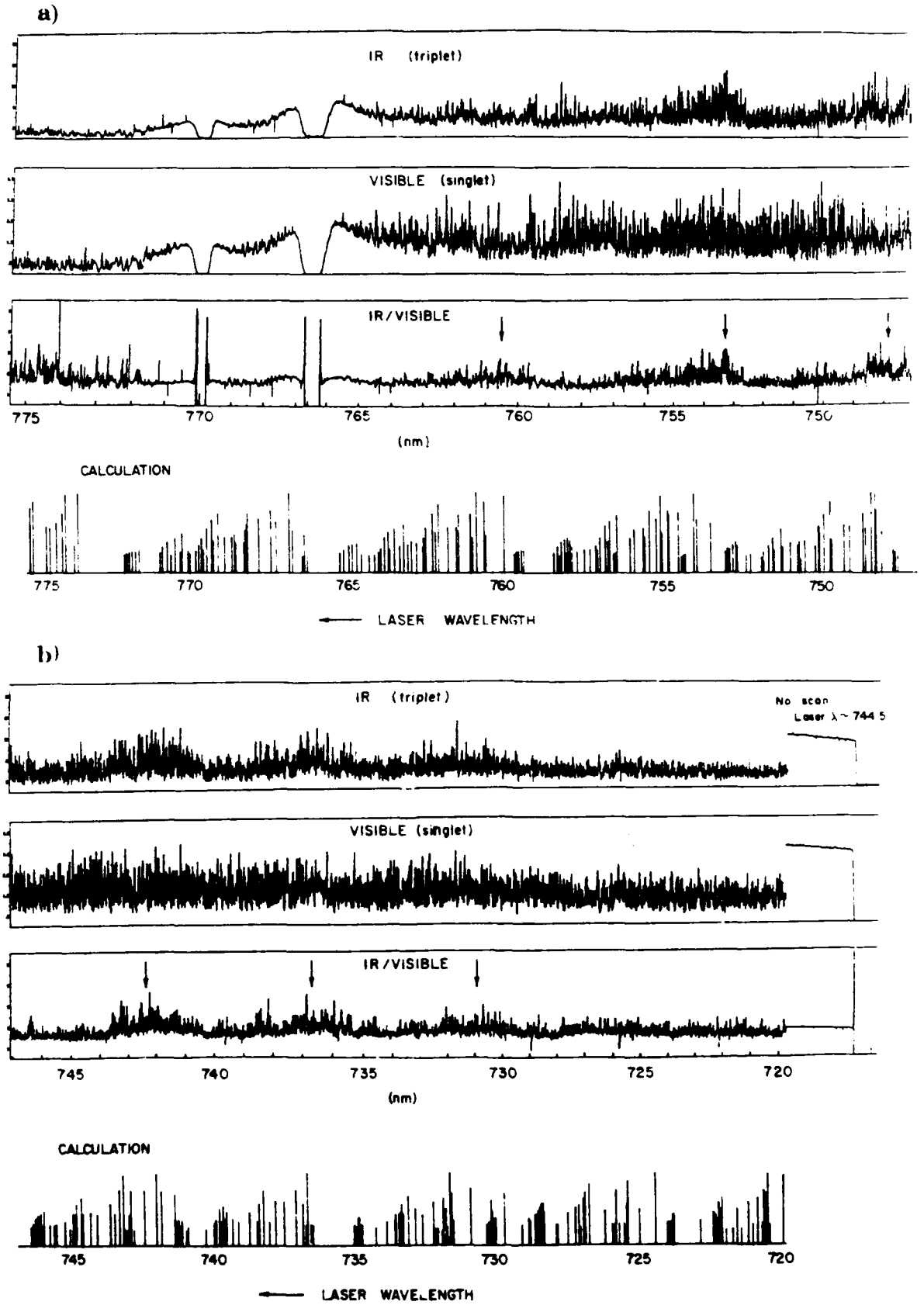

FIG. 10. NaK excitation spectra for laser wavelengths from (a) 775 to 747 nm and (b) 747 to 720 nm. First trace: $1\,^3\Pi \rightarrow 1\,^1\Sigma^+$ emission vs laser wavelength. Second trace: $2\,^1\Sigma^- \rightarrow 1\,^1\Sigma^+$ emission vs laser wavelength (note Na_2 and K_2 singlet emission bands also contribute to this spectrum). Third trace: triplet spectrum divided by singlet spectrum (first trace divided by second). Bottom trace: calculated spectrum (see the text).

parisons of experiment and theory, which are now underway, should allow accurate mapping of the $1^3\Sigma^+$ state potential. This will be discussed further in Sec. IV.

C. Excitation spectra

An attempt was made to map out the perturbations that exist between the NaK $1\,^3\Pi$ and $2\,^1\Sigma^+$ states. The experimental setup is shown in Fig. 4 and described in Sec. II. In this experiment, the laser wavelength was scanned while the total $2\,^1\Sigma^+ \rightarrow 1\,^1\Sigma^+$ band fluorescence and the total $1\,^3\Pi \rightarrow 1\,^3\Sigma^+$ band fluorescence were simultaneously recorded using two separate detectors.

The singlet excitation spectrum was expected to be quite complicated since singlet fluorescence occurs whenever the laser wavelength matches that of an allowed rovibrational transition of the NaK $2\,^1\Sigma^+ \leftarrow 1\,^1\Sigma^+$ absorption band. Additionally, strong singlet bands of both Na_2 and K_2 absorb and radiate in this wavelength region and thereby contribute to the singlet excitation spectrum.

We expected the triplet excitation spectrum to be much simpler since Na_2 and K_2 cannot radiate in the 1.1 to 1.6 μm wavelength range (assuming absorption of only one laser photon), and the NaK triplet fluorescence requires pumping of one of the mixed $2\,^1\Sigma^+$–$1\,^3\Pi$ levels. Thus we hoped that the peaks in the excitation spectrum would map out the perturbations in a simple and direct way.

The singlet and triplet excitation spectra are displayed in Fig. 10. As can be seen, both the singlet and triplet spectra are quite complicated. That the many spikes are not noise is verified in the right-most part of Fig. 10(b), where the laser wavelength was fixed at ~ 744.5 nm. We also see reproducible regions of the triplet spectrum where the signal appears enhanced. These regions are more visible in the third trace of Fig. 10, where we have divided the triplet emission by the singlet emission. The enhanced triplet regions (marked by arrows in the third trace of Fig. 10) are roughly equally spaced, and we believe they represent pumping from the $v = 0$ level of the ground state (which is most heavily populated) into various levels of the upper $^3\Pi$ state. Thus the spacing between the enhanced regions simply reflects the vibrational spacing of the $1\,^3\Pi$ state.

As mentioned in Sec. III B, we used experimental vibrational constants from Ref. 109 and calculated rotational constants from Ref. 87 to obtain energies for the rovibrational levels of the $2\,^1\Sigma^+$ state. These were combined with the known $1\,^1\Sigma^+$ and $1\,^3\Pi$ level energies[80,81] to obtain a "theoretical" list of levels which are most strongly perturbed. Laser wavelengths required to excite these levels were calculated, and a theoretical triplet spectrum was created (bottom trace of Fig. 10). The weighting of the lines is simply the Boltzmann population factor $(2J+1)\exp(-E_{v,J}/kT)$ for the lower state.

Clearly we cannot expect a quantitative match between the observed spectrum and this simple calculation. However, we do see that perturbed levels are quite common, which explains the complexity of the triplet excitation spectrum. Strong perturbations are found almost every 15 rotational levels of each vibrational level of the $^3\Pi_0$ state. Nearby levels (not included in the calculated spectrum of Fig. 10) are also somewhat perturbed, as are various levels of the $^3\Pi_1$ and $^3\Pi_2$ states. This results in perhaps 10% or 20% of all $2\,^1\Sigma^+$ levels having significant triplet admixtures. The calculated triplet excitation spectrum also verifies that the enhanced regions originate in the $v = 0$ levels of the ground state.

More accurate modeling of the excitation spectrum requires accurate experimental constants for the $2\,^1\Sigma^+$ state, which would permit calculation of perturbation positions and strengths, the inclusion of Franck–Condon factors, etc. Additionally, single-mode laser excitation spectra would also be useful. These experimental and theoretical studies are now underway in our laboratories and will be presented in a later publication.[89]

IV. CONCLUSIONS

In summary, we have observed NaK $1\,^3\Pi \rightarrow 1\,^1\Sigma^+$ bound–free emission from specific vibrational levels of the upper state. We have also carried out quantum mechanical simulations of the emission spectra based upon recent *ab initio* NaK potentials.[87] These simulations verify that the emission is of the reflection type; i.e., that the oscillations in the spectra simply reflect the oscillations in the bound level probability distribution function.

At present, we are repeating the fluorescence experiment using a single-mode laser which hopefully will produce cleaner spectra. We are also redoing the calculations, but using the accurate $1\,^3\Pi$ and $1\,^1\Sigma^+$ potentials which are now available from Fourier transform spectroscopy.[80,81] Parameters for the lower $1\,^3\Sigma^+$ state will be varied to maximize agreement between experimental and calculated spectra. This procedure should yield accurate information on the repulsive wall of the $1\,^3\Sigma^+$ potentials. Finally, we are in the process of using a single mode laser to obtain the triplet excitation spectra. It is hoped that the resulting simplification will allow an accurate mapping of the $1\,^3\Pi$–$2\,^1\Sigma^+$ perturbations.

It is possible that this $1\,^3\Pi \rightarrow 1\,^3\Sigma^+$ band of NaK and analogous bands of other heteronuclear alkali molecules may be used to develop widely tunable cw or pulsed near-infrared lasers. In this context, the large number of $1\,^3\Pi$–$2\,^1\Sigma^+$ perturbations is a distinct advantage. We are actively pursuing such possibilities for laser development in our laboratories.

Note added in proof: After submission of the manuscript, accurate experimental constants for the NaK $2\,^1\Sigma^+$ state became availabe from Fourier transform spectroscopy [A. J. Ross, R. M. Clements, and R. F. Barrow, J. Mol. Spectrosc. **127**, 546 (1988)]. In addition Le Roy, Keogh, and Child have recently developed a procedure for inverting bound–free spectra to yield potentials. They have used this procedure to map the NaK $1\,^3\Sigma^+$ state from Breford and Engelke's[57] data on bound–free $2\,^3\Pi \rightarrow 1\,^3\Sigma^+$ emission [R. J. Le Roy, W. J. Keogh, and M. S. Child, J. Chem. Phys. (submitted)].

ACKNOWLEDGMENTS

We would like to thank Kurt Gibble for his great assistance in the early stages of this project, and Joe Zelinski for

his skillful machining of the heat-pipe oven. We would also like to thank Dr. Will Happer and Dr. Frank Feigl for loans of key pieces of equipment and Thad Walker, Dr. William Stwalley, Dr. Marjatta Lyyra, and Dr. Paul Kleiber for useful discussions. This work was supported by the U. S. Army Research Office under Grant No. DAAL03-86-K-0161 and the National Science Foundation under Grant No. PHY-8451279.

[1]M. A. Henesian, R. L. Herbst, and R. L. Byer, J. Appl. Phys. **47**, 1515 (1976).
[2]H. Itoh, H. Uchiki, and M. Matsuoka, Opt. Commun. **18**, 271 (1976).
[3]H. Wellegehausen, S. Shahdin, D. Friede, and H. Welling, Appl. Phys. **13**, 97 (1977).
[4]B. Wellegehausen, IEEE J. Quantum Electron. **15**, 1108 (1979).
[5]A. R. Rajaei-Rizi, J. T. Bahns, K. K. Verma, and W. C. Stwalley, Appl. Phys. Lett. **40**, 869 (1982).
[6]J. T. Bahns, K. K. Verma, A. R. Rajaei-Rizi, and W. C. Stwalley, Appl. Phys. Lett. **42**, 336 (1983).
[7]P. L. Jones, U. Gaubatz, U. Hefter, K. Bergmann, and B. Wellegehausen, Appl. Phys. Lett. **42**, 222 (1983).
[8]W. Luhs, M. Hube, U. Schottelius, and B. Wellegehausen, Opt. Commun. **48**, 265 (1983).
[9]B. Wellegehausen, W. Luhs, A. Topouzkhanian, and J. d'Incan, Appl. Phys. Lett. **43**, 912 (1983).
[10]J.-G. Wang, Y.-C. Wang, G. P. Morgan, and A. L. Schawlow, Opt. Commun. **48**, 398 (1984).
[11]V. M. Kaslin and O. F. Yakushev, Sov. J. Quantum Electron. **13**, 1575 (1983).
[12]D. D. Konowalow and P. S. Julienne, J. Chem. Phys. **72**, 5815 (1980).
[13]M. Allegrini, G. Alzetta, A. Kopystynska, L. Moi, and G. Orriols, Opt. Commun. **22**, 329 (1977).
[14]J. P. Woerdman, Opt. Commun. **26**, 216 (1978).
[15]A. Kopystynska and P. Kowalczyk, Opt. Commun. **28**, 78 (1979).
[16]M. Allegrini and L. Moi, Opt. Commun. **32**, 91 (1980).
[17]C. Y. R. Wu and J. K. Chen, Opt. Commun. **44**, 100 (1982).
[18]G. Pichler, S. Milosevic, D. Veza, and S. Bosanac, in *Spectral Line Shapes*, edited by K. Burnett (Walter de Gruyter, Berlin, 1983), Vol. II, p. 613.
[19]G. Pichler, S. Milosevic, D. Veza, and R. Beuc, J. Phys. B **16**, 4619 (1983).
[20]Cz. Radzewicz, P. Kowalczyk, and J. Krasinski, Opt. Commun. **44**, 139 (1983).
[21]C. Radzewicz, P. Kowalczyk, and J. Krasinski, Z. Phys. A **314**, 293 (1983).
[22]C. Y. R. Wu, J. K. Chen, D. L. Judge, and C. C. Kim, Opt. Commun. **48**, 28 (1983).
[23]L. Li, S. F. Rice, and R. W. Field, J. Chem. Phys. **82**, 1178 (1985).
[24]G. Pichler, J. T. Bahns, K. M. Sando, W. C. Stwalley, D. D. Konowalow, L. Li, R. W. Field, and W. Muller, Chem. Phys. Lett. **129**, 425 (1986).
[25]P. Kowalczyk, C. Radzewicz, and H. Liening, Chem. Phys. **102**, 377 (1986).
[26]S. Milosevic and G. Pichler, Z. Phys. D **1**, 223 (1986).
[27]Z. G. Wang, L. A. Ma, H. R. Xia, K. C. Zhang, and I. S. Cheng, Opt. Commun. **58**, 315 (1986).
[28]J. M. Walter and S. Barratt, R. Soc. Proc. A **119**, 257 (1928).
[29]M. M. Rebbeck and J. M. Vaughan, J. Phys. B **4**, 258 (1971).
[30]Yu. P. Korchevoi, V. I. Lukashenko, and S. N. Lukashenko, Sov. Phys. JETP **48**, 428 (1978).
[31]Yu. P. Korchevoi, V. I. Lukashenko, and S. N. Lukashenko, Phys. Scr. **19**, 271 (1979).
[32]D. D. Konowalow, S. Milosevic, and G. Pichler, J. Mol. Spectrosc. **110**, 256 (1985).
[33]D. E. Johnson and J. G. Eden, J. Opt. Soc. Am. B **2**, 721 (1985).
[34]C. Vadla, K. Niemax, and G. Pichler, Z. Phys. D **2**, 233 (1986).
[35]S. Milosevic, G. Pichler, R. Duren, and E. Hasselbrink, Chem. Phys. Lett. **128**, 145 (1986).
[36]S. Milosevic, P. Kowalczyk, asnd G. Pichler, J. Phys. B **20**, 2231 (1987).
[37]G. Pichler, S. Milosevic, and D. Veza, Chem. Phys. Lett. **103**, 352 (1984).
[38]D. Veza, S. Milosevic, and G. Pichler, Opt. Commun. **56**, 172 (1985).
[39]H. H. Wu, T. C. Chu, and C. Y. R. Wu, Appl. Phys. B **43**, 225 (1987).
[40]M. McClintock and L. C. Balling, J. Quant. Spectrosc. Radiat. Trans. **9**, 1209 (1969).
[41]J. M. Brom and H. P. Broida, J. Chem. Phys. **61**, 982 (1974).
[42]G. Pichler, S. Milosevic, D. Veza, and D. Vukicevic, J. Phys. B **16**, 4633 (1983).
[43]F. W. Loomis and P. Kusch, Phys. Rev. **46**, 292 (1934).
[44]R. Gupta, W. Happer, J. Wagner, and E. Wennmyr, J. Chem. Phys. **68**, 799 (1978).
[45]J. Huennekens, Z. Wu, and T. G. Walker, Phys. Rev. A **31**, 196 (1985).
[46]K. Schmidt, in *Comptes Rendus de la VI^e Conference Internationale sur les Phenomenes d'Ionisation dans les Gaz*, edited by P. Hubert and E. Cremieu-Alcan (S.E.R.M.A. Paris, 1963), Vol. III, p. 323.
[47]P. P. Sorokin and J. R. Lankard, J. Chem. Phys. **55**, 3810 (1971).
[48]S. Shahdin, B. Wellegehausen, and Z. G. Ma, Appl. Phys. B **29**, 195 (1982).
[49]J. P. Woerdman and J. J. de Groot, Chem. Phys. Lett. **80**, 220 (1981).
[50]M. Ligare, S. Schaefer, J. Huennekens, and W. Happer, Opt. Commun. **48**, 39 (1983).
[51]J. Huennekens, S. Schaefer, M. Ligare, and W. Happer, J. Chem. Phys. **80**, 4794 (1984).
[52]A. M. Bonch-Bruevich, T. A. Vartanyan, Yu. N. Maksimov, and V. V. Khromov, Opt. Spectrosc. (USSR) **58**, 331 (1985).
[53]M. Palle, S. Milosevic, D. Veza, and G. Pichler, Opt. Commun. **57**, 394 (1986).
[54]J. T. Bahns and W. C. Stwalley, Appl. Phys. Lett. **44**, 826 (1984).
[55]S. G. Dinev, I. G. Koprinkov and I. L. Stefanov, Opt. Commun. **52**, 196 (1984).
[56]Z. G. Wang, H. Schmidt, and B. Wellegehausen, Appl. Phys. B **44**, 41 (1987).
[57]E. J. Breford and F. Engelke, Chem Phys. Lett. **53**, 282 (1978).
[58]E. J. Breford and F. Engelke, J. Chem. Phys. **71**, 1994 (1979).
[59]D. Eisel, D. Zevgolis, and W. Demtroder, J. Chem. Phys. **71**, 2005 (1979).
[60]C.-L. Chiu and H. Chang, Chem. Phys. Lett. **73**, 167 (1980).
[61]H. Kato and C. Noda, J. Chem. Phys. **73**, 4940 (1980).
[62]H. Kato, M. Baba, and I. Hanazaki, J. Chem. Phys. **80**, 3936 (1984).
[63]P. Kusch and M. M. Hessel, J. Chem. Phys. **63**, 4088 (1975).
[64]J. B. Atkinson, J. Becker and W. Demtroder, Chem. Phys. Lett. **87**, 92 (1982).
[65]F. Shimizu, K. Shimizu, and H. Takuma, Phys. Rev. A **26**, 2701 (1982).
[66]K. Shimizu and F. Shimizu, J. Chem. Phys. **78**, 1126 (1983).
[67]F. Shimizu and K. Shimizu, J. Chem. Phys. **78**, 2798 (1983).
[68]B. E. Miller and P. A. Schultz, in *Advances in Laser Science Vol. I.*, edited by W. C. Stwalley and M. Lapp (American Institute of Physics, New York, 1986), p. 464.
[69]C. Effantin, G. Babaky, K. Hussein, J. d'Incan, and R. F. Barrow, J. Phys. B. **18**, 4077 (1985).
[70]W. Preuss and G. Baumgartner, Z. Phys. A **320**, 125 (1985).
[71]O. C. Mullins, C. R. Mahon, and T. F. Gallagher, Chem. Phys. Lett. **126**, 501 (1986).
[72]M. Li, C. Wang, Y. Wang, and L. Li, J. Mol. Spectrosc. **123**, 161 (1987).
[73]L. Li and R. W. Field, J. Phys. Chem. **87**, 3020 (1983).
[74]L. Li, S.F. Rice and R. W. Field, J. Mol. Spectrosc. **105**, 344 (1984).
[75]X. Xie and R. W. Field, Chem. Phys. **99**, 337 (1985).
[76]X. Xie and R. W. Field, J. Chem. Phys. **83**, 6193 (1985).
[77]S. F. Rice, X. Xie and R. W. Field, Chem. Phys. **104**, 161 (1986).
[78]X. Xie and R. W. Field, J. Mol. Spectrosc. **117**, 228 (1986).
[79]L. Li and R. W. Field, J. Mol. Spectrosc. **117**, 245 (1986).
[80]A. J. Ross, C. Effantin, J. d'Incan, and R. F. Barrow, J. Phys. B **19**, 1449 (1986).
[81]A. J. Ross, C. Effantin, J. d'Incan, and R. F. Barrow, Mol. Phys. **56**, 903 (1985).
[82]J. Verges, C. Effantin, J. d'Incan, A. Topouzkhanian, and R. F. Barrow, Chem. Phys. Lett. **94**, 1 (1983).
[83]C. Effantin, J. d'Incan, A. J. Ross, R. F. Barrow, and J. Verges, J. Phys. B **17**, 1515 (1984).
[84]J. Verges, C. Effantin, J. d'Incan, D. L. Cooper, and R. F. Barrow, Phys. Rev. Lett. **53**, 46 (1984).
[85]D. L. Cooper, R. F. Barrow, J. Verges, C. Effantin, and J. d'Incan, Can. J. Phys. **62**, 1543 (1984).
[86]J. Huennekens, T. G. Walker, and S. C. McClain, J. Chem. Phys. **83**, 4949 (1985).
[87]W. J. Stevens, D. D. Konowalow, and L. B. Ratcliff, J. Chem. Phys. **80**, 1215 (1984).
[88]L. B. Ratcliff, D. D. Konowalow, and W. J. Stevens, J. Mol. Spectrosc. **110**, 242 (1985).
[89]J. Huennekens, M. Masters, K. Sando, M. Lyyra, V. Zafiropulos, W-T.

Luh, and W. C. Stwalley (to be published).
[90]C. R. Vidal and J. Cooper, J. Appl. Phys. **40**, 3370 (1969).
[91]E. U. Condon, Phys. Rev. **32**, 858 (1928).
[92]E. U. Condon, Am. J. Phys. **15**, 365 (1947).
[93]A. S. Coolidge, H. M. James, and R. D. Present, J. Chem. Phys. **4**, 193 (1936).
[94]J. Tellinghuisen, G. Pichler, W. L. Snow, M. E. Hillard, and R. J. Exton, Chem. Phys. **50**, 313 (1980).
[95]J. Tellinghuisen, J. Mol. Spectrosc. **103**, 455 (1984).
[96]Y. Tanaka and K. Yoshino, J. Chem. Phys. **39**, 3081 (1963).
[97]F. H. Mies and A. L. Smith, J. Chem. Phys. **45**, 994 (1966).
[98]A. L. Smith, J. Chem. Phys. **49**, 4817 (1968).
[99]K. M. Sando and A. Dalgarno, Mol. Phys. **20**, 103 (1971).
[100]J. Tellinghuisen, A. K. Hays, J. M. Hoffman, and G. C. Tisone, J. Chem. Phys. **65**, 4473 (1976).
[101]K. Sakurai and H. P. Broida, J. Chem. Phys. **65**, 1138 (1976).
[102]H. Scheingraber and C. R. Vidal, J. Chem. Phys. **66**, 3694 (1977).
[103]J. Tellinghuisen, A. Ragone, M. S. Kim, D. J. Auerbach, R. E. Smalley, L. Wharton, and D. H. Levy, J. Chem. Phys. **71**, 1283 (1979).
[104]W. Koot, W. J. van der Zande, and J. Los, Phys. Rev. Lett. **58**, 274 (1987).
[105]R. J. Niefer, J. Supronowicz, J. B. Atkinson, and L. Krause, Phys. Rev. A **34**, 1137 (1986).
[106]K. Tamagake, and D. W. Setser, J. Chem. Phys. **67**, 4370 (1977).
[107]J. Tellinghuisen, Chem. Phys. Lett. **29**, 359 (1974).
[108]G. Herzberg, *Molecular Spectra and Molecular Structure, Vol. I Spectra of Diatomic Molecules* (Van Nostrand Reinhold, New York, 1950).
[109]F. W. Loomis and M. J. Arvin, Phys. Rev. **46**, 286 (1934).
[110]P. S. Herman and K. M. Sando (unpublished).
[111]P. S. Herman and K. M. Sando, J. Chem. Phys. **68**, 1153 (1978).
[112]D. D. Konowalow, M. E. Rosenkrantz, and M. L. Olson, J. Chem. Phys. **72**, 2612 (1980).

Appendix 2 (to be submitted to J. Chem. Phys. - preliminary)

Bound-Free $1^3\Pi \rightarrow 1^3\Sigma^+$ emission from the NaK molecule: determination of the $1^3\Sigma^+$ repulsive wall above the dissociation limit.

Mark Masters, John Huennekens, Wei Tzou Luh

Lehigh University, Department of Physics. Bethlehem, PA 18015

Li Li[1], *A. Marjatta Lyrra*[2], *Ken Sando*[3], *Vassilios Zafiropulos*[4], *William C. Stwalley*[2]

Center for Laser Science and Engineering, University of Iowa. Iowa City, IA 52242

ABSTRACT

We report the observation of bound-free emission on the $1^3\Pi \rightarrow 1^3\Sigma^+$ band of the NaK molecule. The spectra, which consist of oscillating continua in the near-infrared, have been analyzed to determine parameters describing the repulsive wall of the $1^3\Sigma^+$ state above the dissociation limit. Spectra calculated using a potential of the form $Ae^{-BR}+C$ for the $1^3\Sigma^+$ state were compared to experimental spectra to yield the following values: $A = 6\times10^5$ cm^{-1} , $B = 1.605$ Å^{-1}, $C = -223.990$ cm^{-1} . The relative transition dipole moment of the $1^3\Pi \rightarrow 1^3\Sigma^+$ band has also been determined over a limited range in R through the study of relative intensities of various maxima within each oscillating spectra. In the simulated spectra, the dipole moment was represented by a functional form $D(R) = D_0$ (mR - 1) where D_0 is an undetermined normalization factor. The best fit for the parameter m was determined to be 1.243 Å^{-1}.

October 10, 1989

[1] Permanent address:Dalian Institute of Chemical Physics, Chinese Acadamy of Sciences, Dalian, People's Republic of China.

[2] Also Department of Chemistry and Department of Physics and Astronomy.

[3] Also Department of Chemistry

[4] Permanent address:

PACS #'s 34.15.+n, 33.20.Ea

I. Introduction

The lowest triplet state, $1^3\Sigma^+$, of the sodium-potassium molecule is mostly repulsive, but with a shallow van der Waal's minimum at large internuclear separation. Bound-free fluorescence terminating on this state has been observed since 1978,[1-6] and these spectra have been used in several attempts to determine parameters describing the $1^3\Sigma^+$ repulsive wall above the dissociation limit.[1,3,4,7,8] Interest in the repulsive $1^3\Sigma^+$ state of the alkali diatomics was peaked in 1980 by Konowalow and Julienne,[9] who suggested that continuum fluorescence on the $1^3\Sigma^+_g \rightarrow 1^3\Sigma^+_u$ bands of Li_2 and Na_2 might form the basis for continuously tunable near-infrared lasers.

Experimental observation of alkali triplet bands has been hindered by the dipole selection rule $\Delta S = 0$, and the fact that the ground state of the alkali diatomic molecules is a singlet. This has made it difficult to selectively excite to a specific level of an upper triplet state. It is possible to populate these triplet states by means of collisions,[5] however this results in a great number of triplet levels being populated simultaneously and many interesting spectroscopic details are washed out in the complex fluorescence spectra. In particular, the first observation of the NaK $1^3\Pi \rightarrow 1^3\Sigma^+$ band was made in 1985.[5] However, in this case, collisional population of the $1^3\Pi$ state produced a fluorescence spectrum consisting of a broad featureless continuum, decreasing in intensity with increasing wavelength.

A more selective method used to populate the triplet states of the alkali diatomics has been to rely upon spin-orbit perturbations between nearly degenerate singlet and triplet levels of the same J.[1-4, 6, 10-15] In NaK, for example, the $1^3\Pi$ and $2^1\Sigma^+$ states both dissociate to the sodium 3s plus potassium 4p atomic state limit. Because these two potentials overlap significantly (see Fig. 1), there are many possibilities for the occurrence of spin-orbit perturbations which can be used to populate the triplet. This is the approach used to gain access to the triplet manifold of states in the present work. Accurate spectroscopic constants tor the NaK states, $1^3\Pi_1$, and the bound portions of the $1^3\Sigma^+$, have previously been attained by way of similar $2^3\Pi$–$2^1\Pi$ state perturbations using the technique of perturbation-facilitated Fourier-transform spectroscopy.[15, 16] These experimental $1^3\Pi_1$ and $1^3\Sigma^+$ potentials, as well as those of the $1^1\Sigma^+$ and $2^1\Sigma^+$ states (which have also been mapped out using Fourier-transform spectroscopy in Refs. 16 and 17, respectively), play a significant role in the present analysis.

In a previous work, we reported observation of bound-free emission on the NaK $1^3\Pi \rightarrow 1^3\Sigma^+$ band where the $1^3\Pi$ state was populated via $2^1\Sigma^+ - 1^3\Pi$ spin-orbit perturbations following excitation by a multi-mode cw dye laser.[6] Because of the large bandwidth (~30 GHz) of the multimode laser, it was impossible to avoid the simultaneous population of several v,J levels in the upper triplet state. This, and the complexity of the excitation spectra, rendered it impossible to make accurate assignments of the upper $1^3\Pi$ state levels responsible for the

bound-free fluorescence. In addition, since several upper state levels were generally populated, some washing out of the spectra also occurred. Although bound-free oscillations were still visible, our inability to accurately label upper state levels made it impossible to use the spectra to determine specific information concerning the $1^3\Sigma^+$ potential.

In the present work, we report the observation of near-infrared bound-free emission from the $1^3\Pi_\Omega$ states (Ω=0,1,2) to the $1^3\Sigma^+$ state of the sodium-potassium molecule following single-mode ring-dye laser excitation to specific $1^3\Pi_\Omega(v,J)$ levels. Details of the experiment are presented in Sec. III. These observations of the bound-free $1^3\Pi \rightarrow 1^3\Sigma^+$ emission, and the previously determined potentials for the $1^1\Sigma^+$, $2^1\Sigma^+$, $1^3\Pi_1$ states, and the bound portion of the $1^3\Sigma^+$ state, have enabled us to map the repulsive wall of the $1^3\Sigma^+$ state above its dissociation limit, as a function of internuclear separation, R (see Sec. IV c.). From the fluorescence intensity versus wavelength, we have also been able to determine the relative transition dipole moment of the $1^3\Pi \rightarrow 1^3\Sigma^+$ band as a function of internuclear separation (Sec. IV d.).

II. Theory

NaK $1^3\Pi \rightarrow 1^3\Sigma^+$ bound-free emission from one upper v, J level forms a broad oscillatory continuum. Contained within each such fluorescence spectrum is much information about the lower state potential and the transition dipole moment, D(R). If the spectra can be successfully inverted, we can obtain accurate experimental constants for the $1^3\Sigma^+$ state repulsive wall and

the function D(R). Note that the accuracy with which bound state potentials can be mapped is a result of the hundreds or thousands of discrete lines in bound-bound spectra which can be used to fit the potentials. Repulsive states, on the other hand, are much more difficult to map because they generally result in diffuse continua. However, using a tunable laser to generate oscillating bound-free continua from many upper v, J levels, we can observe hundreds of maxima and minima which can be used in a fitting procedure. Thus such spectra should be capable of producing experimental constants for repulsive state potentials with an accuracy approaching those obtainable for bound states.

In general, the intensity of bound-free emission at a wavelength λ is given by the following equation:[18]

$$I(\lambda) = \frac{64}{3}\pi^4 c N_u \left[\frac{c}{\lambda}\right]^6 \left[\int_0^\infty \Psi_U^*(R)\, D(R)\, \Psi_L(R) dR\right]^2 . \qquad (1)$$

Here N_u is the number of atoms in the upper state level, $\Psi_U(R)$ and $\Psi_L(R)$ are the nuclear radial wavefunctions in the upper bound energy level E_U and lower free energy state E_L respectively, and $E_U - E_L = \frac{hc}{\lambda}$. Information about either the upper or lower state potential is buried within the wavefunctions inside the integral. Note that, in many cases (including the present one), D(R) is a slowly varying function, so that it may be brought outside the integral in Eq. 1. Thus the important quantity in Eq. 1 is the square of the wavefunction overlap

integral, $\left[\int_0^\infty \Psi_U(R)\Psi_L(R)dR\right]^2$. Before going on to discuss the quantum mechanical calculations of these fluorescence spectra, it is useful to discuss two approximations to Eq. 1 which have been used to analyze bound-free spectra in the past.

In the classical Franck-Condon approximation (CFCA),[19] it is assumed that electronic transitions take place so rapidly that the nuclei do not change their relative position or velocity. This means that to each R value there is a corresponding wavelength which is given by the difference in the potentials at that R; i.e. $\lambda(R) = hc\left[V_U(R) - V_L(R)\right]^{-1}$. Thus, for a given wavelength, the integral in Eq. 1 collapses to a delta function in R (since E_U is fixed). Under the CFCA, bound-free emission is particularly simple when the difference potential is monotonic, since in that case there are no interference effects.[20] This is the case for the NaK $1^3\Pi \rightarrow 1^3\Sigma^+$ band. The emission intensity at each wavelength is proportional to the probability that the atomic pair is separated by the appropriate R (given by $\Psi_U^*(R)\Psi_U(R)$ where $\Psi_U(R)$ is the upper state nuclear wavefunction). Thus the CFCA spectra directly represent a reflection of the square of the upper state wavefunction onto the Mulliken difference potential,[20] which is defined as the sum of the lower state potential and the upper state kinetic energy (see Fig. 2a). By simply using the reflection principle of the CFCA in comparison with the experimental spectra, one could determine the NaK $1^3\Sigma^+$ state repulsive wall above the dissociation limit

from the positions of the maxima and minima of the reflection structure. One could also determine the relative transition dipole moment from the relative intensities of the maxima.

A second approximation to Eq. 1 (which we will refer to as the delta function approximation - see Fig. 2b) can be obtained by replacing $\Psi_L(R)$ by a delta function at the classical turning point:[7] $\Psi_L(R) = \delta(E_L - V_L(R))$. Since the actual lower state wavefunction oscillates more rapidly with increasing kinetic energy, the overlap with the upper state wavefunction will tend to cancel for R values far from the repulsive wall. This delta function approximation weights the lower state turning point exclusively. Clearly the delta function approximation is quite different from the CFCA, since the former does not conserve kinetic energy and therefore velocity during the transition.

Both the CFCA and the delta function approximation were tested for use in the inversion of the NaK $1^3\Pi \rightarrow 1^3\Sigma^+$ data by comparison of their results with fully quantum mechanical calculations of the spectra. [The quantum mechanical calculations were carried out using the program Bound-Free.[21] These calculations are described more completely in Ref. 6]. Figure 3 shows such a comparison. Although both approximations reproduce the oscillatory structure, including the correct number of maxima, neither is sufficiently accurate in determining the positions of the maxima and minima for use in obtaining an improved $1^3\Sigma^+$ state experimental potential.

The difficulties encountered by the two approximation techniques described above can be traced to the fact that the overlap of the upper and lower state wavefunctions does not collapse to a delta function in R. In Fig. 4, following Tellinghuisen,[22] we show the accumulated overlap integral as a function of R. From calculations of this type we found that the integrand of the overlap integral can be represented by a "square window". Rather than only a single R value contributing to the overlap integral as in the CFCA and the delta function approximation, the overlap builds up over some finite range of R which is a significant fraction of the width of the upper state well (typically on the order of 20%). Thus, with the fully quantum mechanical calculations, the transition dipole moment is much more difficult to determine because one cannot directly relate a specific R to each wavelength as in the CFCA or delta function approximation. The transition dipole moment at any R will affect the intensity over a fairly broad range of wavelengths which can include several maxima of each oscillatory spectrum. In effect, one must deal with a moving average which is difficult to deconvolve. It is thus impossible to determine fine details within the transition dipole moment using these techniques. However, the finite width of this "window" does not cause any serious problems in the determination of the $1^3\Sigma^+$ repulsive wall above the dissociation energy because one does not need to directly relate wavelength to R in the fitting procedure. Problems of this nature and our results are discussed further in Secs. IV b through d.

III. Experiment

The experimental set-up is shown in Fig. 5. The sodium-potassium mixture was contained in a stainless-steel, five arm, crossed heat-pipe oven.[23] The oven was operated at about 360° C with approximately 2 Torr of argon as a buffer gas. The oven temperature was such that it was near to, but short of, the conditions necessary for true heat-pipe operation.

A single-mode ring-dye-laser with built in wavemeter (Coherent Autoscan CR-699-29), was used for the excitation of NaK. The ring laser, using LD700 dye, was pumped by ~ 7 W from a Kr^+ laser operating at 647.1 nm. This gave the dye laser a tuning range of approximately 700 to 780 nm with between 200 and 300 mW power. The laser wavelength was initially calibrated with the opto-galvanic effect using a Ba hollow-cathode lamp.

Fluorescence was viewed at right angles to the laser excitation axis. Two monochromators were used to disperse the triplet ($1^3\Pi \rightarrow 1^3\Sigma^+$) and singlet ($2^1\Sigma^+ \rightarrow 1^1\Sigma^+$) fluorescence. The triplet fluorescence was resolved using a 1/3 meter monochromator with 1 mm slits (giving a resolution of 7.2 nm), and was detected using a liquid-nitrogen cooled intrinsic germanium detector. The wavelength dependent relative triplet detection system efficiency was calibrated with a quartz-iodine lamp.[24] The correction of the triplet fluorescence spectra for the detection efficiency is important in the determination of D(R) since that determination depends entirely upon relative intensities. A long-pass filter was used in front of

each monochromator to block second and higher order diffractions from the gratings. Singlet band fluorescence was resolved using a 0.5 meter monochromator with 150 μm slits (giving a resolution of .25 nm), and was detected with a photomultiplier of S-1 response. Both monochromators were calibrated with lines from the Ba hollow-cathode lamp.

We were able to take both excitation and fluorescence spectra by the use of two translating mirrors. The mirrors could be positioned to intercept the fluorescence and redirect it to two free standing detectors. These were a Ge detector and a photomultiplier. The monochromators in this case were replaced by interference filters. The filter placed before the free-standing photomultiplier passed light from 0.65 μm to 1.0 μm . As a result this detector acted as a monitor of the total singlet emission. The filter before the free-standing Ge detector passed light from 1.0 μm to 1.6 μm and therefore monitored the total triplet fluorescence. A beam-splitter placed before the heat-pipe sent part of the laser to an iodine cell so we could continuously verify the accuracy of the wavemeter on extended laser scans. The laser was chopped at 200 to 300 Hz and the fluorescence signals were recorded using two lock-in amplifiers.

While using the free-standing detectors, we would scan the laser and observe the total triplet and total singlet fluorescence. The Autoscan laser data acquisition system is limited to 3 input data channels. One channel was used to acquire the vernier etalon scan, which was used

to insure that no mode-hops occurred. The other two were used to acquire the three sets of data we were interested in observing: the total triplet fluorescence, total singlet fluorescence, and fluorescence from the I_2 cell. Thus we carried out two excitation scans in each region of interest. First, we would record an excitation scan of the singlet fluorescence with the I_2 signal. Then we would repeat the scan, recording the total triplet spectrum with the singlet spectrum. Following this, we would fix the laser wavelength to a position where the relative triplet to singlet intensity was high. Under these conditions, the laser was presumably tuned to a strongly perturbed level. We would then translate the movable mirrors out of the way and record spectrally resolved fluorescence. Again two lock-ins were used. The excitation scans were directly recorded by the laser's computer, while the fluorescence spectra were recorded both on chart recorder and on computer.

IV. Results

a. Spectra

Figure 6 shows an example of a composite excitation spectrum. Each spectrum contains an etalon scan, a total triplet fluorescence scan, a total singlet fluorescence scan, and an I_2 scan, each as a function of laser frequency. The total triplet fluorescence trace follows the total singlet, nearly peak for peak. This is due to collisional transfer from the pumped singlet level

to nearby levels of the $1^3\Pi$ state. For fixed laser wavelengths, the resolved singlet spectra consist of series of P-R doublets extending from near the laser frequency to about 1.0 μm , (part of which is shown for one case in Fig. 7). The triplet spectra (see Fig. 8) consist of oscillatory continua, which are characteristic of bound-free reflection structure.

The singlet spectra can be assigned to the NaK molecule after measuring the energy separations between adjacent P-R doublets. The energy separation between the lines depends entirely upon the energy levels of the NaK ground state. The ground states of NaK, K_2 and Na_2 (which are all present in the vapor) are sufficiently different to allow distinction. (In fact, almost all observed fluorescence signals could be assigned to NaK. This is because potassium tends to be pushed out of the central region of the oven where the fluorescence is produced, so that the K_2 concentration is low in that region. In addition, Na_2 does not absorb strongly at these excitation wavelengths.) The triplet bound-free emission can be unambiguously assigned to NaK since the analogous $1^3\Pi \rightarrow 1^3\Sigma^+$ transitions in Na_2 and K_2 are forbidden by symmetry considerations. (The analogous states in the homonuclear molecules are designated as $1^3\Pi_u$ and $1^3\Sigma^+_u$, and u→u transitions are strictly forbidden.) Since all signals are linear in laser power, the upper state must lie in the first excited manifold of states.

b. Analysis of spectra

The excitation spectra are very complex since there are so many thermally populated levels of the ground state. In general, these spectra were used simply to locate levels with a large triplet amplitude.

In order to assign v and J for the pumped $1^3\Pi$ level, which was needed to model the bound-free emission, we analyzed the associated singlet band emission. Since levels which produce enhanced triplet fluorescence are probably spin-orbit perturbed, these $1^3\Pi_\Omega$ levels have an admixture of $2^1\Sigma^+$ probability amplitude which allows population from the ground state. This $2^1\Sigma^+$ amplitude also results in downward transitions to the $1^1\Sigma^+$ state [$2^1\Sigma^+(v',J') \rightarrow 1^1\Sigma^+(v'',J'\pm1)$] obeying the selection rule, $\Delta J = \pm 1$. The singlet spectra consist of a series of P-R doublets (see Fig. 7) which can be analyzed to yield the assignments of v'' and J'. In particular the P and R line splitting within a doublet roughly identifies J', while the splitting between doublets yields the various values of v''. In practice, both quantities depend upon both v'' and J', so assignments were made by comparison of a list of $1^1\Sigma^+(v'',J'-1)$, $1^1\Sigma^+(v'',J'+1)$ energy differences with the observed P-R splittings, and by comparison of a list of $1^1\Sigma^+(v'',J'')$, $1^1\Sigma^+(v''+1,J'')$ energy differences with observed splittings between doublets. The energy differences were generated from the constants of Ref. 16.

Once the assignments of J' and the various v'' were made, it was easy to determine the

level of the ground state which was pumped by the laser. A search program identified all possible levels of the $2^1\Sigma^+$ state which could be pumped from the initial $1^1\Sigma^+$ ro-vibrational level given the laser wavelength, the unperturbed $2^1\Sigma^+$ level energies (from Ref. 17), and an energy error or tolerance. The energy error, typically chosen to be 5 cm^{-1} , was needed to cover possible perturbation-induced deviations from the unperturbed energy positions.

Since the $2^1\Sigma^+$–$1^3\Pi$ perturbations only involve states of the same J, it is straightforward to assign the Ω, v, and J values to the mixed state's $1^3\Pi_\Omega$ probability amplitude. This was done using a second search program which found the closest unperturbed $1^3\Pi_\Omega$ level with the *same J' value as the pumped* $2^1\Sigma^+$ level. We identified triplet emission from all fine-structure levels of the $1^3\Pi$ state. However, most of the spectra analyzed involved $1^3\Pi_0$–$2^1\Sigma^+$ perturbations which give rise to the strongest triplet fluorescence. This is because the spin-orbit operator only couples the $2^1\Sigma^+$ levels to those of the $1^3\Pi_0$. The $2^1\Sigma^+$ levels are also coupled to $1^3\Pi_1$ and $1^3\Pi_2$ levels, but only through more complex secondary perturbations. Table 1 shows the v, J levels of the $1^1\Sigma^+$, $2^1\Sigma^+$, and $1^3\Pi_\Omega$ states which were coupled by the laser for specific pump wavelengths.

As an additional check, we verified that the observed shift of a mixed level from its unperturbed position was consistent with the assigned perturbation; i.e. that the higher of the two levels was shifted up in energy or the lower of the two levels shifted down. We found

that most of the chosen pumped levels were perturbed triplets (triplet amplitude greater than singlet amplitude) since these levels generally give rise to the largest triplet fluorescence.

The largest error in the above procedure results from inaccuracy in the $1^3\Pi_0$ state constants which were used in predicting the unperturbed energies for that state. These constants were derived from the highly accurate $1^3\Pi_1$ state constants of Ref. 15, together with the measured fine-structure constant from the same reference: $\left\{E\left[1^3\Pi_1(v,J)\right] - E\left[1^3\Pi_0(v,J)\right] = 15.557\ \text{cm}^{-1} - 0.0112\ (v+\frac{1}{2})\ \text{cm}^{-1}\right\}$. This is not very satisfactory for our purposes, and we estimate that neglect of higher order terms leads to an error of as much as $1\ \text{cm}^{-1}$ in the unperturbed $1^3\Pi_0$ energies. (This estimate was made by comparing calculated energies for the $1^3\Pi_2$ levels using the $1^3\Pi_1$ level energies and the fine-structure constant of Ref. 15, with more accurate values which include higher order terms.[25]) This uncertainty has a negligible effect on our determination of the $1^3\Sigma^+$ repulsive wall (see next section), but makes it difficult to study the perturbations themselves.

In principle, it should be possible to determine the electronic contribution to the spin-orbit interaction matrix element, ξ_{el}:[14]

$$\langle\Psi_{1^3\Pi_0}|H_{SO}|\Psi_{2^1\Sigma^+}\rangle = \xi_{el}\langle\Psi_{1^3\Pi_0}|\Psi_{2^1\Sigma^+}\rangle, \qquad (2)$$

where $\Psi_{1^3\Pi_0}$ and $\Psi_{2^1\Sigma^+}$ are radial wavefunctions. By ignoring interactions between $1^3\Pi_{2,1}$ and $1^3\Pi_0$ levels, we can construct a simple interaction matrix involving only the $1^3\Pi_0$ and $2^1\Sigma^+$

states:[18]

$$\begin{bmatrix} E_\Sigma & \xi_{el}\langle\Psi_{1^3\Pi_0}|\Psi_{2^1\Sigma^+}\rangle \\ \xi_{el}\langle\Psi_{2^1\Sigma^+}|\Psi_{1^3\Pi_0}\rangle & E_\Pi \end{bmatrix}, \tag{3}$$

where E_Σ and E_Π are the unperturbed energies. Diagonalizing the matrix gives an expression for the perturbed energies, E_+ and E_-:[18]

$$E_\pm = \frac{E_\Pi+E_\Sigma}{2} \pm \frac{1}{2}\left[\left(E_\Pi-E_\Sigma\right)^2 + 4\xi_{el}^2|\langle\Psi_{1^3\Pi_0}|\Psi_{2^1\Sigma^+}\rangle|^2\right]^{\frac{1}{2}}. \tag{4}$$

Determination of ξ_{el} therefore requires knowledge of 3 of the 4 quantities, E_Σ, E_Π, E_+ and E_-. In the present experiment, we accurately know one of the perturbed energies and E_Σ. Unfortunately, we were unable to locate the second perturbed level with the techniques employed. This, combined with the above-mentioned uncertainties in E_Π, made it impossible to determine ξ_{el} accurately since a perturbation typically results in shift of only .5 cm^{-1}.[14] Work to further investigate these perturbations is currently in progress.

c. Determination of the $1^3\Sigma^+$ potential above the dissociation energy

Having determined the particular ro-vibrational level of the $1^3\Pi_\Omega$ state which is populated at a specific laser wavelength through perturbations with the $2^1\Sigma^+$ state, we can proceed with the determination of the $1^3\Sigma^+$ repulsive wall above the dissociation limit. Our procedure was to assume a repulsive potential of a certain form with free parameters, quantum-mechanically simulate the oscillatory spectra using this potential, and vary the parameters of the potential to

obtain the best agreement between observed and calculated spectra (i.e. positions of the oscillatory maxima and minima). We chose to fit the repulsive wall by a function of the form $Ae^{-BR}+C$. This form for V(R) was used previously by LeRoy et al.[8] to describe this same $1^3\Sigma^+$ repulsive potential in a fit of bound-free fluorescence from a higher triplet state ($2^3\Pi$). In their work, the fitted potential was required to join smoothly with the experimentally determined bound portion of the $1^3\Sigma^+$ state;[16] i.e. both the function and its first derivative were made continuous at the junction. This effectively reduces the fit to one parameter, since the continuity of the potential, and the continuity of the derivative each eliminate one degree of freedom. The final free parameter is then obtained by requiring the best match to the spectra. We attempted to obtain "one-parameter" fits using the forms $Ae^{-BR}+C$ and $\frac{A}{R}e^{-BR}+C$. However, we were unable to obtain a good match (within experimental error) to observed spectra from both high and low v levels of the $1^3\Pi$ state using the same values for the parameters. In order to fit all of our data, we dropped the requirement of a continuous derivative of the repulsive wall potential with the known $1^3\Sigma^+$ bound well. This resulted in what is effectively a two-parameter fit. We believe this is acceptable since our data does not detail the region of the "wall" to well junction.

The simulations of the bound-free spectra were fully quantum mechanical and were carried out for the specific levels of the $1^3\Pi_\Omega$ state which were previously determined to be the

levels pumped in the experiment. The calculations were carried out using the program Bound-Free.[21,26] The program utilized the assumed form of the $1^3\Sigma^+$ repulsive wall in conjunction with the experimental $1^3\Pi_\Omega$, and bound portion of the $1^3\Sigma^+$ potential energy curves. These latter two were calculated using a spline fit to the RKR rotationless potential obtained from the experimentally determined term values in Refs. 15 and 16. For the $1^3\Pi_\Omega$ states, we determined turning points for $v = -\frac{1}{2}$ to 50, yielding a range in R of 2.5145 to 5.7223 Å. For the $1^3\Sigma^+$ we determined turning points for $v = -\frac{1}{2}$ to v = 7, yielding a range in R of 4.6452 to 9.0780 Å. We limited the inner turning point of the $1^3\Sigma^+$ state to R = 4.6452 Å because at R's near the dissociation energy, the turning points become unreliable as generated by the RKR procedure. P, Q, and R transitions were all included in the simulations, which causes a slight broadening of the oscillatory maxima, but little change in intensity at the minima. However, the instrument function of the monochromator does significantly increase the intensity at the minima in the experimental spectra. In order to take this into account, we convoluted the simulated spectra with a triangular instrument function of 7.2 nm full-width-half-maximum, corresponding to the measured monochromator resolution. This procedure resulted in good agreement of the intensities at the minima. Each simulated spectrum involved calculation of the intensity at 200 wavelengths to cover the observed region. Because we are simulating spontaneous emission dispersed on a linear wavelength scale, a weighting factor of λ^{-6} was

used. All calculations were made using a theoretical determination of the transition dipole moment, D(R),[27] since the experimental transition dipole moment function was yet to be determined. The effect of using this theoretical D(R) was later seen to shift the calculated peak positions by an amount which was less than our experimental error.

For each simulation, the parameters for A and B were estimated, while C was determined by tying on to the $1^3\Sigma^+$ experimental potential at R = 4.6452 Å. A and B were then varied until the simulations were consistent with our data. This procedure converged fairly quickly since the effects of the $1^3\Sigma^+$ state repulsive wall parameters were very clear in the calculations. If the oscillations in the calculated spectrum were too spread out at short wavelength, then the trial $1^3\Sigma^+$ state wall was not sufficiently steep. Conversely, if the oscillations in the calculated spectrum were too close at short wavelength, then the trial potential was too steep. Our reported best fit potential was, of course, required to simultaneously fit all experimental spectra which were analyzed within experimental error.

We found that, in the present case, the emission from higher v levels of the $1^3\Pi_\Omega$ states was less sensitive to the shape of the $1^3\Sigma^+$ potential over the range of R studied, than emission from lower v levels. This is because all information about the shape of the $1^3\Sigma^+$ potential repulsive wall is contained within the lower ($1^3\Sigma^+$) state wavefunction $\Psi_L(R)$, which is most sensitive to the shape of the potential for R values near the turning point. [The oscillation

wavelength of $\Psi_L(R)$ is determined by the kinetic energy $\frac{p^2}{2m}$ at R, and the de Broglie relation $\lambda=\frac{h}{p}$. Relative changes in λ due to changes in V(R) (and therefore $\frac{p^2}{2m}$ at R) are greatest when kinetic energy is smallest; i.e. near the turning point. Alternatively, looking at it from a mathematical standpoint, the solution to the Schroedinger equation for the lower state wavefunction $\Psi_L(R)$ is most sensitive to the boundary conditions for positions near the boundary.] In the present case, for higher v′ levels, the principal contribution to the intensity at λ comes from larger R values and thus from regions farther from the $1^3\Sigma^+$ repulsive wall. Therefore our derived potential is most sensitive to spectra obtained fom the lower v′ levels. In the more general case, the repulsive potential at R is most accurately determined by emission from a bound vibrational state with either of its turning points (inner or outer) close to R.

From detailed comparison of simulated and observed NaK $1^3\Pi\rightarrow1^3\Sigma^+$ spectra, we report our best fit for the $1^3\Sigma^+$ repulsive wall potential of the form $V(R)=Ae^{-BR}+C$: A = 6.0×10^5 cm^{-1} , B = 1.605$Å^{-1}$, C = –223.990 cm^{-1} . We note that because we are only able to observe the bound-free emission out to about 1.6 μm with the intrinsic germanium detector, we can only accurately map the $1^3\Sigma^+$ potential to a point ~ 2000 cm^{-1} above the dissociation energy. [This limit is obtained by subtracting the energy of a 1.6 μm photon from the energy of the highest $1^3\Pi_\Omega$ level producing observed and analyzed emission.]

In Fig. 9 we have compared our experimental $1^3\Sigma^+$ repulsive wall with those of LeRoy et al[8] and the calculated potential of Stevens et al.[28] We note that our data could not be accurately fit by the LeRoy or Stevens' potentials. We believe the small discrepancy between our potential and those of LeRoy et al. has nothing to do with the approach used in either case, but simply reflects the lack of an accurate experimental characterization of the $2^3\Pi$ state and the use of only one bound-free spectrum in their analysis.

d. Relative transition dipole moment function, D(R)

The transition dipole moment function, D(R) is reflected in the relative intensities of the various maxima in the oscillating continua. However, determination of this function proved to be more difficult than that of the $1^3\Sigma^+$ state potential. Initially, we tried to use the CFCA to directly relate a particular emission wavelength to a particular R. Since the CFCA assumes that the dipole moment varies slowly enough to be pulled out of the integral in Eq. 1, the intensity is proportional to $|D(R)|^2$. We could then obtain a relative dipole moment function, $D(R)^{rel}$ from the following formula:[8]

$$D(R)^{rel} = \left[\frac{I(\lambda)^{obs}}{I(\lambda)^{(D=1)}}\right]^{\frac{1}{2}}. \qquad (5)$$

This procedure, based upon the CFCA proved unsuccessful. The problem occurs because the CFCA assumes that the wavefunction overlap is localized at a particular R, when in fact it

occurs over a relatively broad region of R. This means that a fairly wide region of R contributes to each emission wavelength. In fact, the dipole moment at any R can contribute to several intensity maxima in a given spectrum. A trial and error approach is also unsatisfactory, as it is not obvious how to adjust D(R) to correct for errors in the calculated spectrum.

Our eventual resolution of these difficulties came from looking at accumulated overlap integrals similar to those shown in Fig. 4. These tell us the range of R values which contribute to a given wavelength. We model this range as a square "window" which was determined for each peak in the spectra. The average R of each of these windows then relates the internuclear separation to a corresponding λ, similar to the CFCA. However, these $R(\lambda)$'s are not the same as those given by the CFCA. As in the CFCA, we have assumed that D(R) is sufficiently slowly varying to allow it to be removed from within the integral of Eq. 1. Since these integration "windows" are broad, they will wash out any small details in D(R). Thus we were unable to determine such details using a formula equivalent to Eq. 5. We began our fitting procedure with the highest v′ spectrum, since the higher the pumped v′ level, the farther to the blue the bound-free emission extends, and the larger R for which D(R) can be determined. We assumed a dipole moment function of the form $D(R) = D_0[mR-1]$ and obtained a value for the parameter m. A second spectrum, corresponding to the next highest v′, was then included in the fit. The dipole moment calculated from the second spectrum was normalized at an R

corresponding to its short wavelength maximum to the dipole moment obtained from the first spectrum at that R. We combined all the spectra in this fashion. This enabled us to determine parameters for D(R) which provide a best fit to the data. The determined best parameter for D(R) in relative units is m = 1.243 $Å^{-1}$. We had simultaneously proceeded with a trial and error fit of a linear D(R) function. The systematic procedure described above agrees quite well with our best trial and error fit, increasing our confidence in it. This transition dipole moment is plotted in Fig. 10 where it is compared to the theoretical result of Ratcliff et al.[27] Since our function is just relative, we have normalized our D(R) to that of Ratcliff at R = 4.25 Å (i.e. $D_0 = 2.116\times10^{-20}$CÅ). Because of the limited wavelength range of our spectra, the transition dipole moment we determined is limited to a region between 3.70 and 4.80 Å.

Figure 11 shows a comparison of several experimental spectra with the relevant simulated spectra calculated using the $1^3\Sigma^+$ repulsive wall determined as outlined in the previous section and the transition dipole moment determined as discussed in this section.

e. Comparison of "exact" experimental $1^3\Sigma^+$ potential to results of reflection approximations

There has been much interest in reflection approximations and efforts have been made to find a new reflection method which will correctly give the positions of the maxima and minima of bound-free spectra. In their very recent paper, Eryomin and Kuz'menko [29] have developed

several new methods for determining bound-free spectra by reflection of the upper bound state nuclear probability function ($\Psi_U^*(R)\Psi_U(R)$). Of the three methods proposed, one permits the straight-forward inversion of bound-free spectra to determine the lower unbound state potential, if the upper state potential and energy level are known. The method lies between the two semi-classical approximations previously described; the CFCA and the delta-function approximation.

Rather than conserving all the initial state kinetic energy as in the CFCA, or losing all kinetic energy as in the delta-function approximation, the Eryomin and Kuz'menko method retains one third of the kinetic energy:

$$\frac{hc}{\lambda} = E_U - \left[V_L(R) + \frac{1}{3}\left[E_U - V_U(R)\right]\right], \tag{6}$$

with E_U = the upper state energy, V_U = the upper state potential, and V_L = the lower state potential. As in the other two approximations, the emission intensity is proportional to the probability that the atomic pair is separated by the appropriate R. This approximation is justified by the same reasoning as used in the delta-function approximation. However, Eryomin and Kuz'menko note that the first large maxima of the lower state wavefunction does not occur at the turning point (as assumed in the delta-function approximation), but is offset from that point by a small amount in R. The effect of this offset is approximated by the preservation of one third of the kinetic energy. It can be seen that this approximation is

intermediate between the CFCA and the delta-function approximations. Figure 12 compares the potentials determined using the CFCA, the delta-function approximation, and the Eryomin and Kuz'menko approximation with the potential determined here by fully quantum mechanical methods. Figure 3 shows a comparison of spectra calculated using the delta function approximation, the CFCA, the Eryomin and Kuz'menko approximation, and a fully quantum mechanical calculation, for fixed potential curves. We believe these results demonstrate that the Eryomin and Kuz'menko approximation offers an improvement over the delta function approxmation and the CFCA. We note that the spectra observed in the present work are sensitive to a region of the lower state potential where the slope is not very steep. Under these conditions, all the above reflection methods are less accurate than if the potential were steeper. In particular, it can be seen in Fig. 12 that the potential obtained from the Eryomin and Kuz'menko method agrees well with the quantum-mechanical result at small R where the potential becomes steeper.

IV Conclusion

In summary, we have observed NaK $1^3\Pi_\Omega \rightarrow 1^3\Sigma^+$ bound-free emission from specific ro-vibrational levels of the $1^3\Pi_\Omega$ states. We have carried out quantum mechanical simulations of the emission spectra based upon experimentally determined potentials for the $1^1\Sigma^+$, $2^1\Sigma^+$, $1^3\Pi_1$, and $1^3\Sigma^+$ states, and the $1^3\Pi$ fine structure constant. Using these

simulations, we were able to fit the repulsive wall of the $1^3\Sigma^+$ state above the dissociation limit by a potential of the form $Ae^{-BR}+C$. We were also able to crudely determine the $1^3\Pi \rightarrow 1^3\Sigma^+$ relative transition dipole moment function by comparing measured relative intensities of the oscillatory bound-free emission maxima to those of simulations. In the latter, a linear dependence $D(R) = D_0 (mR - 1)$ was assumed.

At present, we are involved in extending our detection system's sensitivity further to the red in order to extend our experimental $1^3\Sigma^+$ potential to shorter R. We also hope to determine the lifetimes of perturbed states, which will allow us to place our experimental dipole moment function on an absolute basis. Finally, we are in the process of determining the perturbation strength, ξ_{el} by finding both levels of each mutually perturbing pair.

Acknowledgments

We would like to thank Dr. Joel Tellinghuisen and Dr. Robert LeRoy for useful discussions. This work was supported by the U. S. Army Research Office under Grants DAAL03-86-K-0161 and DAAL03-89-K-0171, and the National Science Foundation under Grant PHY-8451279. In addition, we are grateful for equipment provided under the Defense University Research Instrumentation Program, Grant DAAL03-88-0063.

References

1. E. J. Breford and F. Engelke, *Chem. Phys. Lett.*, **53** , 282, (1978).

2. E. J. Breford and F. Engelke, *J. Chem. Phys*, **71** , 1994, (1979).

3. D. Eisel, D. Zevgolis, and W. Demtröder, *J. Chem. Phys.*, **71** , 2005, (1979).

4. H. Kato and C. Noda, *J. Chem Phys*, **73** , 4940, (1980).

5. J. Huennekens, T.G. Walker, and S.C. McClain, *J. Chem Phys*, **83** , 4949, (1985).

6. J. Huennekens, A. Loza, M. Masters, and K. M. Sando, *J. Chem. Phys.*, **88** , 6013, (1988).

7. M. S. Child, H. Essen, and R. J. LeRoy, *J. Chem. Phys.*, **78** , 6732, (1983).

8. R. J. LeRoy, W. J. Keogh, and M. S. Child, *J. Chem. Phys.*, **89** , 4564, (1988).

9. D. D. Konowalow and P. S. Julienne, *J. Chem. Phys.*, **72,** 5815, (1980).

10. O. C. Mullins, C. R. Mahon, and T. F. Gallagher, *Chem. Phys. Lett.*, **126,** 501, (1986).

11. A. J. Ross, P. Crozet, C. Effantin, J. d'Incan, and R. F. Barrow, *J. Phys. B: At. Mol. Phys.*, **20,** 6225, (1987).

12. L. Li and R. W. Field, *J. Mol. Spectrosc.*, **123,** 237, (1987).

13. H. Kato, M. Otani, and M. Baba, *J. Chem. Phys.*, **89** , 653, (1988).

14. C. Effantin, O. Babaky, K. Hussein, J. d'Incan, and R. F. Barrow, *J. Phys. B: At. Mol.*

Phys.,

18, 4077, (1985).

15. A. J. Ross, C. Effantin, J. d'Incan, and R. F. Barrow, *J. Phys. B: At. Mol. Phys.*, **19,** 1449, (1986).

16. A. J. Ross, C. Effantin, J. d'Incan, and R. F. Barrow, *Mol. Phys.*, **56 ,** 903, (1985).

17. A. J. Ross, R. M. Clements, and R. F. Barrow, *J. Mol. Spectrosc.*, **127,** 546, (1988).

18. G. Herzberg, *Molecular Spectra and Molecular Structure: I. Spectra of Diatomic Molecules.*, Van Nostrand Reinhold Company, New York, (1950).

19. E. U. Condon, *Proc. Nat. Acad. Sci.*, **13,** 462, (1927).

20. R. S. Mulliken, *J. Chem. Phys.*, **55,** 309, (1971).

21. P. S. Herman and K. M. Sando, *Program Bound-Free.* University of Iowa, Dept. of Chem. (unpublished).

22. J. Tellinghuisen, *J. Mol. Spectrosc.*, **103,** 455, (1984).

23. C. R. Vidal and J. Cooper, *J. Appl. Phys.*, **40 ,** 3370, (1969).

24. R. Stair, W. E. Schneider, and J. K. Jackson, *Appl. Opt.*, **2 ,** 1151, (1963).

25. A. J. Ross, *Private communication.*

26. P. S. Herman and K. M. Sando, *J. Chem. Phys.*, **68,** 1153, (1978).

27. L. B. Ratcliff, D. D. Konowalow, and W. J. Stevens, *J. Mol. Spectrosc.*, **110,** 242, (1985).

28. W. J. Stevens, D. D. Konowalow, and L. B. Ratcliff, *J. Chem. Phys.*, **80 ,** 1215, (1984).

29. V. V. Eryomin and N. E. Kuz'menko, *Chem. Phys.*, **136,** 127, (1989).

Captions

Fig. 1. Lowest six NaK molecular potential curves. Note that throughout the text the notation $2^1\Sigma^+$ refers to the second lowest $^1\Sigma^+$ state, etc.

Fig. 2. a) Origin of bound-free oscillatory spectra according to the CFCA, in which both position and kinetic energy are conserved. For each internuclear separation R there is a corresponding unique wavelength, and the intensity at that wavelength is proportional to the probability distribution in the bound upper state. The dashed curve represents the lower state potential plus the upper state kinetic energy (Mulliken difference potential). Transitions at two R values are represented by arrows. b) Oscillatory spectra according to the delta function approximation. Again the oscillations reflect the probability distribution of the upper state, but here the kinetic energy is not conserved. Instead the lower state wave function is represented by a delta function at the clasical turning point.

Fig. 3. Comparison of theoretical NaK $1^3\Pi_1(v'=18,J'=37)\rightarrow 1^3\Sigma^+$ emission calculated using four different methods: a) delta function approximation, b) CFCA, c) Eryomin and Kuz'menko approximation, and d) fully quantum-mechanical claculation. For all the calculations the experimental $1^3\Pi_1$, and bound portions of the $1^3\Sigma^+$ potential energy curves from Refs. 15 and 16 were used, in conjunction with the $1^3\Sigma^+$ repulsive wall determined in the present work. All

four calculations predict the correct total number of oscillations which extend to very long wavelengths (~ 4.3 μm). Here, the calculations were cut off at 1.6 μm corresponding to the cutoff of the detector sensitivity in the experiment.

Fig. 4. Wavefunctions, integrand, and accumulated overlap integral for the first a) and third b) maximum (from the left) of the spectrum shown in Fig. 10 d). The $1^3\Pi_0$ level is $v' = 10$, $J' = 38$. Note that the width of the region where the integral accumulates increases as it moves to smaller R values.

Fig. 5. Experimental setup. IF and PMT represent interference filter and photomultiplier, respectively.

Fig. 6. Excitation spectra. a) laser etalon signal indicating the continuity of the scan. b) total triplet band emission. c) total singlet emission. d) I_2 fluorescence. The arrow in b) indicates a position of enhanced triplet emission and therefore a perturbed energy level.

Fig. 7. P-R doublets of the downward $2^1\Sigma^+(v'=20, J'=37) \rightarrow 1^1\Sigma^+(v'', J''=36, 38)$ transitions. The upper state was pumped from the $v''=0$, $J''=36$ level of the $1^1\Sigma^+$ state. Typically these P-R doublets extend to approximately 1.0 μm .

Fig. 8. Bound-free emission from the $1^3\Pi_1$(v′=18, J′=37) level.

Fig. 9. A comparison of the $1^3\Sigma^+$ repulsive wall calculated in the present work (solid line, R < 4.5Å), with those calculated by LeRoy et al. in Ref. 8 (the two short, dashed lines), and the calculated potential of Stevens et al. from Ref. 28 (long dashed curve). The solid curve for R > 4.5Å is the experimental bound portion of the $1^3\Sigma^+$ state from Ref. 16.

Fig. 10. Comparison of the relative dipole moment calculated in the present work (line between two *) with the theoretical dipole of Ratcliff et. al. [27] (full line). The experimental D(R) was normalized to the Ratcliff et. al. result at R = 4.25 Å. The flat line to the right represents the asymptotic theoretical dipole moment.

Fig. 11. Comparison of quantum-mechanical calculated spectra with experimental spectra. Each spectrum is generated from a single ro-vibrational level of the $1^3\Pi_\Omega$ states: a) Ω=0, v′=21, J′=31. b) Ω=1, v′=18, J′=37. c) Ω=0, v′=15, J′=16. d) Ω=0, v′=10, J′=38. In part a) the first peak in the calculated spectrum is cut off, since that part of the spectrum represents bound-bound $1^3\Pi_0 \rightarrow 1^3\Sigma^+$ emission which is not handled by the program Bound-Free.

Fig. 12. $1^3\Sigma^+$ state potentials calculated from the various reflection techniques using the observed spectra and compared to the quantum-mechanical result of the present work. Sym-

bols are as follows: (*) represents the delta function approximation, (□) the CFCA, (◇) the Eryomin and Kuz'menko approximation[29], and (△) represents the present work.

Laser Energy (cm^{-1})	$1^1\Sigma^+$ (v, J)	$2^1\Sigma^+$ (v, J)	$1^3\Pi$ (Ω, v, J)
13949.86	4, 45	32, 46	1, 26, 46
13788.32	1, 30	24, 31	0, 21, 31
13698.69	0, 28	21, 29	0, 19, 29
13606.73	0, 36	20, 37	1, 18, 37
13572.02	0, 47	20, 46	0, 18, 46
13569.45	0, 63	21, 62	1, 18, 62
13488.05	0, 23	18, 24	0, 17, 24
13269.68	0, 15	15, 16	0, 15, 16
12939.08	0, 37	11, 38	0, 12, 38
12713.26	0, 37	10, 38	0, 10, 38

Table 1

NaK levels coupled by the laser for specific pump frequencies which produced spectra analyzed in the present work. In each case, the initial state is $1^1\Sigma^+(v,J)$ with v and J given in the table. The final state is an admixture of $2^1\Sigma^+(v,J)$ and $1^3\Pi_\Omega(v,J)$ levels with Ω, v, and J given in the table for both components (Ω=0 for the $2^1\Sigma^+$ state).

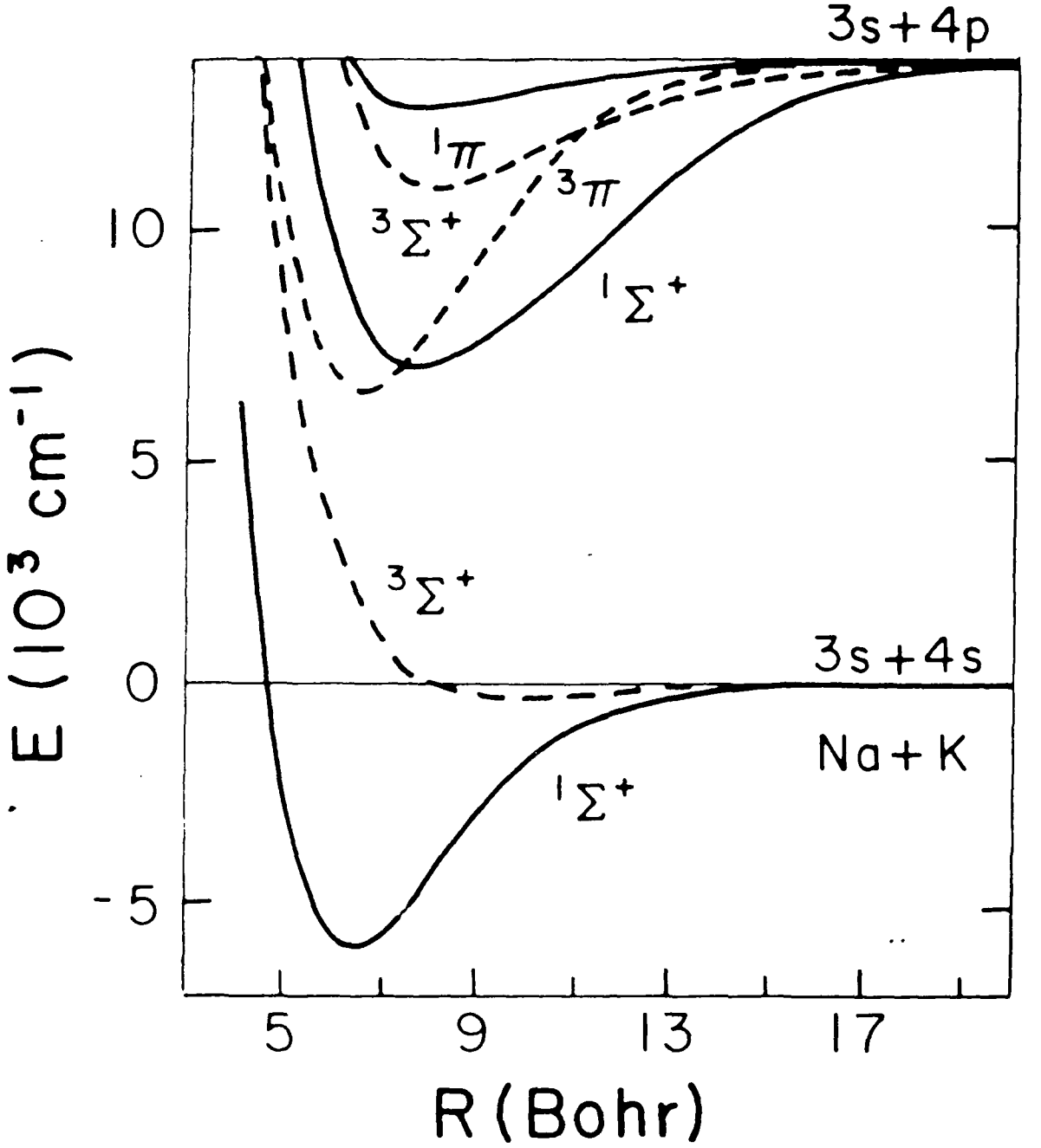
3s+4p
$^1\pi$
$^3\pi$
$^3\Sigma^+$
$^1\Sigma^+$
$^3\Sigma^+$
3s+4s
Na+K
$^1\Sigma^+$
10
5
0
-5
E (10^3 cm^{-1})
5
9
13
17
R (Bohr)

Fig. 1

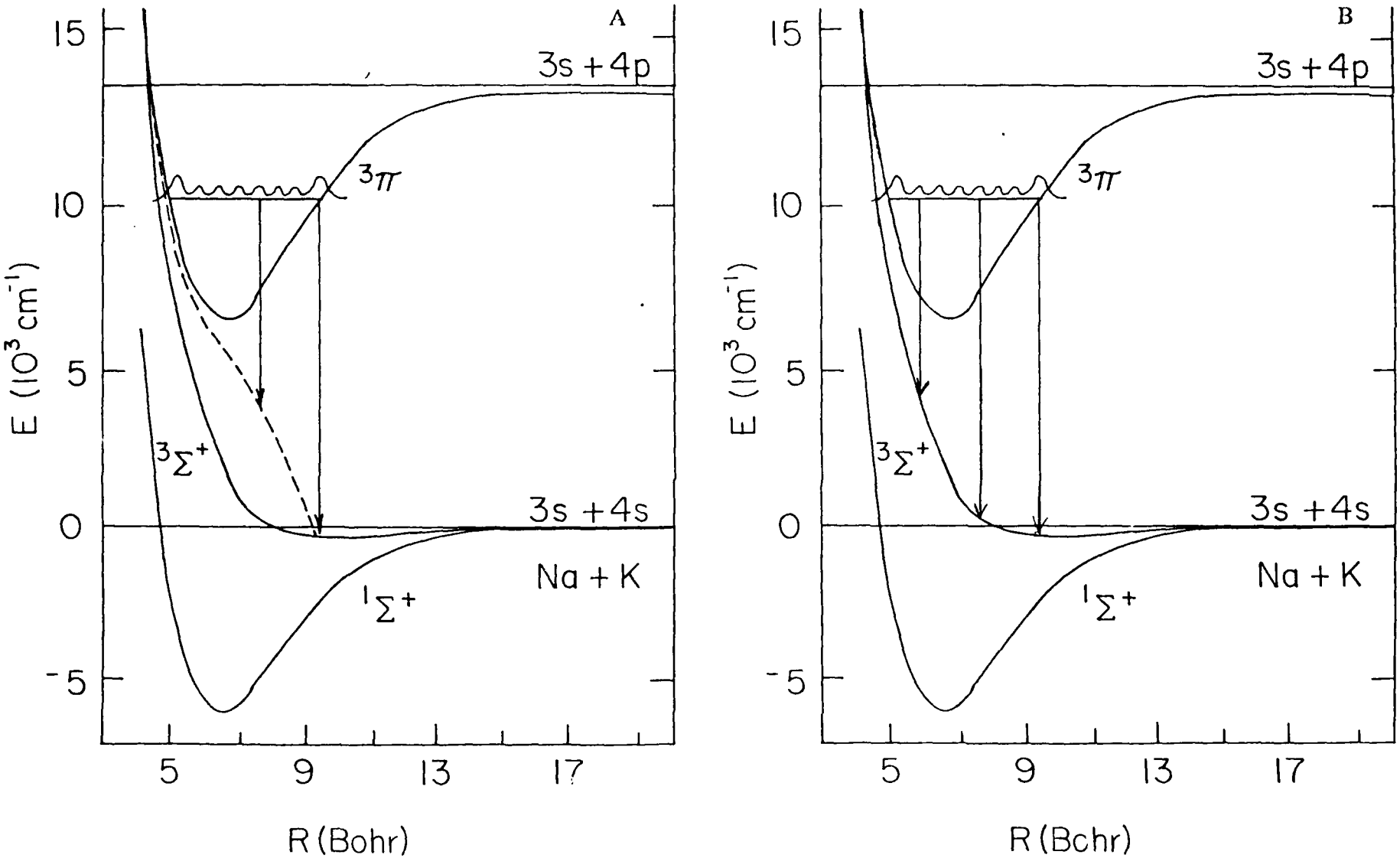
A
B
15
10
5
0
-5
E (10^3 cm^{-1})
3s + 4p
3s + 4s
Na + K
$^3\pi$
$^3\Sigma^+$
$^1\Sigma^+$
5
9
13
17
R (Bohr)

Fig. 2

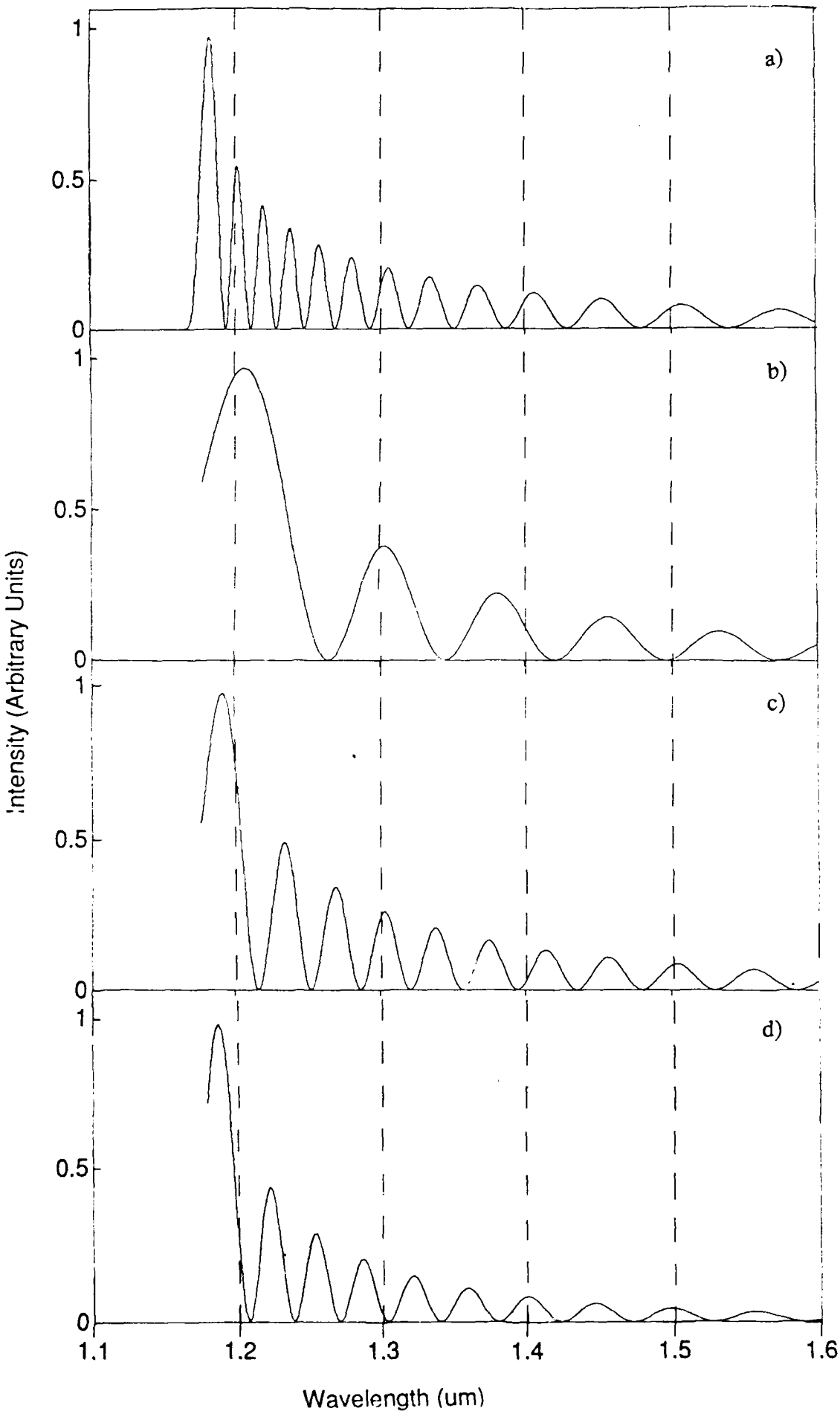
a)
b)
c)
d)
1
0.5
0
Intensity (Arbitrary Units)
1.1
1.2
1.3
1.4
1.5
1.6
Wavelength (um)

Fig. 3

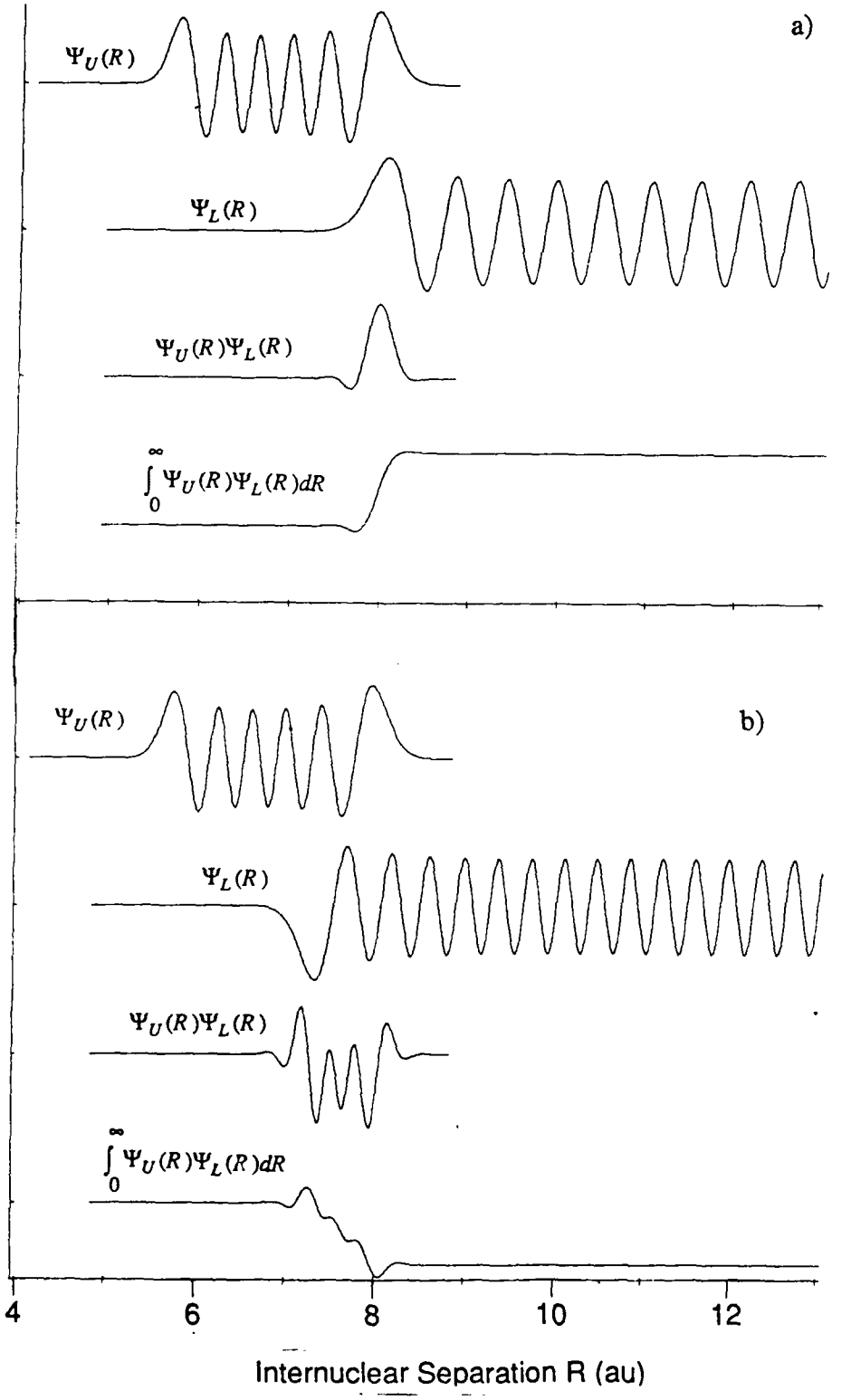
a)
$\Psi_U(R)$
$\Psi_L(R)$
$\Psi_U(R)\Psi_L(R)$
$\int_0^\infty \Psi_U(R)\Psi_L(R)dR$
b)
$\Psi_U(R)$
$\Psi_L(R)$
$\Psi_U(R)\Psi_L(R)$
$\int_0^\infty \Psi_U(R)\Psi_L(R)dR$
4
6
8
10
12
Internuclear Separation R (au)

Fig. 4

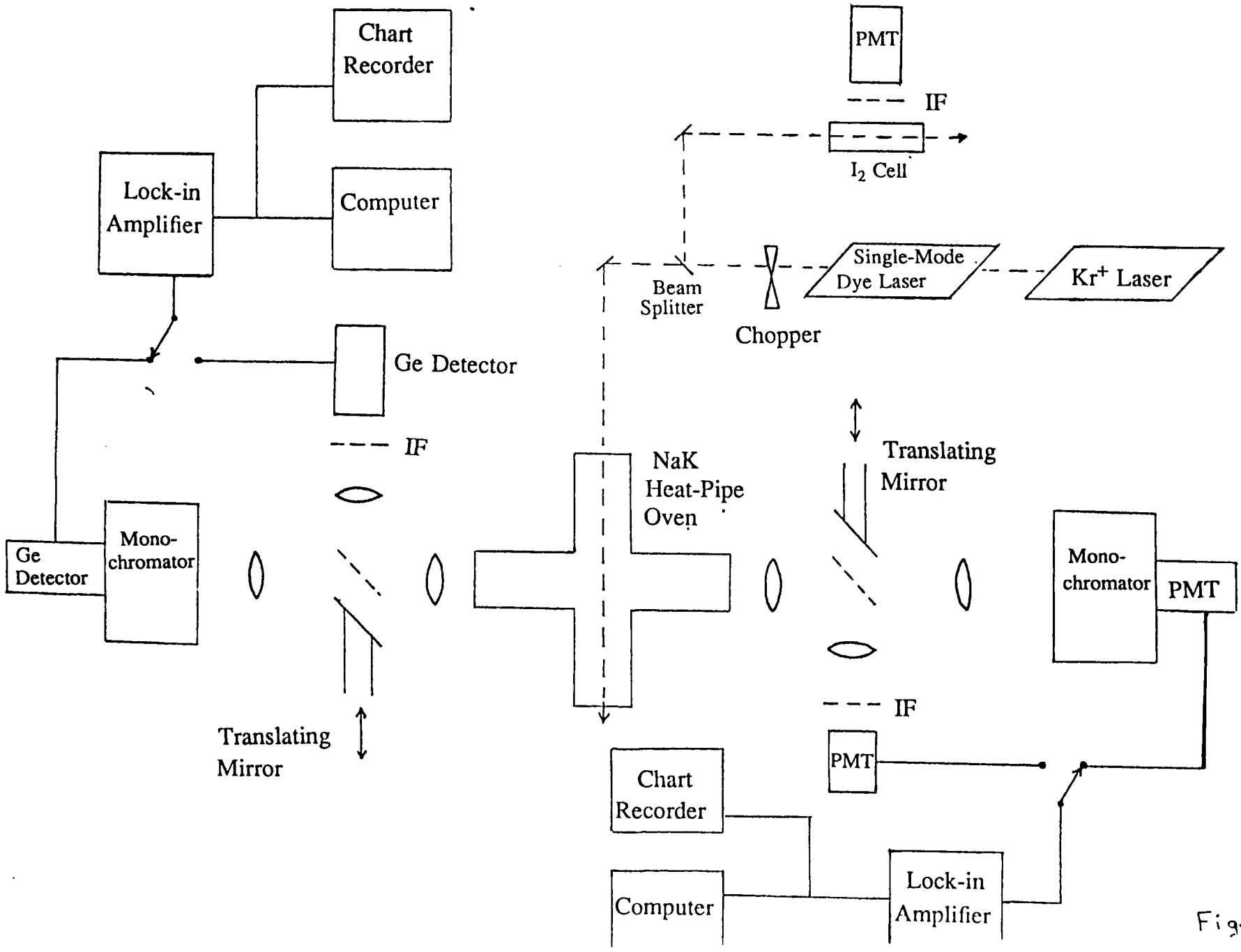
Chart Recorder
Lock-in Amplifier
Computer
Ge Detector
IF
Ge Detector
Mono-chromator
Translating Mirror
PMT
IF
I_2 Cell
Beam Splitter
Chopper
Single-Mode Dye Laser
Kr^+ Laser
NaK Heat-Pipe Oven
Translating Mirror
Mono-chromator
PMT
IF
PMT
Chart Recorder
Computer
Lock-in Amplifier

Fig. 5

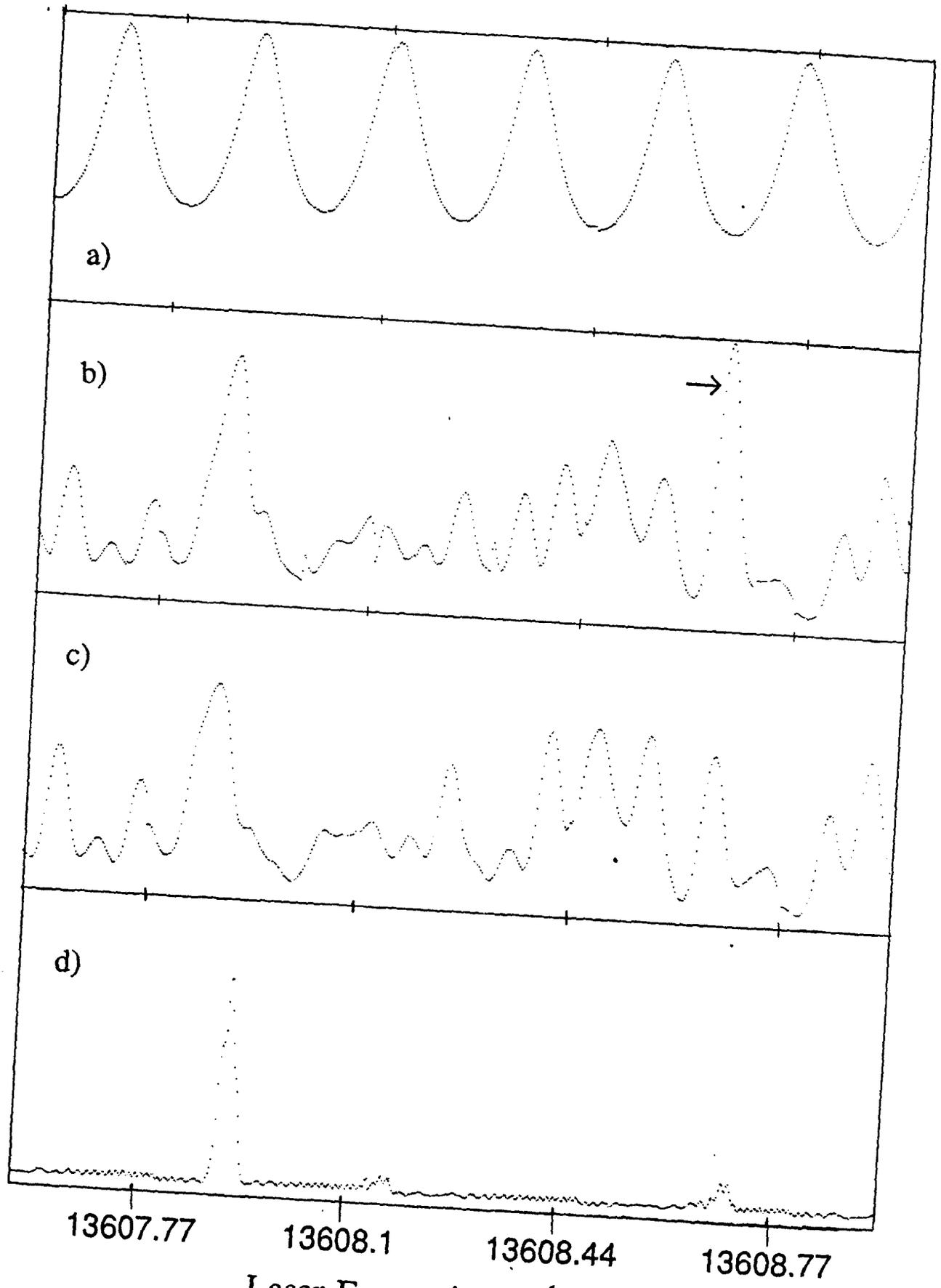

Fig. 6

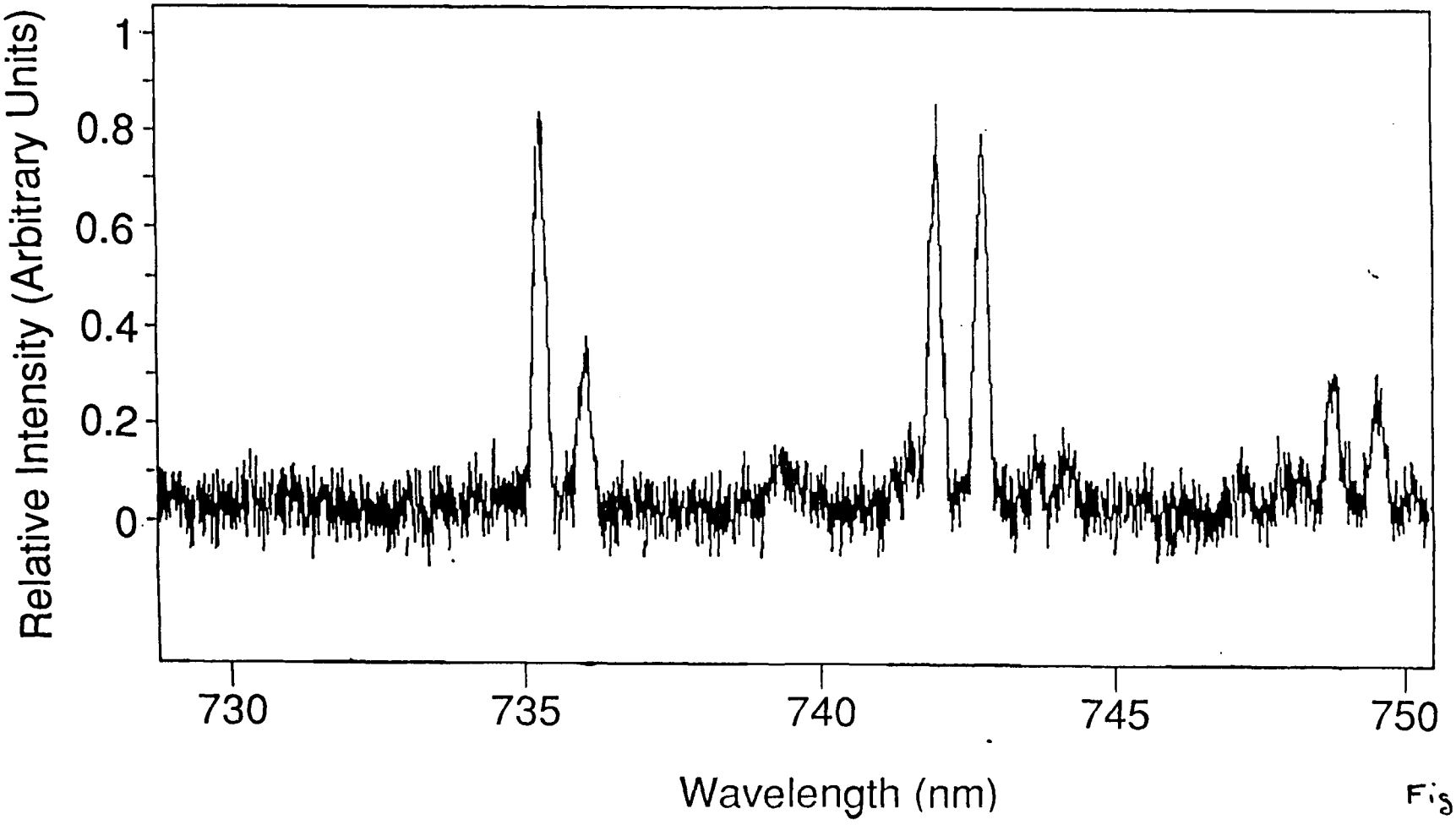
Relative Intensity (Arbitrary Units)
1
0.8
0.6
0.4
0.2
0
730
735
740
745
750
Wavelength (nm)

Fig. 7

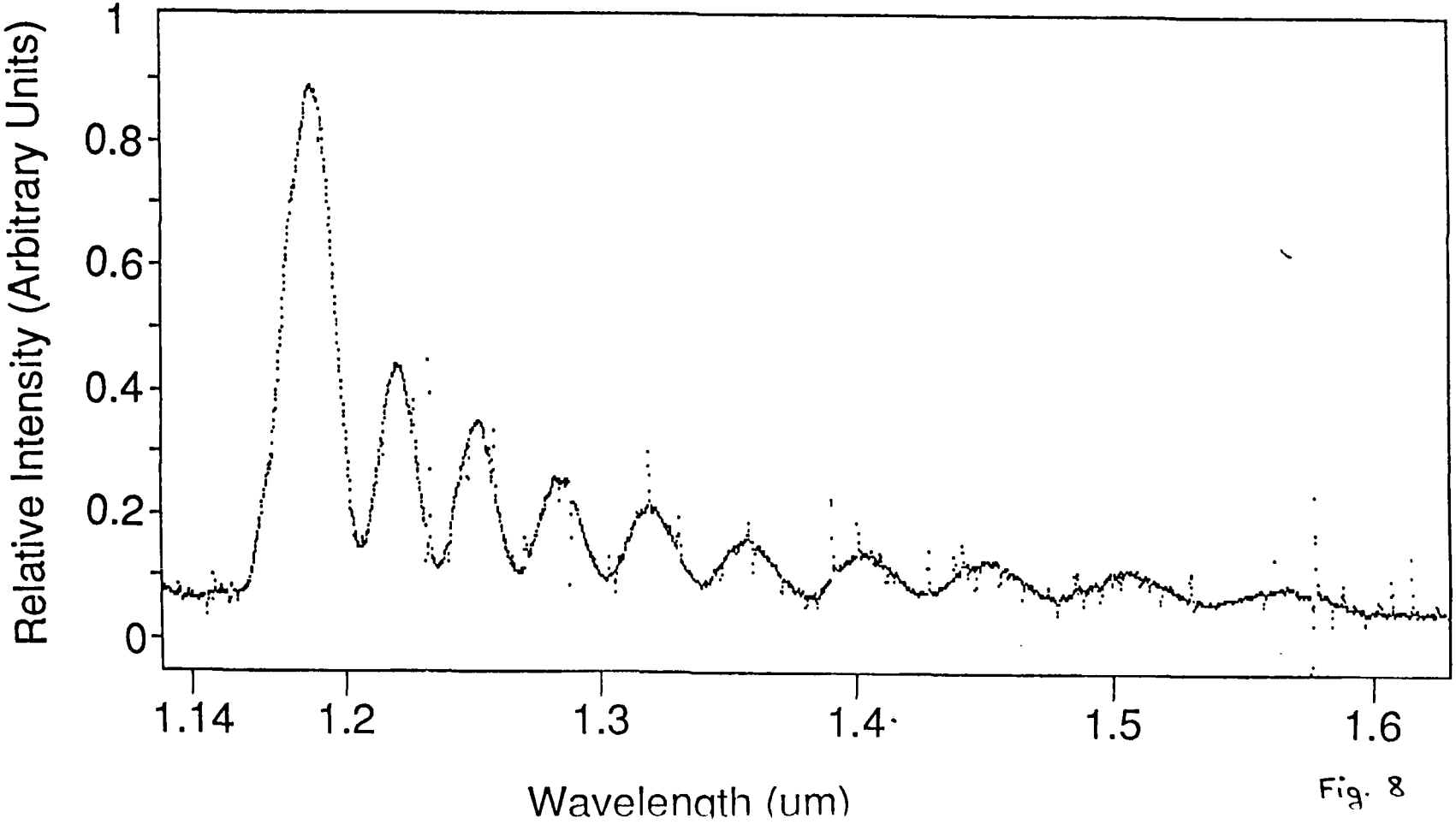
Relative Intensity (Arbitrary Units)
1
0.8
0.6
0.4
0.2
0
1.14
1.2
1.3
1.4
1.5
1.6
Wavelength (um)

Fig. 8

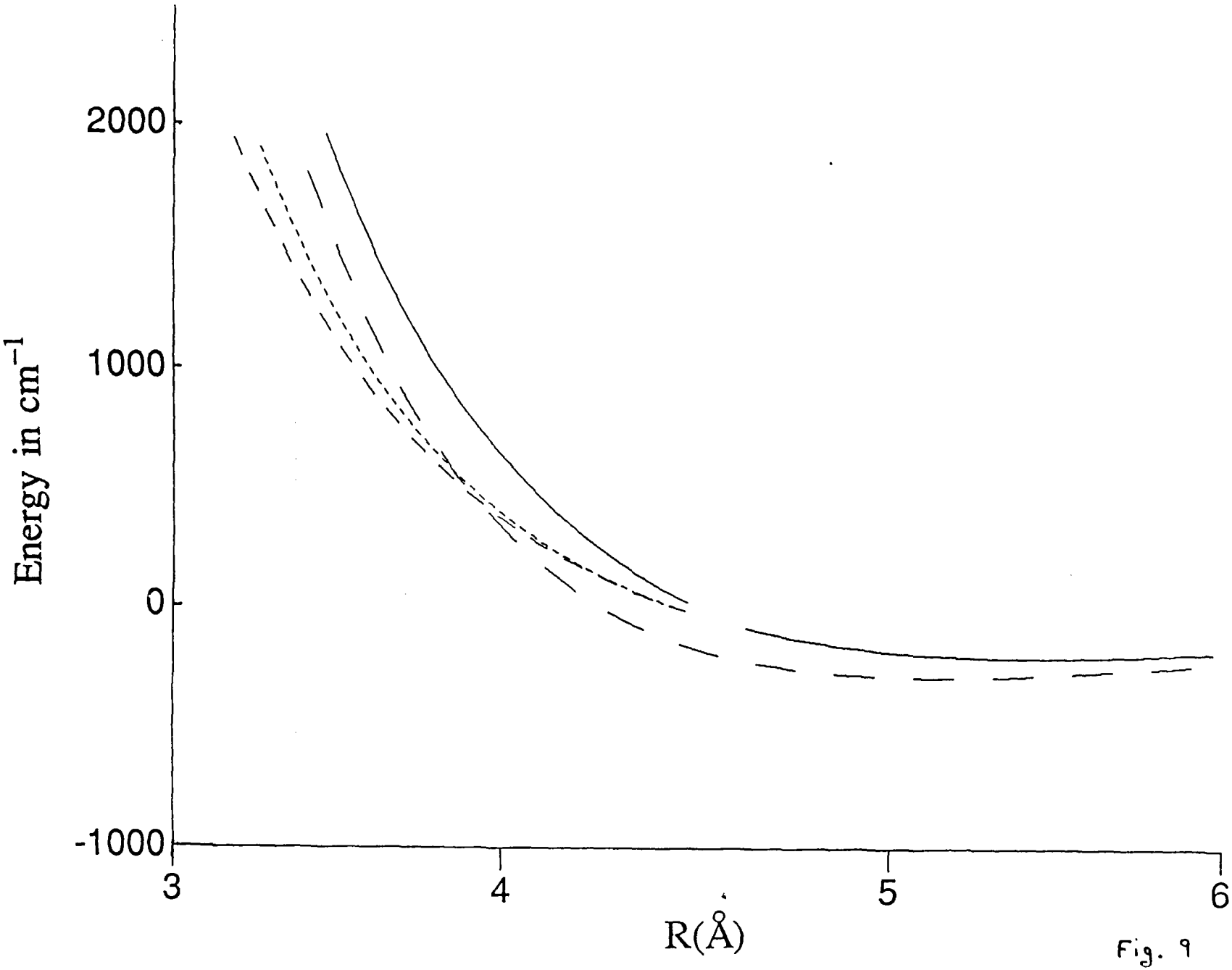

Fig. 9

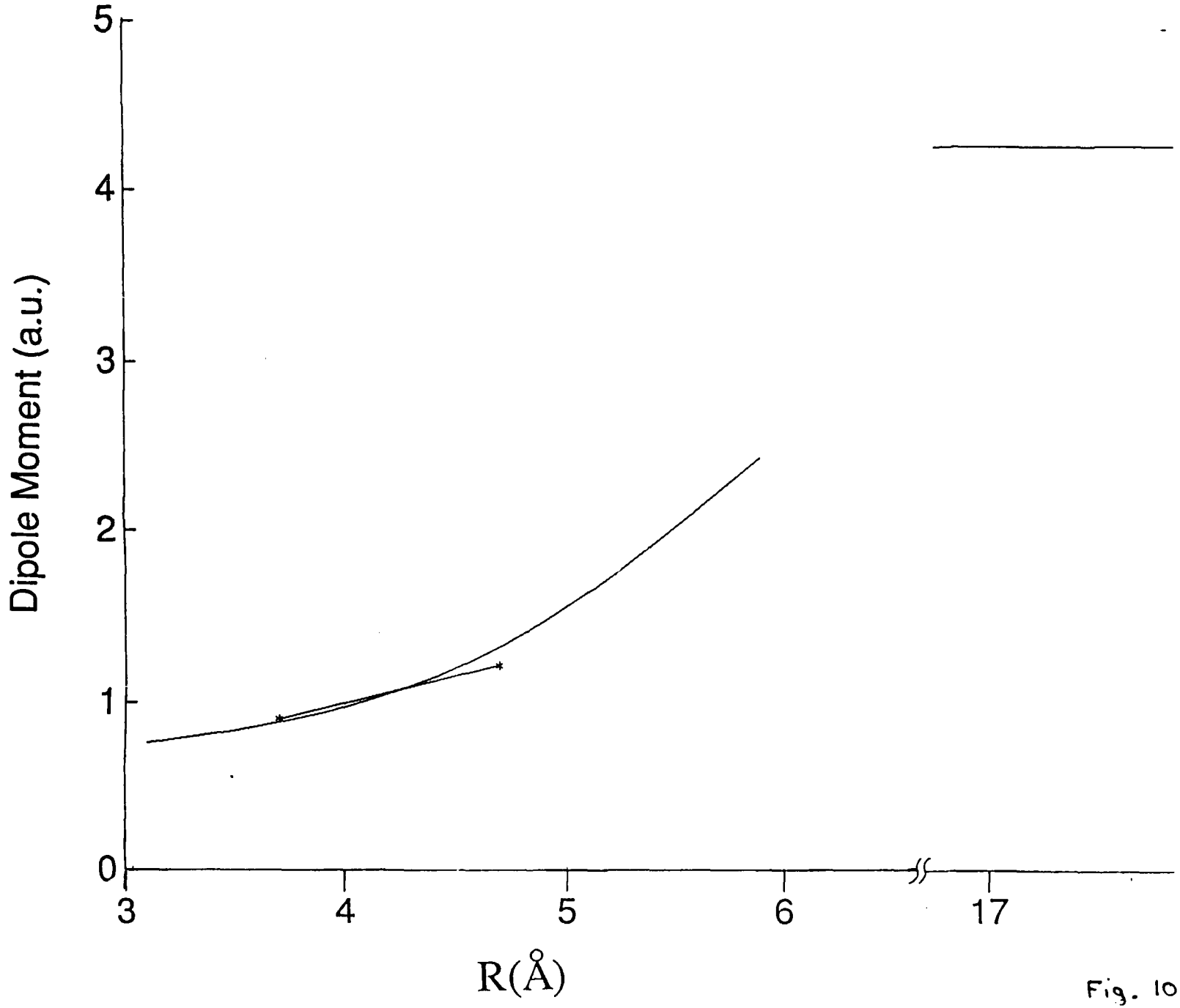

Fig. 10

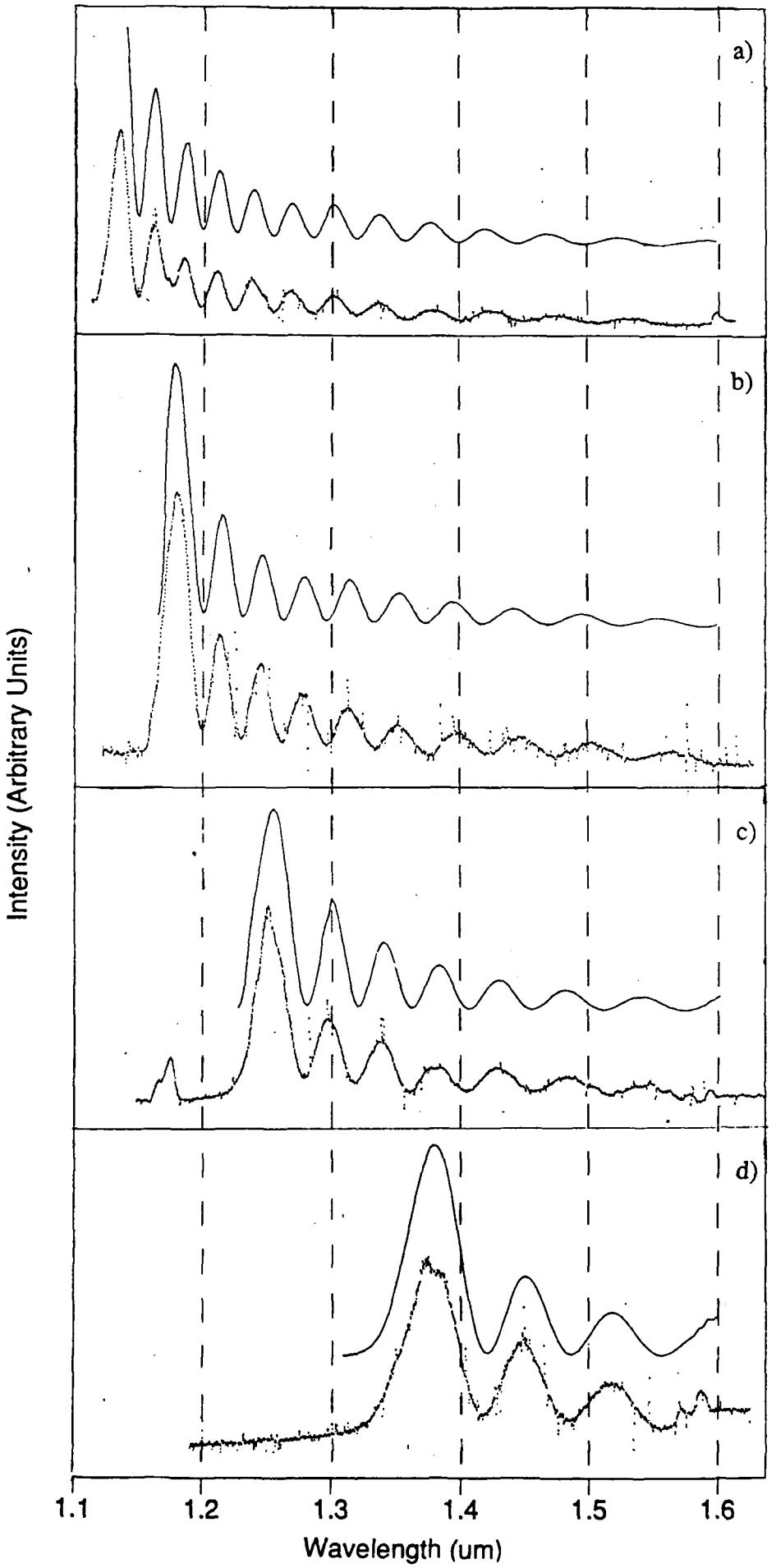
a)
b)
c)
d)
Intensity (Arbitrary Units)
1.1
1.2
1.3
1.4
1.5
1.6
Wavelength (um)

Fig. 11

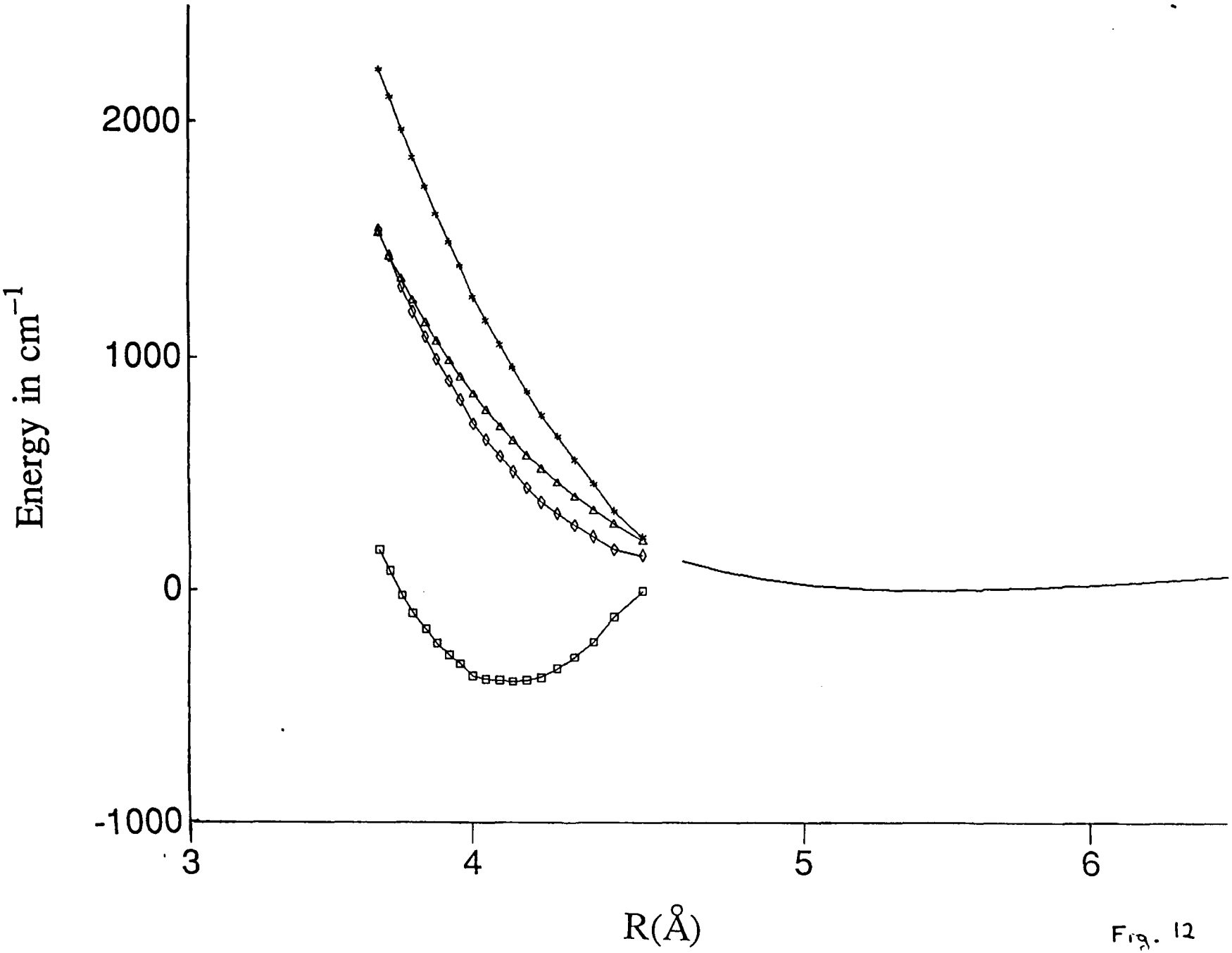

Fig. 12

Appendix 3

Advances in Laser Science - III
ed. A. C. Tam, J. L. Gole and W. C. Stwalley, American Institute of Physics - New York 1988

WAVE-MIXING PROCESSES IN SODIUM-POTASSIUM VAPOR

B. K. Clark, M. Masters and J. Huennekens, Lehigh University, Bethlehem PA 18015

ABSTRACT

We report observations of 4-wave and 6-wave mixing processes based upon two-photon pumping of the potassium 4S → 6S and 4S → 4D transitions in a sodium-potassium mixture. Additionally we observe coherent emissions at the potassium 3D → 4P transition frequencies for pump wavelengths between 725 and 760 nm. The excitation spectra for these emissions show several broad peaks, each of roughly 10 nm width. A series of sharp dips is superimposed on the most intense peak due to depletion of the 3D population by laser-induced absorption to Rydberg F levels. Although the 3D → 4P emissions can be observed in both the forward and backward directions, they are ~50 times more intense in the forward direction. We believe the forward emission is primarily due to 6-wave mixing while the backward emission can most likely be attributed to amplified spontaneous emission following two-photon molecular photodissociation. However, at present, the exact mechanisms responsible for these 3D → 4P emissions are not fully understood.

THE EXPERIMENT

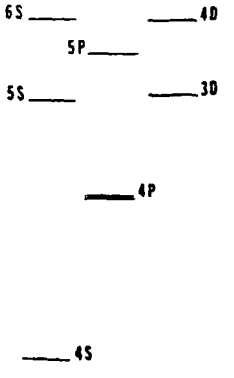

Fig. 1 - Potassium energy levels

The experiment was carried out in a crossed heat-pipe oven containing a 2:1 mixture of potassium and sodium and operated at ~435°C with an argon buffer gas pressure of ~2 Torr. The alkali vapor was excited with a Nd:YAG pumped dye laser operating in the 690 to 760 nm range with LDS 722 dye. The laser typically delivered ~10 mJ in a 10 ns pulse, and the beam was in all cases unfocussed. Forward, backward and side fluorescence was imaged onto a monochromator equipped with either a photomultiplier or an intrinsic germanium detector.

RESULTS AND DISCUSSION

With the dye laser wavelength tuned to the 4S → 6S two-photon transition at 728.4 nm we observed K_2 and NaK molecular fluorescence in the side direction along with various sodium and

potassium atomic lines. In the forward direction we observed coherent emission at the potassium 5P → 4S, 3D → 4P and 5S → 4P transition wavelengths (see Fig. 1) and at 1280 and 1370 nm which do not correspond to any atomic transitions. In the backward direction, only the 3D → 4P and 5S → 4P emissions were observed. The 5P → 4S forward emission was also observed when pumping the 4S → 4D two-photon transition. The various coherent emissions can be understood as resulting from the following processes:

4-wave mixing

$$\omega_{5P\to4S} = 2\omega_{laser} - \omega_{6S\to5P(4D\to5P)} \quad , \quad 2\omega_{laser} = \omega_{4S\to6S(4S\to4D)}$$

6-wave mixing

$$\omega_{1280(1370)} = 2\omega_{laser} - (\omega_{6S\to5P} + \omega_{5P\to3D(5P\to5S)} + \omega_{laser})$$

amplified spontaneous emission (ASE)

$$\omega_{3D\to4P(5S\to4P)} = 2\omega_{laser} - (\omega_{6S\to5P} + \omega_{5P\to3D(5P\to5S)} + \omega_{4P\to4S})$$

The ASE emissions are characterized by approximately equal intensities in the forward and backward directions, while the wave-mixing processes result only in forward emission due to phase-matching requirements. These various processes have either been observed previously in potassium vapor,[1-2] or can be understood by analogy to similar observations made in other alkalis.[3-5]

We also observe strong forward and backward emission at 1170 and 1180 nm (potassium 3D → 4P) when pumping the vapor over a broad range between 725 and 760 nm. The excitation spectrum for the 1170 nm line is shown in Fig. 2. The forward to backward ratio is approximately 55 for a pump wavelength of 752 nm and an argon pressure of 1.8 Torr. As can be seen, the excitation spectrum consists of 3 broad peaks: a very strong one centered at 752 nm, a somewhat weaker one at 741 nm, and a very weak one at 730 nm. The most intense peak has a series of sharp dips superimposed.

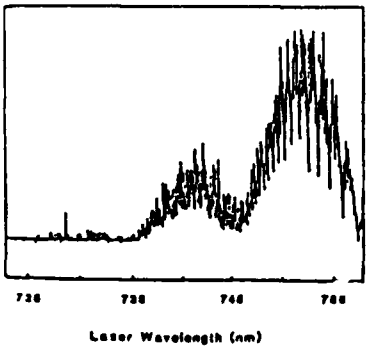

Fig. 2 – 3D → 4P excitation spectrum

Measurements of the 1170 nm forward and backward intensity as a function of argon pressure and laser power were carried out. As the pressure increased from 2 to 25 Torr, the forward signal strength

decreased by about a factor of 2 for a pump wavelength of 752 nm. Over the same range the 742 nm peak almost completely disappeared. Similar but not identical observations were made for the backward emission. Laser intensity dependences showed log-log slopes of ~.7 and 1.3 for the backward and forward 1170 nm emission, respectively. These observations support the idea that the forward and backward emission are caused by different mechanisms.

An investigation of the positions of the sharp dips in the 752 nm peak of the excitation spectrum show that they coincide with 3D → nF transitions with n ranging from 21 to 28. Thus at these pump wavelengths the laser depopulates the 3D state by inducing transitions to high-lying Rydberg states, and thereby reduces the 1170 nm emission. Similar excitation spectra for the 1180 nm line, which probe the $3D_{5/2}$ fine-structure level, show dips shifted by the expected 2 cm^{-1}.

It is worth noting that the 3D → nF dips are significantly more pronounced in the backward direction. This reflects the greater sensitivity of the 3D - 4P population inversion required for ASE compared to total 3D population responsible for forward wave mixing. We now believe the 3D → 4P backward emission can be explained as ASE probably following a two-photon molecular photodissociation process. The forward emission is most probably due primarily to 6-wave mixing involving 2 laser photons and one photon at 1170 or 1180 nm. Also involved in the process are 4P → 4S resonance photons (which are highly trapped and therefore unobservable), and two IR photons which lie beyond our detector response.

We must emphasize that these explanations are still somewhat speculative at present, and additional data is needed before final conclusions can be reached.

ACKNOWLEDGEMENTS

We thank R. N. Compton, W. R. Garrett and M. A. Moore for several helpful discussions and suggestions concerning this work. This work was supported by the Army Research Office under grant DAAL03-86-K-0161. .

REFERENCES

1. P. Agostini, P. Bensoussan and J. C. Boulassier, Op. Commun. 5 293 (1972).
2. P.-L. Zhang, Y.-C. Wang and A. L. Schawlow, J. Opt. Soc. Am. B 1 9 (1984).
3. W. Hartig, Appl. Phys. 15 427 (1978).
4. Z. G. Wang, H. Schmidt and B. Wellegehausen, Appl. Phys. B 44 41 (1987).
5. S. M. Hamadani, J. A. D. Stockdale, R. N. Compton and M. S. Pindzola, Phys. Rev. A 34 1938 (1986).

Appendix -

Appl. Phys. B 47, 159–167 (1988)

Applied Physics B Photophysics and Laser Chemistry

Wave Mixing and Amplified Spontaneous Emission in Pure Potassium and Mixed Sodium-Potassium Vapors

B. K. Clark, M. Masters, and J. Huennekens

Department of Physics, Lehigh University, Bethlehem, PA 18015, USA

Received 6 April 1988/Accepted 16 May 1988

Abstract. We report observations of several wave-mixing and stimulated processes in pure potassium and mixed sodium-potassium vapors which are excited by a pulsed laser operating in the range 680–800 nm. When the laser is tuned to the potassium two-photon $4S \rightarrow 6S$ transition, we observe stimulated emission on the various cascade transitions as well as four- and six-wave mixing. When the laser is tuned over the range 747 to 753 nm, which is well away from all atomic transitions, we observe strong forward and weak backward emission at the potassium $3D_{3/2} \rightarrow 4P_{1/2}$ transition wavelength (1.17 μm). However, this latter emission is only observed in the mixed sodium-potassium vapor. We present data on the excitation spectrum, forward to backward asymmetry, temporal dependence, and the laser power dependence of this emission. We speculate that two-photon photodissociation of the NaK molecule is responsible for this emission.

PACS: 42.65.Cq

The last few years have seen a rapid growth in the number of studies involving non-linear optical processes in alkali vapors. Included in this are studies of purely atomic processes such as parametric four- and six-wave mixing, amplified spontaneous emission, optically pumped stimulated emission, and stimulated Raman and hyper-Raman scattering [1–18]. Additional coherent processes involving collisional energy transfer or photodissociation of alkali molecules have also been observed [19–25].

In the present work, we present experimental observations of various non-linear processes occurring in pure potassium or mixed sodium-potassium vapors excited by a high-power, pulsed laser operating in the range 680 to 800 nm. In particular, when the laser is tuned to either the potassium $4S \rightarrow 6S$ or $4S \rightarrow 4D$ two-photon transition, we observe amplified spontaneous emission on the cascade atomic lines, as well as several four- and six-wave mixing processes. Figure 1 presents partial energy level diagrams of potassium showing in schematic form some of the processes observed. The ~404 nm four-wave mixing signals, which are nearly resonant with the potassium $5P \rightarrow 4S$ transitions, were to the best of our knowledge first observed by Lumpkin [1] and Barak et al. [2]. In those experiments an off-resonant, two-step excitation scheme was used, and the $5P$ levels populated by a stimulated Raman process. Agostini et al. [3] observed similar four-wave mixing near 404 nm when pumping potassium vapor with a dye laser tuned to the two-photon $4S \rightarrow 4D$ transitions. Analogous processes have since been observed in sodium [4, 5], rubidium [6], and cesium [7]. Processes such as the optically pumped stimulated emission ($6S \rightarrow 5P$) and cascade amplified spontaneous emissions ($5P \rightarrow 5S$, $5P \rightarrow 3D$, $5S \rightarrow 4P$, and $3D \rightarrow 4P$) are created by population inversions which occur as the atoms cascade down through their various energy levels. Analogous processes have been observed in all of the alkalis under a wide variety of excitation conditions [4, 9–18]. Finally, when pumping the potassium $4S \rightarrow 6S$ transition we observe coherent forward emissions at 1.28 and 1.37 μm. By comparison

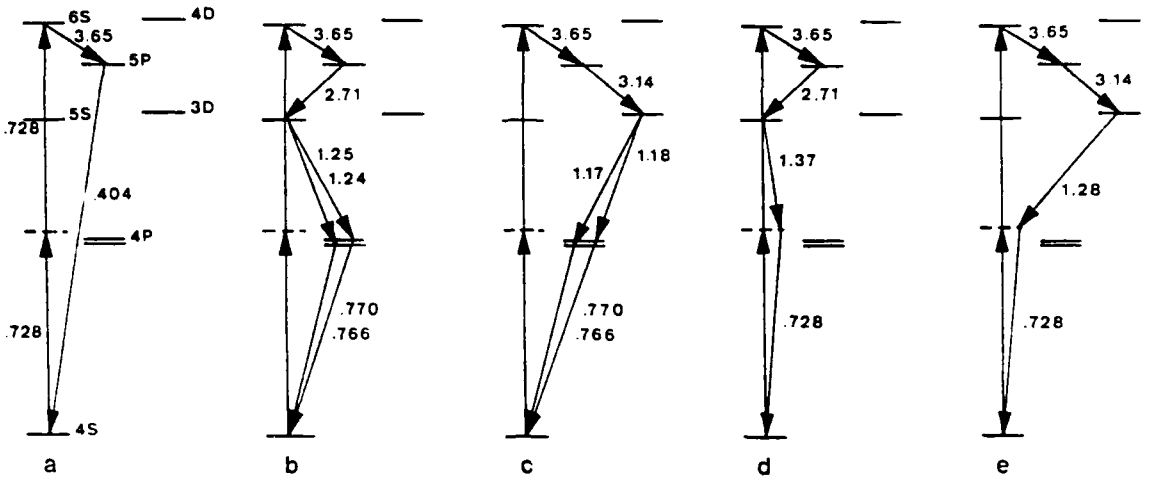

Fig. 1. Partial energy level diagrams of potassium showing the processes observed when the laser is tuned to the potassium $4S \rightarrow 6S$ two-photon transition. (a) Four-wave mixing near the $5P \rightarrow 4S$ transition wavelength. (b, c) Amplified spontaneous emission on the cascade transitions. (d, e) Six-wave mixing processes

with analogous processes in Na vapor [18], we can identify these as six-wave mixing processes. Our data on these various processes are presented in Sect. 2.

While observations of these types of atomic stimulated and wave-mixing processes are now becoming fairly commonplace, more complicated processes involving the diatomic molecules in the vapor are less well understood. In particular, several observations of atomic stimulated emissions have been made when alkali transitions coupling two excited states have been pumped with high power lasers [19–23]. The lower state of the transition (typically the sodium $3P$ or the potassium $4P$ state) is in each case excited by either one photon dissociation of the diatomic molecule or by collisional excitation transfer from the molecule. Another source of stimulated emissions on atomic transitions is due to two-photon photodissociation of molecules into one ground state and one excited state atom. Population inversions can then exist between the excited level and lower unpopulated states. Such a "photodissociation laser" was observed in mercury vapor in 1977 by Komine and Byer [26]. Similar processes were observed more recently in sodium [5, 22] and potassium [19, 21]. The work of Wang and coworkers [19, 21] is of particular interest in connection with our present findings. Finally, there have been recent reports of stimulated emissions on diffuse molecular bands following excitation of atomic transitions [24, 25].

In this paper we also report observations of an interesting process where strong forward emission at the potassium $3D \rightarrow 4P$ transition wavelength is detected when sodium-potassium mixtures are pumped over a broad wavelength range near 750 nm. Since this process cannot be observed in pure potassium vapor, we suspect that either Na_2 or NaK molecules are involved. Since Na_2 absorbs only weakly in this wavelength region, we believe we are observing two-photon photodissociation of NaK. Using the known well depth of the NaK ground state, [27] we find that we have just sufficient energy to reach the $Na(3S) + K(3D)$ dissociation limit from the $v = 1$ level of the ground state well. However, the $3D \rightarrow 4P$ emission appears primarily in the forward direction which may indicate that either a parametric wave mixing process is involved, or that the gain is asymmetric. The excitation spectrum for this $3D \rightarrow 4P$ emission shows a broad hump centered near 750 nm which is similar to the broad hump centered on 640 nm observed by Wang et al. [19] in the excitation spectrum for potassium $5P \rightarrow 5S$ and $5P \rightarrow 3D$ emission. In the present case, the 750 nm hump has a series of sharp dips superimposed on it. We found that these dips are the result of depletion of the potassium $3D$ state population by laser-induced transitions to Rydberg F levels. Details concerning these observations are presented in Sect. 2.

1. The Experiment

The experimental apparatus is shown in Fig. 2. A vapor containing a mixture of sodium and potassium was contained in a 4-way cross, stainless-steel, heat-pipe oven. The initial mixture of potassium and sodium was ~2 to 1 although temperature cycling and subsequent reloadings caused the ratio of potassium to sodium

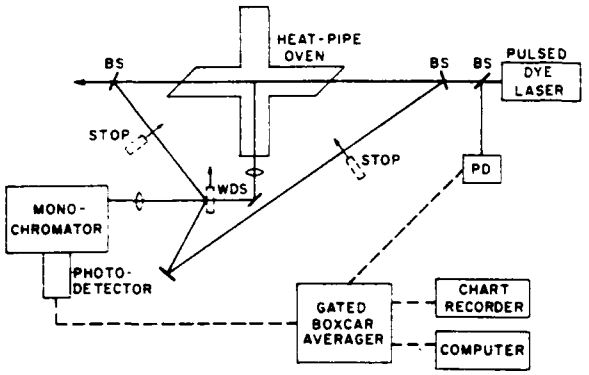

Fig. 2. Experimental set-up. In the figure, PD, BS, and WDS represent photodiode, beam splitter and white diffusing surface, respectively. The white diffuser can be translated out of the way so that side fluorescence can be imaged onto the monochromator slits

atoms in the vapor phase to vary with time. The oven pressure (determined by the argon buffer gas pressure) was varied over the range 1.3 to 9 Torr, while the temperature range studied extended from 385 to 440 °C. To verify the molecular species involved in the non-resonant process, an oven containing pure potassium was occasionally substituted for the Na–K oven without adjusting any of the associated optics.

The vapor was excited by a pulsed, frequency-doubled Nd:YAG laser pumped dye laser. The dye LDS 765 was used in the range 740 to 810 nm, while LDS 722 was used to cover the range 680 to 760 nm. Peak laser powers of ~1 MW at 750 nm were typical. In most cases the laser beam entering the oven was unfocused.

Fluorescence emitted perpendicular to the pump laser axis was monitored through a cross-arm of the heat-pipe oven. The light was resolved using a 0.22 meter monochromator in conjunction with a liquid nitrogen cooled intrinsic germanium detector. Long-pass, color-glass filters were used to eliminate signals due to second order scattering from the diffraction grating. Light emitted approximately parallel (which we will call forward emission) or antiparallel (backward) to the pump laser beam could be directed to the same monochromator by a set of partially reflecting and highly reflecting mirrors. In these cases the intense emissions were scattered off a white diffusing surface in front of the monochromator. The white diffuser was positioned on a translating mount so that forward, backward and side scans could be taken without changing the optical alignment. Note that since collimating optics were not used in the forward and backward directions, only coherent emissions could be observed in those directions. For observations in the forward direction, the laser beam was always blocked with an appropriate color-glass filter before the white diffuser. Calibration of the forward to backward detection efficiency was obtained by first observing the unblocked laser beam in the forward direction (with the oven cold), and then retroreflecting the beam and observing in the backward direction. In this manner it was found that the forward to backward detection efficiency was ~1.

Several types of measurements were performed. For the first type of measurement, the monochromator was set to pass either the potassium $3D_{3/2} \rightarrow 4P_{1/2}$ emission at 1.17 μm or the $3D_{5/2} \rightarrow 4P_{3/2}$ emission at 1.18 μm. The dye laser was then tuned through part of the dye profile and the resulting atomic emission monitored in the forward, backward, or side directions. These we call excitation scans. Measurements of this type were carried out for a range of pressures and temperatures.

In the second type of measurement, the dye laser was set to a particular wavelength and the monochromator scanned, usually from 800 to 1700 nm. These we call emission scans. Since an intrinsic germanium detector was used most of the time, sensitivity was poor below 800 nm although strong emission near 404 nm corresponding to $5P \rightarrow 4S$ could be weakly detected.

In some cases the germanium detector was replaced with a photomultiplier tube (S-1 cathode) or an indium-antiminide detector, so that observations could be made at shorter or longer wavelengths, respectively. Using the three detectors, the entire spectral range between 0.4 and 4 μm could be monitored. Additionally, since the photomultiplier has an ~1 ns time response and a small, but adequate, sensitivity at 1.17 μm, it could be used to study time-dependences of the $3D \rightarrow 4P$ emissions. The angular divergence of the potassium $3D \rightarrow 4P$ forward emission was studied using an iris diaphragm.

Finally, the power dependences of the $3D \rightarrow 4P$ and other emissions were determined using a series of neutral density filters placed between the dye laser and the heat-pipe oven. The filters were calibrated in place using the photodiode shown in Fig. 2.

2. Results and Discussion

Figure 3 shows the near-infrared forward and backward emission scans when the laser wavelength in air was set to 728.36 nm, which corresponds to the potassium $4S \rightarrow 6S$ two-photon transition. Here it can be seen that the atomic $3D_{3/2} \rightarrow 4P_{1/2}$ (1.17 μm), $3D_{5/2} \rightarrow 4P_{3/2}$ (1.18 μm), $5S_{1/2} \rightarrow 4P_{1/2}$ (1.24 μm), and $5S_{1/2} \rightarrow 4P_{3/2}$ (1.25 μm) emissions are all seen in both the forward and backward directions. (In all cases the

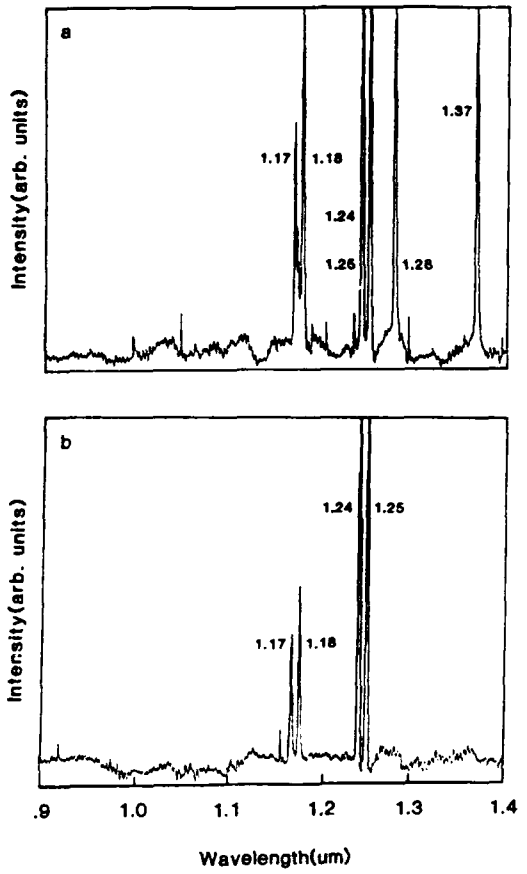

Fig. 3. (a) Forward and (b) backward near-infrared emission scans obtained when the laser was tuned to the potassium $4S \rightarrow 6S$ two-photon transition in the mixed sodium-potassium vapor. The 1.28 and 1.37 μm emissions in the forward direction correspond to six-wave mixing processes while the 1.17/1.18 and 1.24/1.25 μm doublets correspond to potassium $3D \rightarrow 4P$ and $5S \rightarrow 4P$ transitions, respectively

forward to backward intensity ratios are in the range between 1 and 2.) These lines clearly represent amplified spontaneous emission (ASE) resulting from population inversions that exist as the atoms cascade down through their energy levels in allowed transitions.

The two lines at 1.28 and 1.37 μm are only observed in the forward direction. These emissions, which have also been observed at Oak Ridge [28] are analogous to emissions at 795 and 840 nm observed in sodium vapor pumped at the two-photon $3S \rightarrow 5S$ and $3S \rightarrow 4D$ transitions, respectively [18]. From the explanation of [18] and the diagrams in Fig. 1d and e, it can be shown that these lines represent six-wave mixing processes involving three photons at the laser wavelength and two near-infrared photons produced in the vapor by stimulated hyper-Raman scattering and ASE. Due to phase-matching conditions, these emissions are only in the forward direction. A side emission scan verified that although the various atomic lines and molecular emission could be clearly seen, the 1.28 and 1.37 μm emissions were absent as expected.

A photomultiplier tube was used in place of the germanium detector so the emission scans could be made down to 400 nm. Near 404 nm, very strong forward emission was observed. No emission near this wavelength could be detected in the backward direction. This emission, which has been studied extensively in the past [1–3, 28], represents a parametric four-wave mixing process.

These various processes observed when pumping the two-photon transition at 728.36 nm can be summarized by the following set of equations:

4-wave mixing

$$\omega_{5P \rightarrow 4S} = 2\omega_{\text{laser}} - \omega_{6S \rightarrow 5P(4D \rightarrow 5P)}, \quad 2\omega_{\text{laser}} = \omega_{4S \rightarrow 6S(4S \rightarrow 4D)}$$

6-wave mixing

$$\omega_{1.28(1.37)} = 2\omega_{\text{laser}} - (\omega_{6S \rightarrow 5P} + \omega_{5P \rightarrow 3D(5P \rightarrow 5S)} + \omega_{\text{laser}})$$

amplified spontaneous emission

$$\omega_{3D \rightarrow 4P(5S \rightarrow 4P)} = 2\omega_{\text{laser}} - (\omega_{6S \rightarrow 5P} + \omega_{5P \rightarrow 3D(5P \rightarrow 5S)} + \omega_{4P \rightarrow 4S}).$$

Measurements of the angular divergences of these emissions for the laser tuned to 728.36 nm were not carried out in the present experiment. However, Wang et al. [18] found that the analogous emissions in sodium display roughly the same angular divergence as the pump laser beam. We note also that apart from effects due to pressure and temperature differences in the two ovens, results obtained with the pure potassium and the sodium-potassium mixtures were essentially identical when pumping at 728.36 nm.

When we replaced the germanium detector with the indium-antimonide detector, several other coherent emissions could be observed. These include infrared emissions at 3.65, 3.14, and 2.71 μm which correspond to the $6S \rightarrow 5P$, $5P \rightarrow 3D$, and $5P \rightarrow 5S$ transitions, respectively. The $6S \rightarrow 5P$ emission appeared in both the forward and backward directions with an intensity ratio of 3:8, while the $5P \rightarrow 3D$ and $5P \rightarrow 5S$ emissions, which compete with the $5P \rightarrow 4S$ emission at 404 nm, were observed with a forward to backward intensity ratio of $\sim 10:1$.

Raising the pressure in the heat-pipe oven we observed a change in the 1.17 and 1.18 μm emission when pumping at 728.36 nm. At low temperatures and pressures, these emissions appeared at 1.169 and 1.177 μm and were observed with approximately equal intensities in the forward and backward directions. At

higher temperatures and pressures a third emission at 1.172 μm, which was only observed in the forward direction, began to build in. As the temperature and pressure were raised still further, the 1.172 μm emission was the only one of the three that could be observed. This observation represents a competition between amplified spontaneous emission and a parametric six-wave mixing process. This competition is strongly influenced by phase-matching conditions involving the anomalous dispersion near the transition frequency. This in turn is influenced by the temperature, pressure and composition of the vapor. For example, under our conditions the 1.169 and 1.177 μm lines were difficult to produce clearly in the pure potassium heat-pipe but easily observable in the mixed vapor oven.

In the course of investigating the various coherent emissions described above, we also recorded several laser excitation spectra. We found that when the laser was tuned away from the two-photon $4S \rightarrow 6S$ and $4S \rightarrow 4D$ transitions we could still observe strong forward and weak backward emission on the potassium $3D_{3/2} \rightarrow 4P_{1/2}$ transition at 1.17 μm, and under certain conditions we could also see weak emission at 1.18 μm corresponding to the $3D_{5/2} \rightarrow 4P_{3/2}$ transition. These emissions could only be observed in the heat-pipe oven containing the sodium-potassium mixture. No forward emission could be observed in the pure potassium oven when the laser was tuned away from the atomic transitions despite extensive searches over our range of pressures, temperatures and laser wavelengths.

Figure 4 shows several excitation spectra for the $3D_{3/2} \rightarrow 4P_{1/2}$ forward emission taken in the Na–K oven at various pressures. In this case the dye LDS 765 was used. Excitation spectra obtained with the dye LDS 722 over the same wavelength range were quite different and will be discussed below. It can be seen from Fig. 4 that the 1.17 μm emission can be produced over a broad range of pump wavelengths between 747 and 753 nm. Although each excitation spectrum appears to be a set of spikes, it really consists of a broad hump with a series of sharp dips superimposed. The dips can be easily identified as occurring at wavelengths corresponding to $3D_{3/2} \rightarrow nF_{5/2}$ transitions. Here n is the range 26 through 29. Under conditions where forward emission at 1.18 μm can be observed, the excitation spectra reveal a series of sharp dips corresponding to $3D_{5/2} \rightarrow nF_{7/2}$ transitions. In each case it is clear that the emission intensity is being reduced by the coincidental pumping of the upper state of the forward emission to a high-lying Rydberg F level.

Under the same conditions as those that produced Fig. 4, weak backward emission at 1.17 μm could also be observed. The ratio of forward to backward emission at 1.17 μm was on the order of 25 : 1.

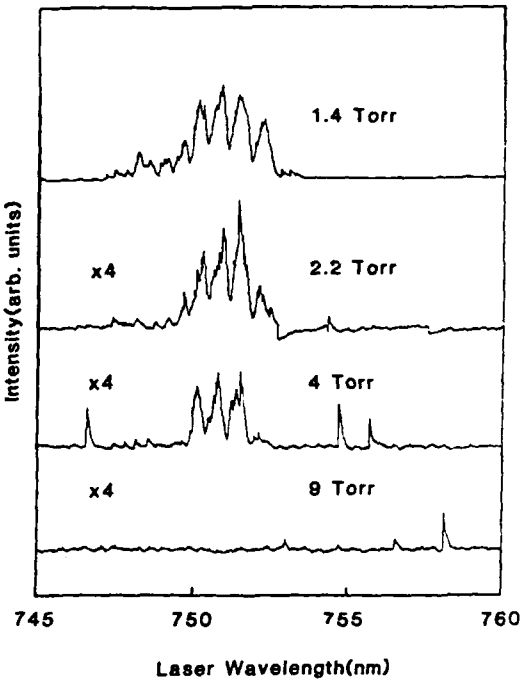

Fig. 4. 1.17 μm (potassium $3D_{3/2} \rightarrow 4P_{3/2}$) excitation spectra obtained at several pressures in the mixed sodium-potassium vapor. The extraneous spikes at ~747, 755, and 756 nm in the 4 Torr scan, and at ~758 nm in the 9 Torr scan are not reproducible and are due to cosmic rays to which the germanium detector is sensitive

Figure 5 shows emission scans in the forward and side directions for laser excitation at 751.6 nm. It can be seen that the forward 1.17 μm emission is stimulated since spontaneous emission (as observed in the side direction) produces more light at 1.18 than at 1.17 μm. The spontaneous emission spectrum also shows K_2 and NaK molecular emission near 1 μm and potassium $5S \rightarrow 4P$ emission at 1.24 and 1.25 μm.

Time dependence measurements shown in Fig. 6 reveal that the forward 1.17 μm light is produced during the laser pulse duration of ~8 ns, while the side direction spontaneous emission is recorded over a period greater than 100 ns, which is characteristic of the $3D$ state lifetime (~40 ns) lengthened by radiation trapping. Using the three available detectors, we conducted a search for other forward emissions in the wavelength range 0.4 to 4 μm, but no other emissions were observed.

Figures 4 and 7 show the effects of pressure and temperature on the 1.17 μm forward emission. As can be seen, increasing temperature enhances the emission, while increasing pressure quenches the process.

Figure 8 shows the dependence of the 1.17 μm emission on laser power. Clearly the emission displays a

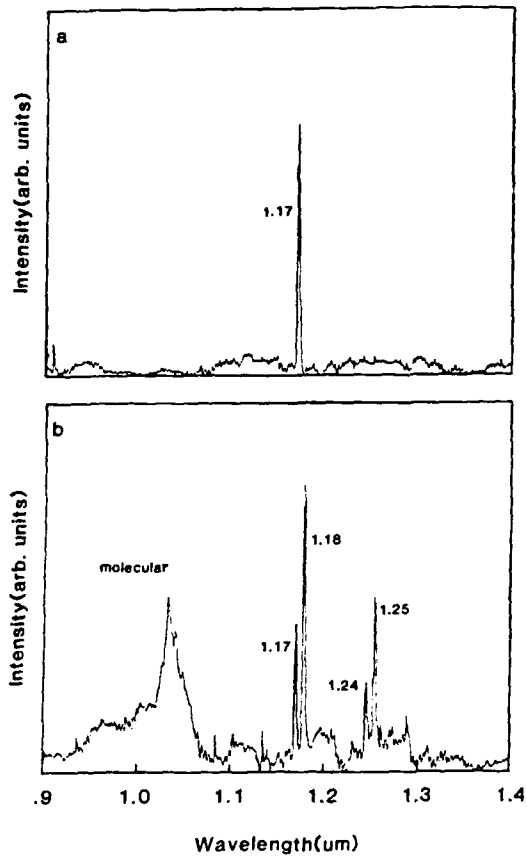

Fig. 5. (a) Forward and (b) side near-infrared emission scans obtained when the laser was tuned to 751.6 nm in the mixed sodium-potassium vapor. The molecular emission observed in the side direction between 0.95 and 1.05 μm is due to NaK and K_2 $A^1\Sigma \rightarrow X^1\Sigma$ transitions

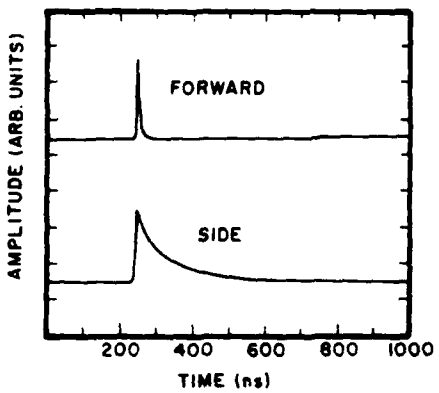

Fig. 6. Time dependence of the forward and side emission at 1.17 μm. The forward emission has a full width half maximum of ~8 ns which corresponds to the laser pulse duration. The side emission persists for more than 100 ns which represents the 3D state natural lifetime of ~40 ns lengthened somewhat by radiation trapping

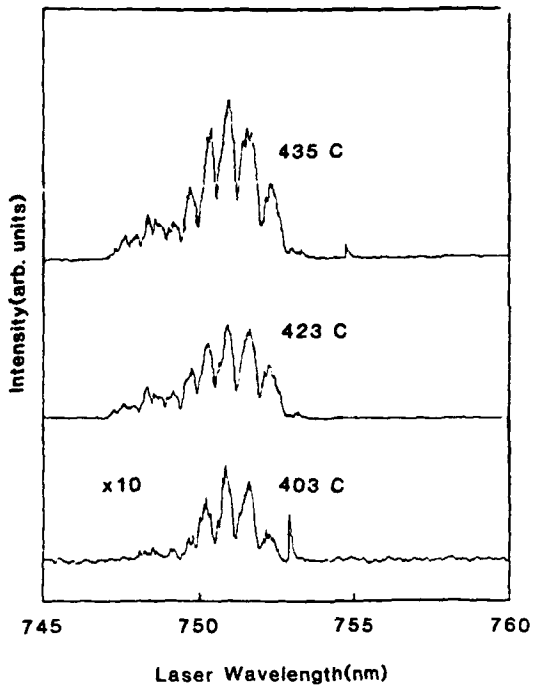

Fig. 7. Temperature dependence of the 1.17 μm (potassium $3D_{3/2} \rightarrow 4P_{1/2}$) forward emission observed when the mixed sodium-potassium vapor is excited over the range 745 to 760 nm. The pronounced dips in the emission hump correspond to depletion of the $3D_{3/2}$ level by laser excitation to Rydberg $nF_{5/2}$ levels (with n in the range 26 to 30)

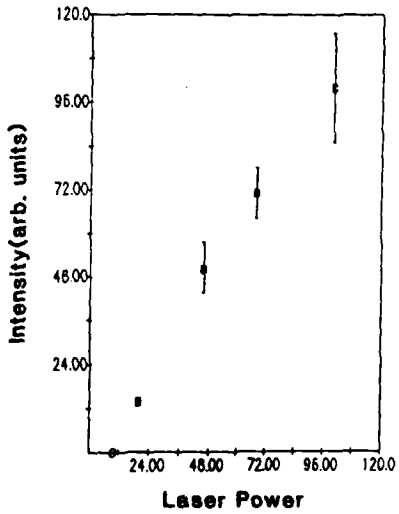

Fig. 8. Laser power dependence of the 1.17 μm emission when the mixed vapor is excited at 751.6 nm. Laser power of 100 corresponds to full laser power (approximately 1 MW) in an unfocused beam of ~0.1 cm diameter

threshold behavior. Above threshold the emission follows a linear response with some indication of saturation at high intensities. Finally, the angular divergence of the 1.17 μm emission produced with LDS 765 dye pumping of the NaK vapor at 751.6 nm was studied using an iris diaphragm. These studies showed that the 1.17 μm emission has a somewhat larger angular divergence than the pump laser beam.

We interpret these results as indicating that two-photon excitation of the NaK molecule populates a state that can either directly dissociate or predissociate to produce excited potassium atoms in the $3D_{3/2}$ state; i.e.

$$\mathrm{NaK}(X^1\Sigma)+2h\nu\rightarrow\mathrm{NaK}(?)\rightarrow\mathrm{K}(3D_{3/2})+\mathrm{Na}(3S).$$

We identify the important molecular species as NaK by a process of elimination. K_2 can be ruled out by the absence of the emission in pure potassium vapor and Na_2 is an unlikely candidate since it is a poor absorber near 750 nm and a collisional step would also be required to populate K(3D) in that case. The requirement of sodium in the oven makes it difficult to imagine that the process could be strictly atomic, although some hybrid sodium-potassium collisional mechanism might be invoked. However, the molecular dissociation mechanism is further supported by the absence of other stimulated infrared emissions. Two laser photons would carry the potassium atom to well above the 5P level, which could be populated by stimulated hyper-Raman scattering or by collision from some excited state of sodium. However, any such mechanism would be likely to produce stimulated emission on either the $5P\rightarrow3D$ or $5P\rightarrow5S$ transitions. Such emissions were observed by Sorokin and Lankard [8] pumping at 694.3 nm, and also by Wang et al. [19] who used las excitation over the range 600 to 700 nm. Because of the binding energy of the NaK ground state, it is not possible to reach 5P through photodissociation of the molecular states. However, the K(3D) + Na(3S) dissociation limit can just be reached from low lying rovibrational levels of the NaK ground state with two laser photons. Collisional excitation transfer from molecules to atoms (i.e. $\mathrm{NaK}^*+\mathrm{K}\rightarrow\mathrm{NaK}+\mathrm{K}^*$ where NaK^* and K^* represent an excited molecule or atom, respectively) cannot be entirely ruled out. However, collisions would be expected to occur over a time much longer than the laser pulse, and would be expected to populate other levels such as 5P, 5S, and $3D_{5/2}$ just as strongly as $3D_{3/2}$. Photodissociation, on the other hand, can be a very selective process. In cesium, for example, the $5D_{3/2}$ state is found to be populated more than twice as efficiently as $5D_{5/2}$ when Cs_2 is photodissociated over the pumping range 460–520 nm, [29] and the $6P_{3/2}$ state is 200 times more strongly populated than $6P_{1/2}$ over the range 560–620 nm [30].

Both the forward to backward intensity ratio and the larger angular divergence of the 1.17 μm emission compared to the pump beam argue that the observed process involves some type of wave-mixing. However, it is hard to reconcile the wave-mixing idea with a photodissociation process. Photodissociation converts some excitation energy into kinetic energy so it is difficult to imagine how the photon energies could add up as required in wave-mixing. In addition our studies indicate that no other nearly collinear photons are emitted in the range 0.4 to 4 μm. It is impossible to devise a four- or six-wave mixing process involving two laser photons and one photon at 1.17 μm that does not also produce at least one other photon in this 0.4 to 4 μm range. Nevertheless, it is possible to imagine that a population inversion between $3D_{3/2}$ and $4P_{1/2}$ could be produced by photodissociation, and the subsequent amplified spontaneous emission could trigger a wave mixing process involving two laser photons, one 1.17 μm photon, one $4P_{1/2}\rightarrow4S$ photon at 769.9 nm (which is highly trapped in the optically thick vapor and therefore cannot be observed), and several IR photons beyond 4 μm. This would explain the small emission in the backward direction as a residual of the ASE, while most of the forward emission would result from the wave-mixing process. An alternate explanation is that we are observing a simple photodissociation produced lasing which has a strong forward to backward gain asymmetry. This type of gain anisotropy is observed in alkali dimer lasers, for example [31, 32]. However, it should be emphasized that at this point all such discussion is primarily speculation, and remains to be fully tested.

It was mentioned above that pumping the sodium-potassium vapor using the dye LDS 722 produced a very different excitation spectrum at 1.17 μm than that obtained with the dye LDS 765 over the same wavelength range. The LDS 722 excitation spectrum is shown in Fig. 9. Not only is the intensity of the 750 nm hump approximately 12 times larger than the corresponding LDS 765 peak (even though we had less power at 750 nm using LDS 722), but also a weaker hump centered about 741 nm and a very weak hump near 730 nm can now also be seen. Because of this surprising discrepancy, we carried out detailed measurements of the spectral composition of the laser pulse for each of the two dyes. When the laser wavelength was set to 751.6 nm, the LDS 722 dye is working near the edge of its gain profile. Under such conditions background ASE from the dye is expected to be relatively strong. We found that in addition to the main laser peak, the LDS 722 produced a 15 nm wide lobe located 30 nm to the blue of the main peak which

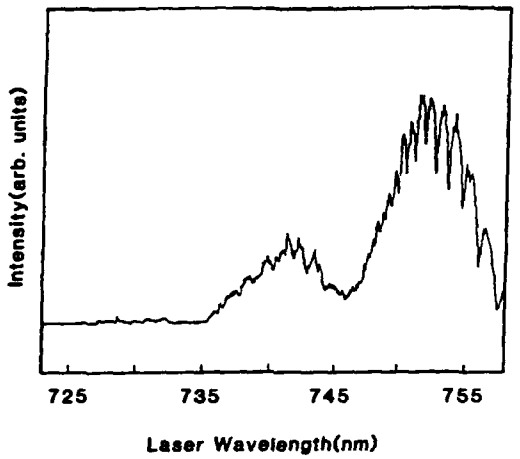

Fig. 9. 1.17 μm forward excitation spectrum obtained in the mixed vapor using unfiltered LDS 722 dye laser pumping. In this case the dye laser emission is contaminated by an ASE lobe located at ~720 nm and containing approximately 0.5% of the total laser intensity. Although the intensity scales in this figure and Figs. 4 and 7 are arbitrary, our measurements indicate that the peak intensity is roughly a factor of 12 greater when the ASE lobe is present. Additionally, a second hump in the excitation spectrum can now be seen centered on 741 nm and a third very weak hump can just barely be seen near 730 nm. The dips on the main hump correspond to depletion of the $3D_{3/2}$ level by pumping to $nF_{5/2}$ levels with n in the range 21 to 32

contained approximately 0.5% of the total intensity. A similar, but 20 times smaller, lobe was observed approximately 25 nm to the long wavelength side of the main peak. When we used the dye LDS 765, the short wavelength lobe was not observed although the long wavelength lobe was still present.

It was clear that the short wavelength lobe had a profound effect on the 1.17 μm excitation spectrum. To demonstrate this we used a set of long pass filters to prefilter the laser beam before the heat-pipe oven. When a Schott RG695 filter was used in the LDS 722 beam, no change in the excitation spectra was seen other than that due to the power loss from reflections at the glass surfaces. However when an RG780 filter was used, the 741 nm hump disappeared from the excitation spectra and the 750 nm peak was reduced by a factor of 7. In fact the filtered LDS 722 spectrum closely resembled the LDS 765 spectrum, but the latter was ~0.6 times as intense. A look at the filtered laser spectrum showed that the short wavelength lobe was reduced in intensity by ~95% over the unfiltered case, while the main laser peak was reduced by only a factor of 2. Filtering the LDS 765 output had little effect on the results. Note that the 1.17 μm output pumping at 750 nm with LDS 722 dye is much stronger than the same wavelength emission when pumping the two-photon $4S \rightarrow 6S$ atomic transition at 728.36 nm. The latter can just barely be seen in Fig. 9.

Another interesting but as yet unexplained result is that the dips appearing in the LDS 722 excitation spectrum near 750 nm (which we have identified as corresponding to $3D_{3/2} \rightarrow nF_{5/2}$ transitions) are more pronounced in the backward than in the forward direction.

The data from LDS 765 shows that two 750 nm photons are sufficient to produce strong forward emission at 1.17 μm. However the additional presence of even a very weak source near 720 nm enhances the process dramatically. Note that the LDS 722 dye excitation spectrum (Fig. 9) demonstrates that 2 photons at 720 nm are not, by themselves, particularly efficient at producing 1.17 μm light. No other atomic lines were observed in the unfiltered LDS 722 case, indicating that the enhancement due to the 720 nm ASE lobe is not simply due to a resonant atomic process. Note also that the data presented in our previous paper [33] were all taken with LDS 722 dye with the contaminating ASE lobe at 720 nm. Thus the earlier published results were taken under the conditions of the present Fig. 9 and therefore are quite different from the results presented here in Figs. 4 and 6.

The conclusion from these studies using the filtered and unfiltered output from the LDS 722 dye laser is that one or the other step in the two-step NaK molecular excitation is greatly enhanced near 720 nm. Since the NaK $A^1\Sigma^+ \leftarrow X^1\Sigma^+$ absorption peaks near 750 nm (according to the potentials of Refs. [27] and [34]), we expect that it is the second step which is enhanced. In particular, the $v=0$ level of the ground state cannot be pumped to the K(3D) + Na(3S) dissociation limit with two 750 nm photons, but can be with one 750 and one 720 nm photon. The final explanation of these processes can only be obtained by two-laser experiments which are now underway in our laboratory.

3. Conclusions

In this paper we have reported our observations of forward and backward stimulated emission in pure potassium and mixed sodium-potassium vapor excited in the range 680–800 nm. We have found that when either vapor is excited at 728.36 nm, corresponding to the potassium $4S \rightarrow 6S$ two photon transition, we observe optically pumped stimulated emission on the $6S \rightarrow 5P$ transition. In addition we observe amplified spontaneous emission on cascade transitions, and four- and six-wave mixing signals which are nearly resonant with the $5P \rightarrow 4S$, $5S \rightarrow 4P$, and $3D \rightarrow 4P$ transitions. These results for resonant excitation are

analogous to previous results obtained in other alkalis as well as in potassium.

We have also found that when the sodium-potassium vapor is excited off resonance over the range 747–753 nm we can observe stimulated emission at 1.17 μm (potassium $3D_{3/2} \rightarrow 4P_{1/2}$). This emission, which cannot be observed in pure potassium vapor, has a strong forward to backward asymmetry (25 : 1). A weaker signal at 1.18 μm (potassium $3D_{5/2} \rightarrow 4P_{3/2}$) can also be observed under certain circumstances. We believe the large $3D_{3/2}$ population is created through a two-photon photodissociation of the NaK molecule. Sharp dips in the excitation spectra are due to coincidental depletion ot fhe upper $3D_{3/2}$ level via laser excitation to Rydberg F levels. The forward to backward asymmetry in this emission is still unexplained, but may result from either a wave-mixing process triggered by the photodissociation lasing or simply an asymmetric gain in the latter. Finally we note that the 1.17 μm forward emission is enhanced by more than an order of magnitude when the pump dye laser contains a weak (0.5%) ASE contamination near 720 nm. We believe that this enhancement results from a two-step sequence in which NaK $A^1\Sigma^+$ is first excited from the ground ($X^1\Sigma^+$) state with a 750 nm photon and then is photodissociated by a second photon near 720 nm. Note that two laser photons at 720 nm produce no emission at 1.17 μm. Further work on this two-step process is currently in progress.

Acknowledgements. We are grateful to W. R. Garrett, Mary Anne Moore, R. N. Compton, and S. J. Bejic for many helpful discussions. We also thank Scott Corey for helping with computer graphics. This work was supported by the Army Research Office under grant DAALO3-86-K-0161, and the National Science Foundation under grant PHY-8451279.

References

1. O.J. Lumpkin, Jr.: IEEE J. QE-4, 226 (1968)
2. S. Barak, M. Rokni, S. Yatsiv: IEEE J. QE-5, 448 (1969)
3. P. Agostini, P. Bensoussan, J.C. Boulassier: Opt. Commun. 5, 293 (1972)
4. W. Hartig: Appl. Phys. 15, 427 (1978)
5. J.K. Chen, C.Y.R. Wu, C.C. Kim, D.L. Judge: Appl. Phys. B 33, 155 (1984)
6. M.E. Movsesyan, T.O. Ovakimyan, S.V. Shmavonyan: Opt. Spectrosc. 61, 285 (1986)
7. S.M. Hamadani, J.A.D. Stockdale, R.N. Compton, M.S. Pindzola: Phys. Rev. A 34, 1938 (1986)
8. P.P. Sorokin, J.R. Lankard: J. Chem. Phys. 54, 2184 (1971)
9. P.P. Sorokin, J.J. Wynne, J.R. Lankard: Appl. Phys. Lett. 22, 342 (1973)
10. P.-L. Zhang, Y.-C. Wang, A.L. Schawlow: J. Opt. Soc. Am. B 1, 9 (1984)
11. C.Y.R. Wu, J.K. Chen: Opt. Commun. 50, 317 (1984)
12. N.V. Znamenskii, A.P. Lutsenko, M.G. Piskarev: Opt. Spectrosc. (USSR) 59, 545 (1985)
13. J. Krasinski, D.J. Gauthier, M.S. Malcuit, R.W. Boyd: Opt. Commun. 54, 241 (1985)
14. D.G. Sarkisyan, A.A. Badalyan, S.O. Sapondzhyan, G.A. Torosyan: Sov. J. Quant. Electron. 16, 571 (1986)
15. K. Mori, Y. Yasuda, N. Sokabe, A. Murai: Opt. Commun. 57, 418 (1986)
16. V.E. Mnuskin, V.G. Nikiforov, A.N. Tokareva, B.F. Trinchuk: Sov. J. Quant. Electron. 17, 241 (1987)
17. V. Vaichaitis, M. Ignatavichyus, V.A. Kudryashov, Yu.N. Pimenov, R. Yakite: Sov. J. Quant. Electron. 17, 478 (1987)
18. Z.G. Wang, H. Schmidt, B. Wellegehausen: A. Phys. B 44, 41 (1987)
19. Z.-G. Wang, L.-J. Qin, L.-S. Ma, Y.-Q. Lin, I.-S. Cheng: Opt. Commun. 51, 155 (1984)
20. D. Krökel, M. Hube, W. Luhs, B. Wellegehausen: Appl. Phys. B 37, 137 (1985)
21. Z.G. Wang, L.J. Qin, K.C. Zhang, I.S. Cheng: Appl. Phys. B 41, 125 (1986)
22. S.G. Dinev, I.G. Koprinkov, I.L. Stefanov: Appl. Phys. B 39, 65 (1986)
23. S.G. Dinev, I.L. Stefanov: Appl. Phys. B 44, 235 (1987)
24. S.G. Dinev, I.G. Koprinkov, I.L. Stefanov: Opt. Commun. 52, 199 (1984)
25. H.H. Wu, T.C. Chu, C.Y.R. Wu: Appl. Phys. B 43, 225 (1987)
26. H. Komine, R.L. Byer: J. Appl. Phys. 48, 2505 (1977)
27. A.J. Ross, C. Effantin, J. d'Incan, R.F. Barrow: Mol. Phys. 56, 903 (1985)
28. R.N. Compton: Private communication
29. C.B. Collins, J.A. Anderson, D. Popescu, I. Popescu: J. Chem. Phys. 74, 1053 (1981)
30. C.B. Collins, F.W. Lee, J.A. Anderson, P.A. Vicharelli, D. Popescu, I. Popescu: J. Chem. Phys. 74, 1067 (1981)
31. B. Wellegehausen: IEEE J. QE-15, 1108 (1979)
32. B. Wellegehausen: In *Metal Bonding and Interactions in High Temperature Systems*, ed. by J.L. Gole, W.C. Stwalley, ACS Symposium Series 179 (American Chemical Society, Washington, D.C. 1982) p. 461
33. B.K. Clark, M. Masters, J. Huennekens: Wave-mixing processes in sodium-potassium vapor. In *Proceedings of the Third International Laser Science Conference*, ed. by W.C. Stwalley (to be published)
34. A.J. Ross, R.M. Clements, R.F. Barrow: J. Molec. Spectrosc. 127, 546 (1988)

Appendix 5

Appl. Phys. B 49, 155–161 (1989)

Applied Physics B Photophysics and Laser Chemistry

NaK $2^1\Sigma^+ \rightarrow 1^1\Sigma^+$ Band Optically Pumped Laser Near 1.02 μm

B. K. Clark*, W. T. Luh, and J. Huennekens

Department of Physics, Lehigh University, Bethlehem, PA 18015, USA

Received 8 December 1988 Accepted 1 March 1989

Abstract. Optically pumped laser emission has been observed on the NaK $2(A)^1\Sigma^+ \rightarrow 1(X)^1\Sigma^+$ electronic state transition. The emission occurs between 1.015 and 1.035 μm when a sodium-potassium heat-pipe oven is pumped with 695–745 nm pulsed dye laser radiation. The laser emission occurs on many ro-vibrational transitions without the use of cavity mirrors. However, the addition of a simple cavity increases both the number of observed lasing transitions and the amplitude of the emission on each line. We report our results for the dependence of the emission intensity on pump laser power, oven temperature, and buffer gas pressure.

PACS: 42.55.Hq, 33.50.Dq

Optically pumped lasers (OPL's) based upon electronic transitions in alkali diatomic molecules were first demonstrated in sodium vapor by Henesian et al. in 1976 [1]. This pulsed alkali OPL was soon followed by a report of continuous laser action on the Na_2 $B \rightarrow X$ band [2]. Since that time, various studies have produced OPL emission based upon the $A \rightarrow X$ and $B \rightarrow X$ bands of the homonuclear alkali molecules Li_2, Na_2, and K_2 [3–14]. OPL emission from more highly excited states of the sodium molecule has also been observed [15–18]. Of particular interest to the present study, OPL emission has been observed from the heteronuclear alkali molecule NaRb [19]. These alkali OPL's have now been made to operate on a large number of fixed frequency lines in the range 400–910 nm as well as on several lines in the 2.5 μm region. Other dimers such as Bi_2, S_2, Te_2, and I_2 have also been made to yield stimulated emission in the visible and near-infrared regions through OPL transitions. Such lasers have applications in gain modulated spectroscopy [20] and in the determination of electronic transition moments [21].

Optically pumped alkali lasers may be treated as three level lasers as is shown in Fig. 1. In general, two mechanisms are responsible for the OPL emission. In the first, a thermally populated level of the ground electronic state is pumped on-resonance in an allowed ro-vibrational transition to the upper laser level. Lasing then occurs to thermally unpopulated high lying levels of the ground state. The second mechanism is a Raman process where the excitation and emission wavelengths can be either resonant or slightly off resonant with the same three levels. This Raman process leads to asymmetric gain favoring emission parallel to the direction of the pump laser propagation [4, 22].

In the present work we report laser emission on NaK $2^1\Sigma^+ \rightarrow 1^1\Sigma^+$ electronic transitions. The observed OPL lines consist of P and R transitions originating from vibrational levels in the range $v' = 17$–33 of the $2^1\Sigma^+$ electronic state and terminating on the $v'' = 36$–53 levels of the $1^1\Sigma^+$ ground state. The initial levels that are excited by the pump laser are the thermally populated ro-vibrational levels of the $1^1\Sigma^+$ state ($v'' = 0$–7). With the high gain that is obtained using a high-power, pulsed dye laser as the excitation source, lasing (or more correctly amplified spontaneous emission) can be observed on many lines without the use of cavity mirrors. However, the addition of a simple cavity increases both the number of lasing transitions and the amplitude of each emis-

* Present address: Dept. of Physics, Illinois State University, 311 Moulton Hall, Normal, IL 61761, USA

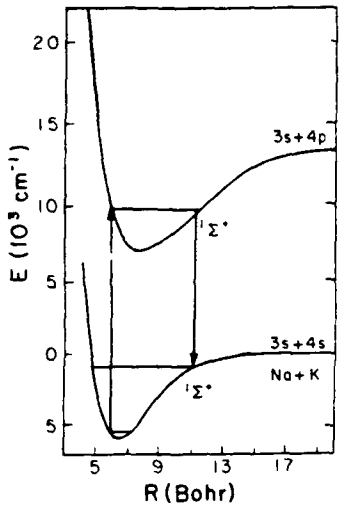

Fig. 1. Schematic potential energy level diagram for the NaK molecule showing the observed OPL transitions. The arrow pointing up represents the pumping process from low lying levels of the $1^1\Sigma^+$ state to various levels of the $2^1\Sigma^+$ state. The downward arrow represents OPL emission from the pumped level to initially unpopulated, high-lying levels of the $1^1\Sigma^+$ state

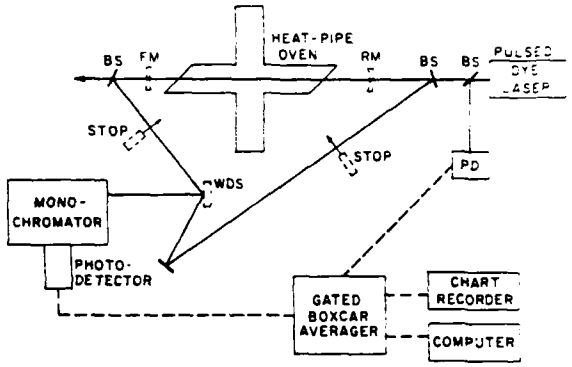

Fig. 2. Experimental set-up. Here PD, BS, RM, FM, and WDS represent photodiode, beam splitter, rear cavity mirror, forward cavity mirror, and white diffusing surface, respectively

sion line. While the lasing transitions reported here are similar to the other alkali OPL's, the present observations represent only the second case of OPL emission involving the heteronuclear alkali molecules and the first such observation in the NaK molecule. In addition, the present work extends the known alkali dimer laser emissions into the 1.0 μm region.

1. The Experiment

The experimental apparatus is shown in Fig. 2. A vapor consisting of a mixture of sodium and potassium was contained in a 4-way cross, stainless-steel, heat-pipe oven. The initial mixture of potassium and sodium was ~2:1 although temperature cycling and subsequent reloadings caused the ratio of potassium to sodium atoms in the vapor phase to vary with time. The oven also contained argon buffer gas which was varied in pressure over the range 1–130 mbar. Since the oven was typically not operated in the heat-pipe mode, the temperature could be independently varied from ~400–600 °C. To verify the molecular species involved in the OPL process, a second heat pipe, containing pure potassium vapor, could be substituted for the Na–K oven.

The Na–K vapor was pumped by a dye laser which was in turn pumped by a frequency doubled, pulsed Nd:YAG laser. Calibration of the dye laser frequency was carried out using the optogalvanic effect in a neon-filled hollow cathode lamp. We used the dye LDS 722, which tunes over the range 690–760 nm. However, most of the OPL pumping occurred between 695 and 745 nm. The peak power of the dye laser was ~1 MW in this range. The dye laser beam was either unfocused or weakly focused into the heat-pipe oven.

Emission from the Na–K oven directed generally parallel or antiparallel to the pump beam (referred to as forward and backward emission, respectively) could be monitored by the use of beam splitters which directed the beams to a white diffusing surface placed in front of a monochromator. Light passing through the monochromator was detected with a liquid nitrogen-cooled, intrinsic germanium detector. In all cases, appropriate color filters were used to eliminate second and higher order diffraction from the monochromator grating, as well as unwanted pump laser light. The detector output was then processed by a boxcar-averager and sent to both a chart recorder and a computer for later analysis. With this setup, only stimulated emissions from the oven could be detected since no focusing optics were employed along their optical paths.

The relative forward to backward detection efficiencies were calibrated with the oven cold by first aligning the forward detection optics and then retroreflecting the pump laser beam upon itself and through the backward detection optics. A beam splitter was used in the backward path as shown in Fig. 2, while either a beam splitter (for roughly equal forward to backward efficiencies) or a mirror (for higher sensitivity) was used in the forward direction. With this calibration of the forward to backward efficiencies, we could determine the relative forward to backward OPL intensity ratio. Finally, for the highest sensitivity the white diffusing surface was sometimes bypassed, and the stimulated emission sent directly into the monochromator using highly-reflective mirrors.

Under these conditions, neutral density filters were needed to regulate the light levels.

Normally the 0.75 m monochromator was set to pass light at a specific wavelength in the 1.015–1.035 μm region with a bandpass of 0.3–6.7 nm. For laser excitation scans, the monochromator slits were set to 3 mm (yielding a spectral resolution of 6.7 nm) and the laser frequency was scanned. With the laser linewidth of $\sim 0.1\ cm^{-1}$, well defined rotational-vibrational progressions could be observed.

The power dependence of the OPL emission at 1.02 μm was determined using a series of neutral density filters which were calibrated in place using a photodiode (see Fig. 2). By referencing the stimulated emission intensity at 1.02 μm to the pump laser intensity and taking account of the relative efficiency of the intrinsic germanium detector at the two wavelengths, the conversion efficiency of this OPL emission could be determined. The relative efficiency of the detection system at the pump laser and OPL wavelengths was determined following the procedures outlined in [23] utilizing a tungsten halogen lamp with known relative emission vs. wavelength.

Most of the studies were carried out without the use of OPL cavity mirrors. However, several cavity designs were tried in attempts to enhance the OPL emission. In all cases the rear cavity mirror was chosen to have a 3 m radius of curvature, >99% reflectivity at 1.02 μm and >80% transmission between 700 and 800 nm. Several forward cavity mirrors were tried. The first was ~50% reflecting at 1.02 μm and >80% transmitting between 700 and 800 nm, with a 3 m radius of curvature. The second was a flat quartz window with one side antireflection coated. Its effective reflectivity was ~5%. The third was a plane sapphire window with a reflectivity of ~7% from each surface.

Laser excitation scans were made without any cavity mirrors and for each forward cavity mirror (including the case of no forward reflector) in conjunction with the rear high reflector. The dependence of the 1.02 μm emission on pump laser power was measured with the sapphire window cavity and with no cavity present. The effect of each cavity configuration on the intensity of selected lasing transitions was studied by misaligning and then realigning each mirror to its optimal position.

2. Results and Discussion

The forward emission at 1.02 μm was first observed when we heated the Na–K heat-pipe oven above 500 °C at ~50 mbar buffer gas pressure during studies of parametric wave-mixing and other coherent emissions [24]. With the monochroamtor set to specific wavelengths near 1.02 or 1.03 μm, we obtained laser excitation scans which show ro-vibrational progressions corresponding to P and R line absorptions on the NaK $2(A)^1\Sigma^+ \leftarrow 1(X)^1\Sigma^+$ band (Fig. 3). Most of the observed transitions originate from low lying vibrational levels of the ground state. The upper state vibrational level ranges from $v' = 17$–33.

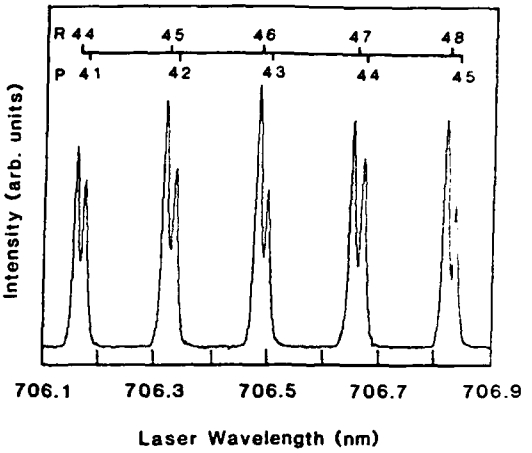

Fig. 3. Laser excitation spectrum corresponding to OPL emission at 1.021 μm (monochromator bandpass ~1.4 nm). The labelled P and R absorption lines are part of the $2^1\Sigma^+(v'=28) \leftarrow 1^1\Sigma^+(v''=0)$ band. The heat-pipe oven was operated at 519 °C with an argon buffer gas pressure of 50 mbar

The 1.02–1.03 μm OPL emission detected by the germanium detector is the $2^1\Sigma^+ \rightarrow 1^1\Sigma^+$ downward transition to initially unpopulated, high-lying levels of the ground state ($v'' = 36$ to 53). Due to the very high density of absorption lines leading to OPL emission in the vicinity of 1.03 μm (which is near the long-wavelength satellite of the NaK $2^1\Sigma^+ \rightarrow 1^1\Sigma^+$ band), we did not attempt to carry out a detailed identification of the lines in the spectrum. However, using the accurate experimental constants for the NaK $1^1\Sigma^+$ and $2^1\Sigma^+$ states from [25, 26], respectively, we were able to assign individual ro-vibrational absorption lines in the relatively simple region of the spectrum between 700 and 715 nm. Note that K_2 could be ruled out as the source of the OPL emission by the fact that no such emission was observed when pumping pure potassium vapor in this spectral range under similar conditions. Na_2 could also be eliminated since there are no Na_2 emission bands in the 1.02–1.03 μm region.

Using the 0.75 m monochromator with a fixed pump wavelength and 100 μm slits (0.3 nm resolution), the OPL emission near 1.02 μm could be resolved into an $R(J-1)$ and $P(J+1)$ doublet of one vibrational transition of the $2^1\Sigma^+ \rightarrow 1^1\Sigma^+$ band. The specific case of $J = 49$, pumped via the

$$2^1\Sigma^+(v'=28,\ J'=49) \leftarrow 1^1\Sigma^+(v''=0,\ J''=48)$$

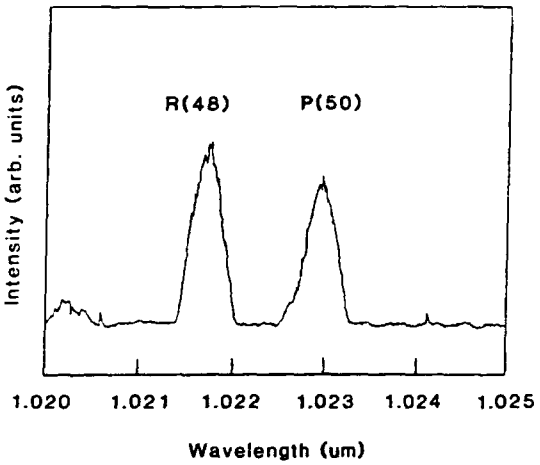

Fig. 4. Monochromator scan of the OPL emission with the pump laser tuned to the

$2^1\Sigma^+(v'=28,\ J'=49) \leftarrow 1^1\Sigma^+(v''=0,\ J''=48)$

transition. The oven temperature was 517 °C, and the buffer gas pressure 33 mbar. The monochromator slits were set to give a resolution of 0.3 nm. This spectrum was taken using the high reflecting back cavity mirror and the sapphire window as the forward mirror. The weak line observed at 1.0202 μm has not been identified, but probably represents a weaker pumping from some higher level of the ground state $[1^1\Sigma^+(v''>0)]$. The separation of the two main peaks is in agreement with the energy splitting of the $v''=46$, $J''=48$ and 50 levels of the ground state. The observed OPL wavelengths and calculated Franck-Condon factors (see text) are also consistent with the interpretation that this OPL emission represents a single *P*, *R* doublet terminating at $1^1\Sigma^+(v''=46)$

transition is shown in Fig. 4. The observed emission peak positions are in agreement with those predicted for the

$$2^1\Sigma^+(v'=28,\ J'=49) \rightarrow 1^1\Sigma^+(v''=46,\ J''=48,50)$$

lines from the constants of [25, 26]. (Note that although the $v''=0 \rightarrow v'=28$ band was by no means the most effective at producing OPL emission, it occurs in a relatively simple region of the spectrum where individual line assignments were possible. Consequently, much of our subsequent data analysis, such as power dependences and cavity studies, were carried out using lines of this band.)

Longer monochromator scans indicate that, with our level of sensitivity, each upper level pumped by the laser will, in general, only produce stimulated emission on a single *P*, *R* doublet of one vibrational band. We presume that these are the transitions with the highest gain, which is determined by the relevant Franck-Condon factors. These were calculated using the computer program INTENSITY [27] and RKR potential calculated from the NaK $2^1\Sigma^+$ and $1^1\Sigma^+$ molecular constants of Ross et al. [25, 26]. In Table 1 we list the strongest downward transitions (as determined from these calculated Franck-Condon factors) for various upper state vibrational levels. For each of the bands that were investigated in detail, lasing was observed only on the vibrational transition from the pumped upper level that has the largest Franck-Condon factor. In a homogeneously broadened gain medium, the upper level population gets clamped at the threshold value for the transition with the largest gain [16, 28]. In the present case, we are dealing with a Doppler (and therefore inhomogeneously) broadened gain medium. However, it is possible that a similar population clamping mechanism may be responsible for this observation of lasing on only one vibrational transition. It is likely that in cases where Franck-Condon factors are nearly equal, lasing could be observed on more than one vibrational band from a single upper level. It is also probable that weaker vibrational bands could be made to lase with the addition of a tuning element to the cavity. However, this was not attempted in the present work.

Table 1. List of the strongest downward transitions of the NaK $2^1\Sigma^+ \rightarrow 1^1\Sigma^+$ band (defined by the Franck-Condon factors) for a given upper vibrational state v'. Only those bands which radiate most strongly in the 1.01–1.035 μm range are listed. These are the bands which are most likely to contribute to the observed OPL emission. Column three gives the Franck-Condon factor $q \equiv |\langle v'|v''\rangle|^2$ for each transition, while column four gives roughly the band center wavelength [defined by the wavelength of the $Q(50)$ line]. Here, the most probable rotational level is $\sim J=50$ for our experimental temperatures

v'	v''	q	λ[μm]
17	36	0.1921	1.0334
18	37	0.2070	1.0337
19	38	0.2257	1.0340
20	39	0.2471	1.0340
21	40	0.2682	1.0339
22	41	0.2837	1.0337
23	42	0.2851	1.0332
24	43	0.2628	1.0326
25	43	0.2236	1.0251
26	44	0.2702	1.0244
27	45	0.2912	1.0235
28	46	0.2651	1.0224
29	47	0.1848	1.0211
30	47	0.1427	1.0139
31	50	0.1689	1.0232
32	51	0.1259	1.0210
33	53	0.1259	1.0231

In Fig. 5 we present a plot of the total OPL emission, with the laser tuned to the

$2^1\Sigma^+(v'=28,\ J'=49) \leftarrow 1^1\Sigma^+(v''=0,\ J''=48)$

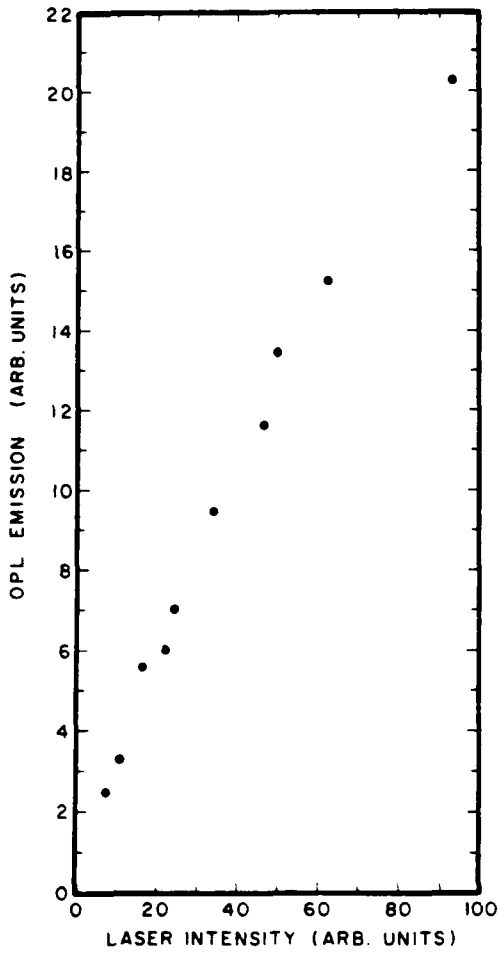

Fig. 5. OPL emission intensity as a function of pump laser power with the laser tuned to the $R(48)$ line of the $v''=0 \rightarrow v'=28$ transition. For these measurements, the oven temperature was 519°C and the buffer gas pressure 35 mbar. The monochromator bandpass was 6.7 nm centered at 1.0224 μm. Laser power of 100 corresponds to the full available pump power (~1 MW). The pump laser beam was weakly focused to a diameter of ~0.1 cm in the oven. The sapphire window cavity was used for these data

transition, as a function of pump laser power. These data were taken with the sapphire window cavity in place. However, similar results were obtained without cavity mirrors. As can be seen for this relatively weak transition at fairly high pressure and temperature, the power dependence is roughly linear. However, other levels may show different power dependences due to saturation effects, etc. In particular, at lower temperatures (~460°C) we observed not only saturation of some signals, but even reduced OPL emission as the laser power was increased to the highest levels. At lower laser power, all levels show the roughly linear power dependence seen in Fig. 5.

Using the sapphire window cavity and a monochromator bandpass of 6.7 nm, we found that the OPL emission could be produced by many absorption lines in addition to those clearly observed in the no-cavity case. Figure 6 shows a specific case in which the $v''=1$ to $v'=29$ absorption band can be seen overlapping the $v''=0$ to $v'=28$ band when the cavity is in place. These lines of the 1–29 band are very weak in the no-cavity spectrum. In some cases, bands which were very weak in the no-cavity case were enhanced by the cavity to intensities which were comparable to those of the strong bands.

Several other reflectors were tried as the forward cavity mirror. Use of either the quartz window, the 50% reflector, or no forward reflector at all resulted in essentially the same OPL emission as with the sapphire window. Strong lines (those observed clearly with no back reflector) generally only increased in intensity by ~10% with the use of a forward mirror. However, for these lines the back mirror and its alignment proved more critical, typically increasing the forward emission by a factor of ~2.5. For weak lines (those which were not observed clearly without a back reflector), the observed intensity typically increased by a factor of 4–6 with the addition of a forward cavity mirror.

The conversion efficiency of pump laser radiation to OPL emission was measured on the

$$2^1\Sigma^+(v'=28,\ J'=49) \rightarrow 1^1\Sigma^+(v''=46,\ J''=48)$$

transition following pumping from $v''=0, J''=48$ of the ground state. For these measurements, the heat-pipe oven temperature was 523°C and the buffer gas pressure 40 mbar. The intensity of the laser beam passing through the heat-pipe oven was measured with the oven cold and hot. Then the intensity of the OPL emission was measured. The ratio of OPL emission to pump laser intensity transmitted through the cell was $\sim 10^{-4}$. Note that this conversion efficiency should be taken as only an order of magnitude estimate since it depends strongly on the buffer gas pressure, cell temperature, and vapor composition (see below). With no cavity present, we also measured a forward to backward intensity ratio of ~10:1.

For wavelengths in the range 700–720 nm, we found that the pump laser transmission through the oven at 515°C and a buffer gas pressure of 50 mbar was ~50% of that observed with the oven cold. To test whether transmission of the pump laser beam through the heat-pipe oven was noticably reduced when pumping a transition giving rise to OPL emission, a beam-splitter was used to send a small amount of the transmitted pump laser radiation to a photodiode. A laser excitation spectrum, where the absorption of the pump laser radiation as measured by the photodiode was compared to OPL emission, showed no measur-

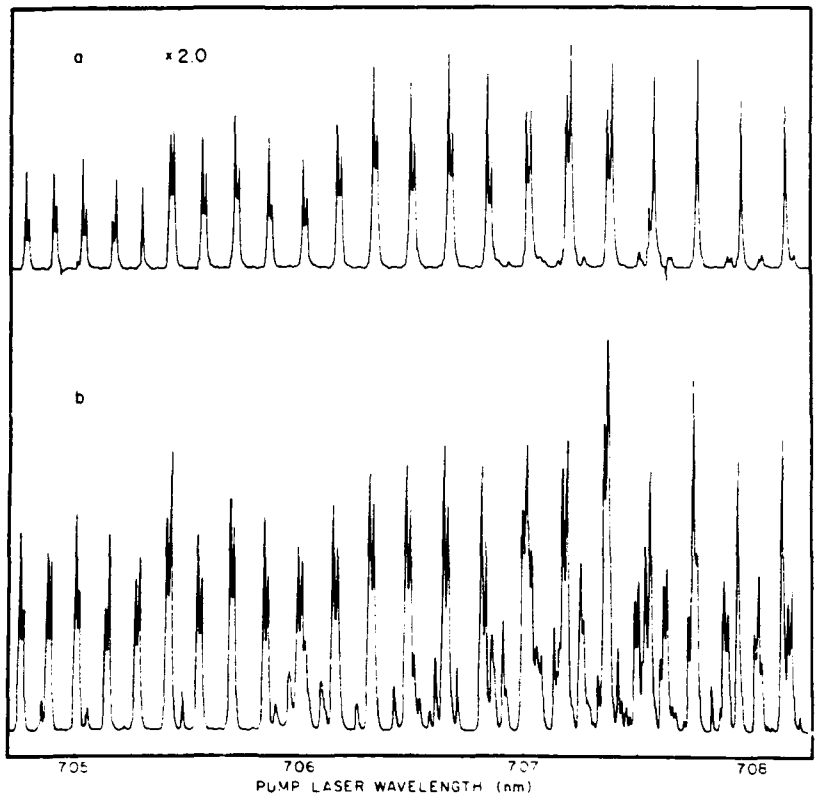

Fig. 6. a No OPL laser cavity and **b** sapphire window cavity laser excitation scans. The monochromator monitored emission at 1.022 μm with a resolution of 6.7 nm. The no-cavity scan clearly shows the $2^1\Sigma^+(v'=28) \leftarrow 1^1\Sigma^+(v''=0)$ ro-vibrational progression, while the sapphire window cavity scan shows in addition lines from the $2^1\Sigma^+(v'=29) \leftarrow 1^1\Sigma^+(v''=1)$ band. In both cases the buffer gas pressure was 35 mbar and the heat-pipe central temperature 515°C

able decrease in the transmitted pump laser intensity specifically at the OPL absorption lines.

The observed OPL emission is a strong function of the vapor composition which is difficult to regulate in the mixed alkali oven. When the vapor is relatively rich in potassium, the most intense emissions are observed when pumping in the range 700–730 nm. At longer wavelengths the pump light is strongly absorbed in the oven, and the OPL emission is greatly reduced. We believe that a partial separation of the sodium and potassium vapors occurs in the oven and that the pump light can be absorbed by the K_2 $A^1\Sigma^+ \leftarrow X^1\Sigma^+$ band before reaching the region of greatest NaK density. Under such conditions, little or no NaK OPL emission can be seen for pump wavelengths greater than 740 nm despite the fact that the maximum of the NaK $2^1\Sigma^+ \leftarrow 1^1\Sigma^+$ absorption band lies in this region. With a more sodium rich mixture, the strongest OPL emissions are seen when pumping in the 720–745 nm region as one would expect from consideration of the NaK state constants and Franck-Condon factors.

Despite these composition dependent effects, we wanted to qualitatively investigate the temperature and buffer gas pressure dependence of the OPL emission for a fixed vapor mixture. This was carried out with a mixture relatively rich in potassium which was also used for the bulk of the other data. For a fixed buffer gas pressure of 33 mbar, we first observed OPL emission from the pumped level $2^1\Sigma^+(v'=28, J'=49)$ at 495°C. The intensity increased until 548°C when the heat pipe could no longer be operated at this fixed pressure. Note that at the lower temperatures studied here, the oven was not operating in the heat-pipe mode because the alkali vapor pressure was below that of the buffer gas. This resulted in mixing of buffer gas with the alkali in the central region of the oven. At higher temperatures, heat-pipe operation was established, resulting in an alkali vapor pressure equal to that of the buffer gas. In this regime, the central region of the oven contains only alkali vapor. When the power to the heaters was raised even further, the heat-pipe regime again broke down and vaporization of the alkali in the central region became so rapid that the pipe was soon occluded by alkali metal condensing near the ends of the wick.

Pumping the same ro-vibrational transition, the OPL emission as a function of buffer gas pressure was also studied at a fixed temperature of 515°C. Under these conditions, the OPL intensity was greatest at 15 mbar and had almost disappeared by 60 mbar.

Pressures below 15 mbar could not be studied at this temperature because the pipe soon occluded due to a break down of the heat-pipe mode of operation.

The increase in OPL emission as temperature increased can probably be linked to the increasing number density of NaK molecules. We expect the signals to continue to increase with temperature until the pump beam attenuation becomes too severe. The decrease in OPL emission with increasing buffer gas pressure probably results from collisional excitation transfer out of the upper OPL level. It is possible that conversion efficiencies of 10^{-3} are achievable with this OPL system by further optimization of the buffer gas pressure, temperature, and cavity parameters.

3. Conclusions

In the present work we report observation of optically pumped laser emission in the region of 1.015–1.035 μm based upon $2^1\Sigma^+ \rightarrow 1^1\Sigma^+$ transitions of the NaK molecule. The large gain produced using high-power, pulsed laser excitation resulted in stimulated emission on many ro-vibrational transitions without the use of cavity mirrors. Under these conditions, we observed a forward to backward intensity ratio of $\sim 10:1$. The addition of a simple cavity (which contains no dispersing elements) increased the amplitude of these emissions and caused lasing to occur for many other $2^1\Sigma^+(v', J') \leftarrow 1^1\Sigma^+(v'', J'')$ absorptions which were below our detection limit in the no-cavity case. We investigated the dependences of the OPL emissions on cell temperature, buffer gas pressure, and pump laser intensity.

These results represent the first observation of OPL emission in the NaK molecule and demonstrate that alkali OPL's can be made to operate past 1.0 μm which, in the case of NaK, is near the $2^1\Sigma^+ - 1^1\Sigma^+$ band ($A - X$ band) satellite. The addition of a tunable cavity and further optimization of vapor parameters should result in laser action on many other lines in this spectral region.

Acknowledgements. The authors would like to thank the referees for several helpful comments and suggestions. This work was supported by the Army Research Office under grant DAALO3-86-K-0161, and the National Science Foundation under grant PHY-8451279.

References

1. M.A. Henesian, R.L. Herbst, R.L. Byer: J. Appl. Phys. **47**, 1515 (1976)
2. B. Wellegehausen, S. Shahdin, D. Friede, H. Welling: Appl. Phys. **13**, 97 (1977)
3. H. Itoh, H. Uchiki, M. Matsuoka: Opt. Commun. **18**, 271 (1976)
4. B. Welleghausen: IEEE J. QE-**15**, 1108 (1979)
5. B. Welleghausen: In *Metal Bonding and Interactions in High Temperature Systems*, ed. by J.L. Gole, W.C. Stwalley, ACS Symposium Series 179 (American Chemical Society, Washington, DC 1982) p. 461
6. C.N. Man-Pichot, A. Brillet: In *Metal Bonding and Interactions in High Temperature Systems*, ed. by J.L. Gole, W.C. Stwalley, ACS Symposium Series 179 (American Chemical Society, Washington, DC 1982) p. 487
7. A.R. Rajaei-Rizi, J.T. Bahns, K.K. Verma, W.C. Stwalley: Appl. Phys. Lett. **40**, 869 (1982)
8. P.L. Jones, U. Gaubatz, U. Hefter, K. Bergmann, B. Wellegehausen: Appl. Phys. Lett. **42**, 222 (1983)
9. J.T. Bahns, K.K. Verma, A.R. Rajaei-Rizi, W.C. Stwalley: Appl. Phys. Lett. **42**, 336 (1983)
10. W. Luhs, M. Hube, U. Schottelius, B. Wellegehausen: Opt. Commun. **48**, 265 (1983)
11. W. Luhs, B. Wellegehausen: Opt. Commun. **46**, 121 (1983)
12. C.N. Man, A. Brillet: J. Appl. Phys. **56**, 71 (1984)
13. W.T. Luh: Ph.D. Thesis, University of Iowa (1985)
14. W.T. Luh, J.T. Bahns, W.C. Stwalley: J. Mol. Spectrosc. **128**, 82 (1988)
15. B. Wellegehausen, W. Luhs, A. Topouzkhanian, J. d'Incan: Appl. Phys. Lett. **43**, 912 (1983)
16. P. Bernage, P. Niay, H. Bocquet: J. Mol. Spectrosc. **98**, 304 (1983)
17. Z.-G. Wang, Y.-C. Wang, G.P. Morgan, A.L. Schawlow: Opt. Commun. **48**, 398 (1984)
18. Z.G. Wang, H.R. Xia, L.S. Ma, Y.Q. Lin, S. Cheng: Appl. Phys. B **37**, 233 (1985)
19. V.M. Kaslin, O.F. Yakushev: Soviet J. Quant. Electron. **13**, 1575 (1983)
20. H.S. Schweda, G.K. Chawla, R.W. Field: Opt. Commun. **42**, 165 (1982)
21. J.B. Koffend, R. Bacis, R.W. Field: J. Chem. Phys. **70**, 2366 (1979)
22. U. Hefter, J. Eichert, K. Bergmann: Opt. Commun. **52**, 330 (1985)
23. R. Stair, W.E. Schneider, J.K. Jackson: Appl. Opt. **2**, 1151 (1963)
24. B.K. Clark, M. Masters, J. Huennekens: Appl. Phys. B **47**, 159 (1988)
25. A.J. Ross, C. Effantin, J. d'Incan, R.F. Barrow: Mol. Phys. **56**, 903 (1985)
26. A.J. Ross, R.M. Clements, R.F. Barrow: J. Mol. Spectrosc. **127**, 546 (1988)
27. (a) W.T. Zemke, W.C. Stwalley: Quant. Chem. Prog. Exch. Bull. **4**, 79–80 (1984), (b) K.M. Sando: Private communication
28. A. Yariv: *Introduction to Optical Electronics* (Holt, Rinehart and Winston, New York 1976) p. 171

Appl. Phys. B ■■, ■■■-■■■ (1989)
1-11

Appendix C

Applied Physics B Photophysics and Laser Chemistry

830 nm Emission in Sodium Vapor

W. T. Luh, Yan Lee, and J. Huennekens

Department of Physics, Lehigh University, Bethlehem, PA 18015, USA

Received 13 March 1989 Accepted 17 April 1989

Abstract. We demonstrate that the intriguing 830 nm coherent emission, which is observed when sodium vapor is pumped with a high-power pulsed laser tuned near the $3S \rightarrow 4D$ two-photon transition, is due to an axially phase-matched six-wave mixing process. This conclusion is based upon the observation of emission near 584 nm, which is coupled to the 830 nm emission in the six-wave mixing process: $\omega_1 + \omega_2 = 2\omega_L - \omega_{4D \rightarrow 4P} - \omega_{4P \rightarrow 3D}$. In addition, we have observed coherent emission near 1.16 μm, which is due to an analogous process involving cascade through the $4S$ (as opposed to the $3D$) state. We calculate the wavelengths of all photons involved in these processes using the standard formulas of parametric wave-mixing theory, and show that they can be predicted to within experimental uncertainties. Finally we report observations of significant blue shifts of the 830 nm and 1.16 μm emissions in a mixed sodium-potassium vapor. These shifts can be readily understood by considering the effect of the potassium on the frequency-dependent refractive index of the vapor. Due to these results, other recent interpretations of the 830 nm emission as stimulated excimer emission on the Na_2 $1^3\Sigma_g^+ \rightarrow 1^3\Sigma_u^+$ band must now be rejected.

PACS: ■■■■

When alkali vapors are pumped by high-power lasers tuned near two-photon allowed atomic transitions, a number of coherent and stimulated emissions can be observed. These include optically pumped stimulated emission (OPSE), stimulated hyper-Raman scattering (SHR), amplified spontaneous emission (ASE) and angle phase-matched four- and six-wave mixing (see [1-7] and references therein for an introduction to the growing literature in this field). Recently, axially phase-matched four- and six-wave mixing in sodium vapor excited near the $3S \rightarrow 3D$, $4D$ two-photon transitions has been identified experimentally and explained theoretically [8, 9]. In addition to these atomic processes, the laser frequency may overlap one or more ro-vibrational transitions of the alkali molecules that are also present in the vapor. This can result in dimer lasing (or more correctly ASE in the absence of an optical cavity) on the bound-bound electronic transitions [10-12].

The present study concerns the strong coherent emission at 830 nm which is observed when sodium vapor is pumped near the $3S \rightarrow 4D$ two-photon transition. This emission has been the subject of several studies over the last several years, the first of which (to the best of our knowledge) being that of Dinev et al. [13]. These authors identified the 830 nm emission as excimer lasing on the Na_2 $1^3\Sigma_g^+ \rightarrow 1^3\Sigma_u^+$ bound-free transition since the emission spectrum appears broad and band-like and since this particular triplet band is the only known atomic or molecular emission which occurs in sodium vapor in this wavelength region [14, 15]. In addition, they identified a sharp feature near 840 nm, which occurs under the same experimental conditions, as a bound-bound cascade transition involving higher molecular states. The proposed mechanism involves collisional excitation transfer from the $4D$ excited state to a highly-excited bound triplet state of Na_2. The molecule then cascades in bound-bound stimulated transitions (one of them producing the 840 nm emission) down to the lowest vibrational level of the $1^3\Sigma_g^+$ state. The 830 nm emission results from the bound-free $1^3\Sigma_g^+ \rightarrow 1^3\Sigma_u^+$ transition, which is the final step of the cascade.

A later study by Wang et al. [6] showed that the 840 nm emission was actually an angle phase-matched six-wave mixing process satisfying the energy conser-

vation equation

$$\omega_{840} = 2\omega_L - (\omega_{4D\to 4P} + \omega_{4P\to 3D} + \omega_L) \quad (1)$$

and the momentum conservation equation

$$\mathbf{k}_{840} = 2\mathbf{k}_L - (\mathbf{k}_{4D\to 4P} + \mathbf{k}_{4P\to 3D} + \mathbf{k}_L), \quad (2)$$

where ω_L and $\mathbf{k}_L$ are the laser frequency and wave vector. Since in general, $\mathbf{k} = (n\omega/c)\hat{k}$ where n is the (frequency dependent) index of refraction, (1) and (2) can only both be satisfied if the 840 nm emission propagates in a cone centered on the pump laser axis (Fig. 1a). Under the same experimental conditions that produced the 830 and 840 nm emissions, Wang et al. also observed Na_2 $1(A)^1\Sigma_u^+ \to 1(X)^1\Sigma_g^+$ stimulated emission in the region between 784 and 800 nm [Ref. 6, Fig. 4]. This is due to the fact that the laser, which is tuned near the $3S \to 4D$ two-photon atomic transition, coincidentally also pumps various $1^1\Sigma_u^+ \leftarrow 1^1\Sigma_g^+$ rovibrational transitions. In an interesting experiment, Wang et al. were able to completely supress the dimer emissions by superheating the vapor using a hot wire passing down the axis of their heat-pipe oven parallel to the pump beam axis. This superheating, which decreased the number of bound dimers thereby dropping the $1^1\Sigma_u^+ \to 1^1\Sigma_g^+$ stimulated emission below threshold, did not affect either the 830 or the 840 nm emission intensity. This led to the conclusion that the 830 nm emission was probably not due to any process which involved the bound, ground state molecules. In addition, they showed that placing the oven inside an optical cavity enhanced the dimer emission near 790 nm but not the emissions at 830 and 840 nm. Although it was not possible to rule out the excimer explanation of the 830 nm emission as a result of these experiments (since bound $1^3\Sigma_u^+$ molecules and colliding atom pairs interacting along the $1^3\Sigma_u^+$ potential curve would not be depleted by the superheating), Wang et al. concluded from the strong similarities to the 840 nm signals and other evidence, such as the strong forward to backward emission asymmetry, that the 830 nm emission was probably also an atomic parametric process.

Very recently, Bajic et al. [17] reported new experimental data on the 830 nm emission, and concluded that it was indeed stimulated excimer emission on the $1^3\Sigma_g^+ \to 1^3\Sigma_u^+$ band of Na_2. This conclusion was based on the broad excitation spectrum (see [Ref. 16, Fig. 5] or Fig. 5 of the present work) which shows a pronounced dip at the two-photon atomic frequency (thus suggesting that the excitation is of a molecular or quasi-molecular nature). Bajic et al. proposed that the excitation occurred through the two-photon process $3^1\Pi_u \xleftarrow{2h\nu} 1^1\Sigma_u^+$. In addition, for some experimental conditions, the spectrum of the 830 nm emission is much broader than is typical for other atomic parametric processes such as the 840 nm peak. Finally, Bajic et al. argue that they have observed an analogous emission peak in potassium vapor, which they attribute to the $1^3\Sigma_g^+ \to 1^3\Sigma_u^+$ excimer band of the K_2 molecule.

We became interested in the 830 nm emission due to our long term interest in the alkali excimer bands, and in possibilities for producing tunable, near-infrared lasers based upon them. The evidence regarding an excimer as opposed to an atomic parametric explanation for the 830 nm emission seemed inconclusive to us, so we decided to carry out a two-color excitation experiment (suggested by Wang et al. in their paper) to test this hypothesis. If the excimer explanation was correct, we believed the 830 nm emission could be resonantly enhanced through the pumping scheme

$$3^3\Delta_u \xleftarrow{h\nu_2} 1^3\Pi_g \xleftarrow{h\nu_1} 1^3\Sigma_u^+ .$$

Here laser 1 would be tuned near 551.5 nm, which is the wavelength of the well localized $1^3\Pi_g \leftarrow 1^3\Sigma_u^+$ satellite [17], while laser 2 would be tuned near 609.1 nm, which is the wavelength needed to bring the two-photon sum close to the $3S-4D$ energy separation.

However, before we got to the two-color experiment, we obtained new data from a one-laser experiment which we believe unambiguously identifies the 830 nm emission as resulting from an axially phase-matched six-wave mixing process. Processes of this type have been described in detail by Moore et al. in an interesting paper which appeared recently [8]. In axially phase-matched wave-mixing, the photons all propagate collinearly with the pump beam (Fig. 1b). In this case, and for the particular six-wave process which is of interest here (Fig. 2), the energy and momentum conservation equations become:

$$\omega_1 + \omega_2 = 2\omega_L - (\omega_{4D\to 4P} + \omega_{4P\to 3D}) \quad (3)$$

and

$$|\mathbf{k}_1| + |\mathbf{k}_2| = 2|\mathbf{k}_L| - (|\mathbf{k}_{4D\to 4P}| + |\mathbf{k}_{4P\to 3D}|). \quad (4)$$

Here ω_1 and ω_2 (and the corresponding wave vectors) refer to the two axially phased-matched waves produced in the vapor which satisfy (3) and (4). In the following sections of this article, we present our data on the 830 nm, and other related coherent emissions. In particular, we have observed both ω_1 and ω_2 for the process described by (3) and (4), as well as for an analogous process involving the Na $4S$ (as opposed to the $3D$) state (Fig. 2). Section 1 of this paper describes our experimental set-up. Section 2 presents our experimental results which include emission and excitation

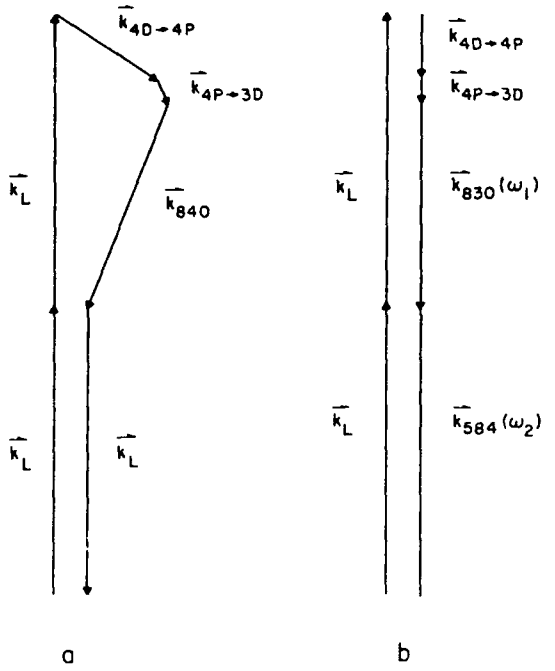

Fig. 1a, b. Phase matching diagrams for six-wave mixing processes occurring in sodium vapor pumped at the $3S\to4D$ two-photon transition wavelength. **a** Angle phase-matched process described by (1) and (2). The angles have been greatly exaggerated for clarity. **b** Axially phase-matched process described by (3) and (4)

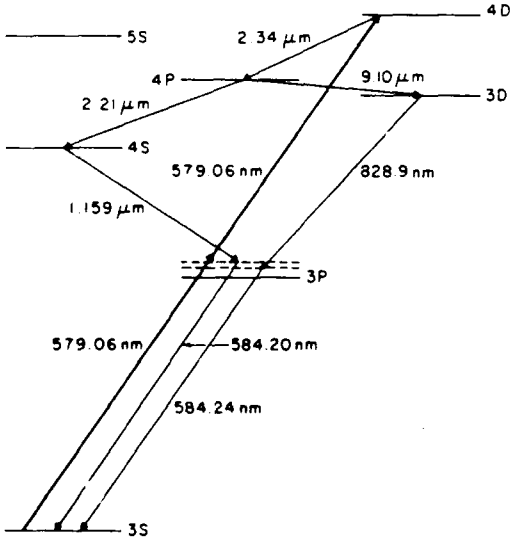

Fig. 2. Partial energy level diagram of sodium showing the two axially phase-matched six-wave mixing processes studied in the present work. In this example, the pump laser (which is indicated by the heavy lines) is tuned to 579.06 nm (with respect to air), which is near to the $3S\to4D$ two-photon transition. The other wavelengths given in the figure correspond to this pump wavelength. The separation of the two virtual levels above the $3P$ state is greatly exaggerated. Energies are taken from [18]

scans, laser power dependences, angle dependences of the emission, etc. Section 3 contains theoretical calculations of the wavelengths of the observed axially phase-matched six-wave mixing processes in both pure sodium and in mixed sodium-potassium vapor. Finally, Sect. 4 presents our conclusions and a summary.

1. The Experiment

Figure 3 shows a diagram of the experimental set-up. A frequency-doubled Nd:YAG laser (Quanta Ray DCR 11) with an output power of ~100 mJ was used to pump a commercial Littman-type dye laser (Lumonics HyperDye 300). The dye laser was operated with Rhodamine 6G dye and produced output powers of ~6 mJ in a pulse of ~6 ns duration. The linewidth was ~0.1 cm^{-1}.

The dye laser was tuned near 579 nm (i.e. close to the sodium $3S\to4D$ two-photon transition wavelength), and was used to excite sodium vapor contained in a heat-pipe oven. Two ovens were used for the present experiment. The first is a linear heat-pipe containing pure sodium metal, while the second is a four-armed cross containing sodium-potassium mixtures. Both ovens were typically operated at ~770 K, which corresponds to a sodium vapor pressure of ~5.5 mbar. In the pure sodium pipe, the argon buffer gas pressure was ~16 mbar, but was raised to 33–47 mbar in the Na–K mixture.

The laser beam was directed through the heat-pipe oven and onto the entrance slits of a 0.75 m monochromator (Spex model 1702). Coherent and stimulated emissions emerging from the alkali vapor along the pump laser axis were then also aligned to the monochromator slits. Color glass and interference filters were used in front of the monochromator to eliminate second and higher order grating effects, and

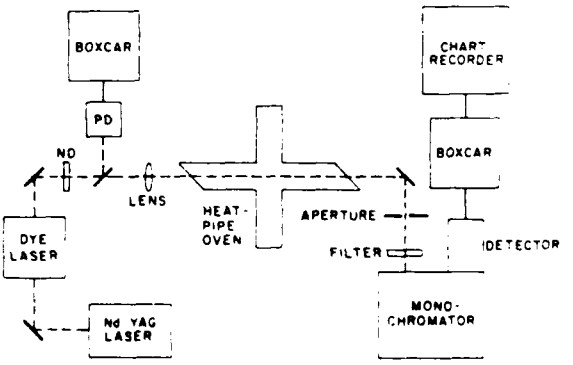

Fig. 3. Experimental set-up. ND and PD represent neutral density filter and photodiode, respectively

to filter out the strong pump laser light before it reached the detector. An aperture was placed along the beam path approximately 0.7 m from the exit window. This was used to study the angular divergences of the various emissions of interest. Neutral density filters were used before the heat-pipe to control the pump laser intensity which was monitored continuously with a photodiode. A lens was used to focus the laser to a diameter of ~0.5–1.0 mm in the center of the oven.

The dispersed emission spectra exiting the monochromator were detected by either an S-1 or S-20 photomultiplier (Hamamatsu R 1767 or R 1387, respectively), whose output was sent to a gated boxcar-averager (Stanford Research SR 250). The boxcar signals were recorded on a strip-chart recorder or laboratory computer.

Typically, data were taken in two modes. For emission spectra, we set the laser to a particular frequency and scanned the monochromator. Excitation spectra were obtained by setting the monochromator transmission wavelength and scanning the laser wavelength. Depending on the detection efficiency for the wavelength of interest and the proximity of that wavelength to the pump laser line, monochromator slits were adjusted to give a resolution between 0.2 and 0.8 nm.

2. Experimental Results

In Fig. 4 we show forward emission spectra for the various wavelength ranges of interest. Details of the emission spectra depend on the exact laser wavelength, although the main features are the same for all excitation wavelengths near the $3S \rightarrow 4D$ two-photon transition. Here, the pump laser wavelength was set to 578.76 nm. Part b) of the figure shows the 830 nm emission along with the unresolved $3D \rightarrow 3P$ atomic ASE and other processes near 820 nm and the angle phase-matched wave-mixing signal at 840 nm. Part c) shows the analogous region near the $4S \rightarrow 3P$ transition wavelength. The peaks near 1.14 μm correspond to the $4S \rightarrow 3P$ fine-structure doublet, while that at 1.18 μm is the analog of the 840 nm emission which has previously been reported by Hartig [2]. Clearly, the 1.16 μm peak appears to be the analog of the 830 nm axially phase-matched emission. This conclusion will be justified in the next section where we will calculate the expected positions of the various emission lines which result from the axially phase-matched six-wave processes. The observed positions of the 830 nm and 1.16 μm peaks are compared in Table 1 with values calculated as described in the next section. According to theory, the 1.16 μm and 830 nm emission should be coupled to emission at a wavelength which is roughly halfway between the wavelengths of the laser and the $3P \rightarrow 3S$ atomic line (Fig. 2). Figure 4a shows an emission scan taken in the region around 584 nm. A clear peak is observed close to the predicted position (see

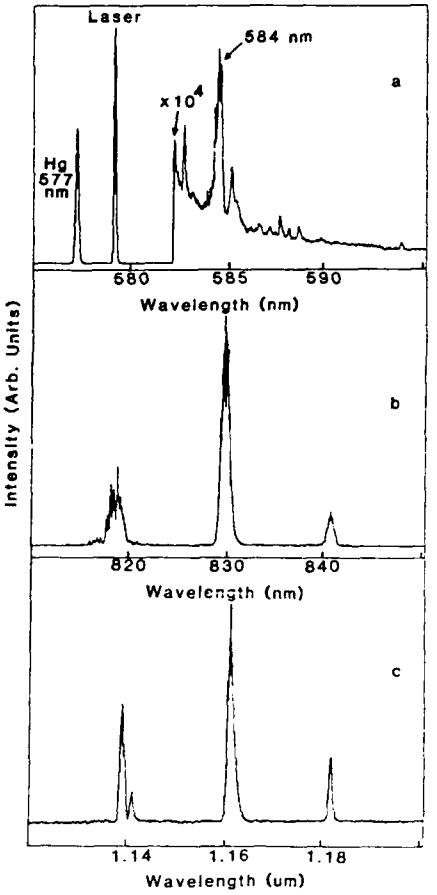

Fig. 4a–c. Forward emissions scans obtained in pure sodium vapor with the laser tuned to 578.76 nm, which is near the sodium $3S \rightarrow 4D$ two-photon transition. Part **a** shows the region between 570 and 595 nm, which includes a mercury calibration line, the laser line, and the axial emission at 584 nm. The laser line was attenuated by $\sim 10^4$. Monochromator slits were adjusted to 30 μm (yielding a resolution of ~0.2 nm) in order to distinguish the 584 nm emission from leakage through the monochromator of the very strong laser line (which is responsible for the background near 584 nm). We demonstrated that the other small peaks near the 584 nm line are grating ghosts, but that the 584 nm peak itself is not. Part **b** shows the region from 810–850 nm which includes the $3D \rightarrow 3P$ ASE and wave-mixing signals near 819 nm, the axially phase-matched emission near 830 nm, and the angle phase-matched emission near 840 nm. Part **c** contains the region between 1.12 and 1.20 μm, which shows the analogous $4S$ state channel. The monochromator slits were 300 μm in parts **b** and **c**. In all parts, the heat pipe oven temperature and buffer gas pressure were ~510 C and ~16 mbar, respectively. The laser energy was ~1 mJ in a 6 ns pulse.

Table 1. Observed and calculated wavelengths for axially phase-matched six-wave mixing processes occurring in pure sodium vapor excited at the $3S \rightarrow 4D$ two-photon transition. All wavelengths are taken in air, and are expressed in nm. Experimental uncertainties are given in parentheses

		3D channel		4S channel	
	λ_{pump}	$\lambda(\omega_1)$	$\lambda(\omega_2)$	$\lambda(\omega_1)$	$\lambda(\omega_2)$
Exp.	578.66 (±0.05)	–	829.66 (±0.3)	–	1160.55 (±0.5)
Calc.		584.05	829.24	584.00	1159.69
Exp.	578.76	584.00	829.16	584.00	1160.34
Calc.		584.10	829.15	584.05	1159.48
Exp.	578.86	583.90	829.04	583.90	1160.31
Calc.		584.15	829.05	584.10	1159.30
Exp.	579.06	584.26	828.96	584.26	1159.09
Calc.		584.24	828.86	584.20	1158.92

also Table 1). Although this peak is difficult to isolate due to its proximity to the laser line, we were able to demonstrate that the observed peak is not a grating ghost or other artifact. The excitation spectra and power dependences, which will be presented next, support our identification of this 584 nm emission as the final photon in the axially phase-matched six-wave mixing process.

Figure 5 shows the excitation spectra for the 584 nm, 830 nm, and 1.16 μm axially phase-matched six-wave mixing signals. It is important to note that the detailed shapes of the excitation spectra depend critically on the wavelength setting of the monochromator, and on the monochromator slit widths. [Ref. 16, Fig. 5] presents excitation spectra for several different monochromator wavelength settings near 830 nm, which are consistent with our observations. Nevertheless, the strong similarity of the 584 nm, 830 nm, and 1.16 μm excitation spectra is strong evidence that these emissions are closely related. In particular, all show a pronounced dip exactly at the $3S \rightarrow 4D$ two-photon transition wavelength, regardless of the monochromator setting. Figure 6 shows for comparison the excitation spectra of the 820 nm, 830 nm (axially phase-matched six-wave mixing), and 840 nm (angle phase-matched six-wave mixing) signals, as well as those of the analogous lines from the 4S state channel. The 820 nm and 1.14 μm signals consist of both ASE and parametric wave-mixing emissions resulting in

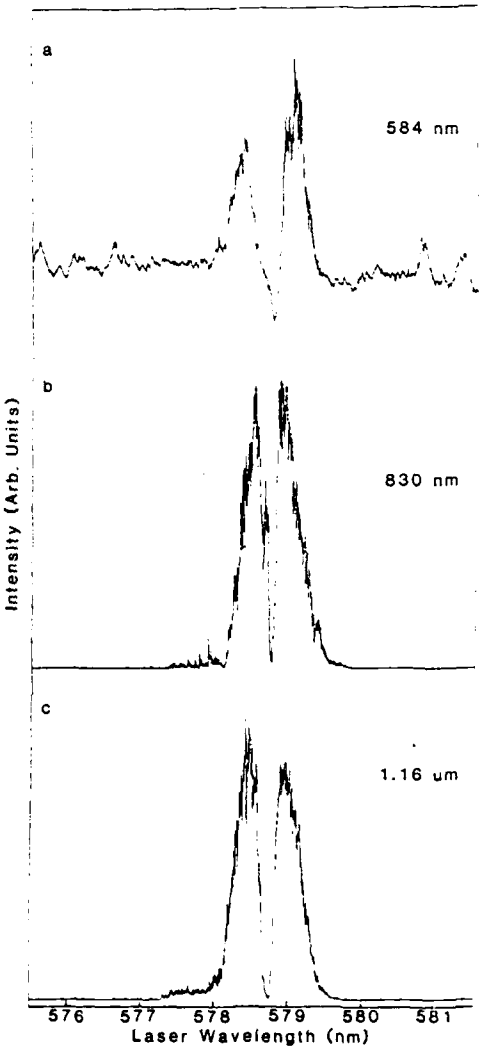

Fig. 5a–c. Laser excitation spectra for axial emission at **a** 584 nm **b** 830 nm and **c** 1.16 μm. Monochromator slits were set to 30 μm for part **a**, and 300 μm for parts **b** and **c**. The oven was operated with pure sodium, and the temperature and pressure were ~550 C and ~16 mbar, respectively. Laser power was ~2 mJ

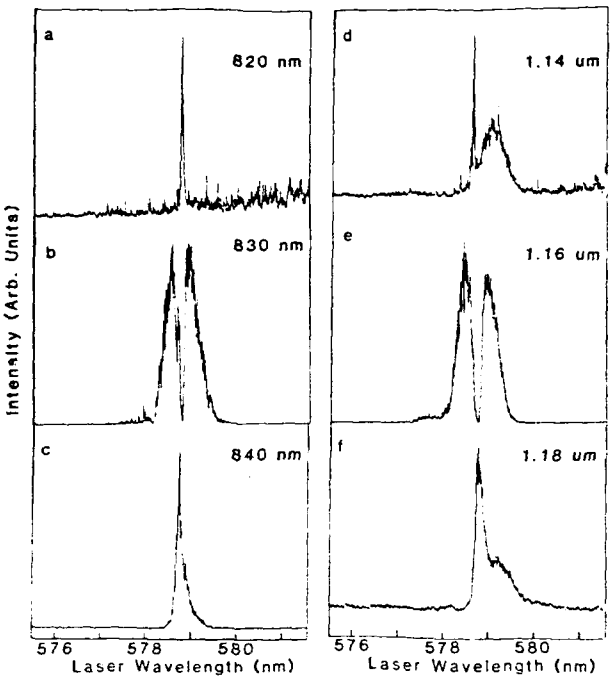

Fig. 6a–c. Laser excitation spectra in pure sodium vapor for processes coupled to the 3*D* states: **a** ASE and wave-mixing at 819 nm, **b** axially phase-matched emission at 830 nm, and **c** angle phase-matched emission at 840 nm. **d**, **e**, and **f** Excitation spectra for analogous processes coupled to the 4*S* state, at 1.14, 1.16, and 1.18 μm, respectively. The oven temperature and buffer gas pressure were ~550 °C and ~16 mbar, respectively. Monochromator slits were 30 μm for part **a**, and 300 μm for parts **b** through **e**. The laser power was ~2 mJ

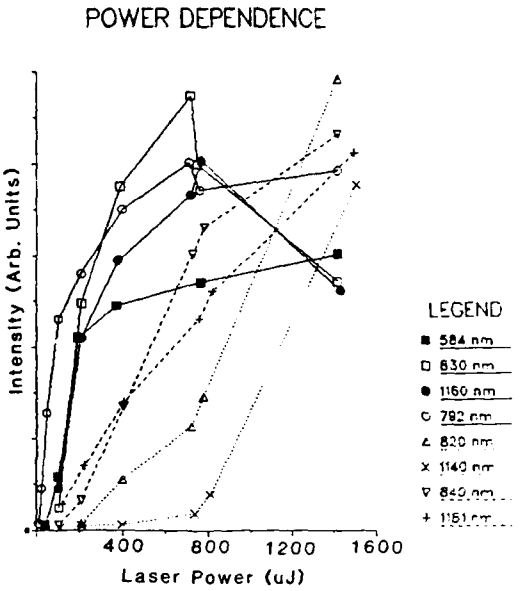

Fig. 7. Dependence of the forward emission intensities on pump laser power for the various processes studied in this work. Dotted curves represent the ASE and wave-mixing signals at 820 nm and 1.14 μm. Dashed curves correspond to angle phase-matched processes at 840 nm and 1.18 μm. Solid lines correspond to the axially phase-matched emissions at 584 nm, 830 nm, and 1.16 μm. The power dependence of stimulated emission on one Na_2 dimer line at 792 nm is also shown as a solid line for comparison. The oven contained pure sodium vapor and was operated at a temperature and buffer gas pressure of ~500 °C and ~17 mbar, respectively. The laser wavelength was 578.70 nm

complicated excitation spectra which depend strongly on the monochromator wavelength and slitwidth. In particular, the 820 nm signal shows only a sharp spike on resonance because of the narrow slits used in part a) of Fig. 6 (which were needed to discriminate against unwanted molecular emissions). With wider slits at lower pressures, the 820 nm excitation spectrum shows a broad hump to the red of the narrow spike, and is thus quite similar to the 1.14 μm excitation spectrum presented in Fig. 6d. We did not investigate these features any further in the present work, since these emissions have been well studied previously [8]. All of the spectra shown in Fig. 6 change in detail as the monochromator wavelength is varied. However, the purpose of Figs. 5 and 6 is to demonstrate the qualitative similarity of the 584 nm, 830 nm, and 1.16 μm excitation spectra, and to point out their marked differences from those of the ASE and angle phase-matched processes.

Figure 7 presents the dependences of the various observed signals on pump laser power. Again, the similarity of the 584 nm, 830 nm, and 1.16 μm emissions (shown as solid lines in the figure) can be seen. The angle phase-matched signals at 840 nm and 1.18 μm (dashed lines) also behave similarly to each other, as do the signals at 820 nm and 1.14 μm (dotted curves). This figure also includes the power dependence of one Na_2 $1^1\Sigma_u^- \rightarrow 1^1\Sigma_g^+$ band OPL line at 792 nm (also shown as a solid line) for comparison [6, 11].

While Fig. 7 presents the dependences of the various emission peaks on pump laser intensity, Fig. 8 shows the variation of the full 830 nm excitation spectrum with laser intensity. Note that the resonance dip becomes narrower and the overall width of the excitation peak decreases as the laser intensity is reduced. These dependences are not yet well understood, but we will discuss some possible explanations in the next section.

Additional information can be obtained from angle dependent studies similar to those carried out by Moore et al. [8, 9]. Figure 9 shows the emission in the 810–850 nm region with the aperture in Fig. 3 fully opened (Fig. 9a) and partially closed (Fig. 9b). It can be seen that the 830 nm emission is concentrated more

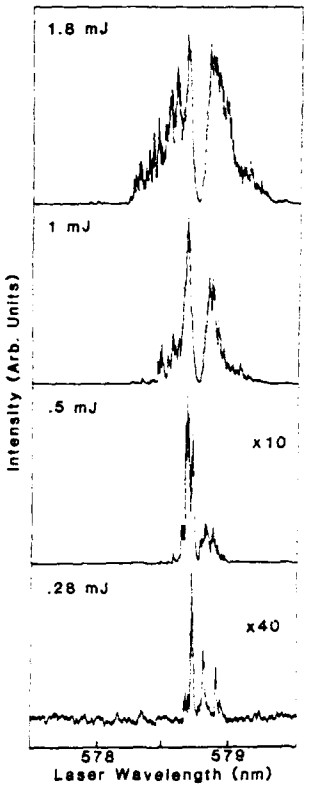

Fig. 8. Laser power dependence of the 830 nm excitation spectrum in pure sodium vapor. Oven temperature and pressure were ~550 C and ~16 mbar, respectively. For these scans, the monochromator wavelength was set to 829.9 nm, and the slits to 100 μm

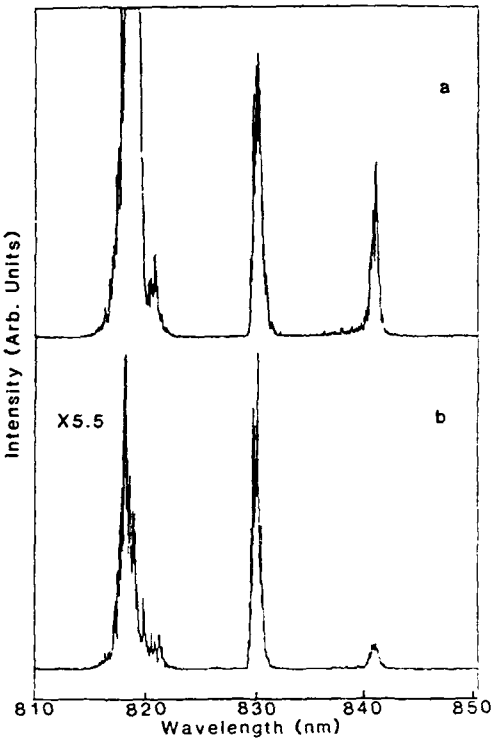

Fig. 9. a Forward emission scan in the 810–850 nm region obtained with the aperture in Fig. 2 fully opened. **b** Same spectrum but with the aperture partially closed. In part **b**, the sensitivity is 5.5 times greater. It can be seen that the intensities of the 820 and 840 nm emissions are reduced much more by the aperture than is the 830 nm emission. Thus these spectra demonstrate that the 830 nm emission is concentrated more closely to the laser axis than are the other two emissions. For these scans, the pure sodium oven temperature and buffer gas pressure were ~510°C and ~16 mbar, respectively. The laser power was ~1.2 mJ. The laser wavelength was 578.66 nm

closely along the pump laser axis than the angle phase-matched emission at 840 nm, or the combination of processes which contribute to the peak at 820 nm.

Finally, we present in Fig. 10 emission spectra taken in mixed sodium-potassium vapor. Note that the 830 nm emission has shifted to ~825 nm in the mixture. The frequency of the 1.16 μm peak (not shown in the figure) also shifts, but by a lesser amount. These observed shifts were the most important clue in leading us toward an axial pase-matched wave-mixing explanation for these processes. The shifts can be predicted from the simple model presented in the next section.

3. Theoretical Treatment

Figure 2 presents an energy level diagram for sodium. In the figure, we show two paths which can be described as axially phase-matched six-wave mixing. In the following, we will show that the channel involving the $3D$ state is responsible for the sodium 830 nm emission.

The theory of axially propogating parametric wave-mixing has been discussed in some detail by Moore et al. [8]. In the case of alkali vapors, it is straight-forward to calculate the wavelengths of the two parametric waves produced in axial four- or six-wave mixing processes. For the particular case of axially phase-matched six-wave mixing produced by two-photon pumping of the sodium $3S \rightarrow 4D$ transition, we can calculate these wavelengths as follows. Using the relation $|\mathbf{k}| = \omega n/c$, where n is the refractive index at the relevant frequency, we can combine (3) and (4) to yield:

$$\omega_1[n(\omega_1)-1]+\omega_2[n(\omega_2)-1] = 2\omega_L[n(\omega_L)-1]-\omega_{4D\rightarrow 4P}[n(\omega_{4D\rightarrow 4P})-1] - \omega_{4P\rightarrow 3D}[n(\omega_{4P\rightarrow 3D})-1] \quad (5)$$

The frequency dependent index of refraction is in general given by $n = \mathrm{Re}\{\varepsilon^{1/2}\}$ with ε the dielectric constant obtained from the expression: [19]

$$\frac{\varepsilon - 1}{\varepsilon + 2} = \frac{4\pi}{3}\frac{e^2}{m}\sum_{i,k} N_i \frac{f_{ik}}{\omega_{ik}^2 - \omega^2 - i\gamma_{ik}\omega}. \tag{6}$$

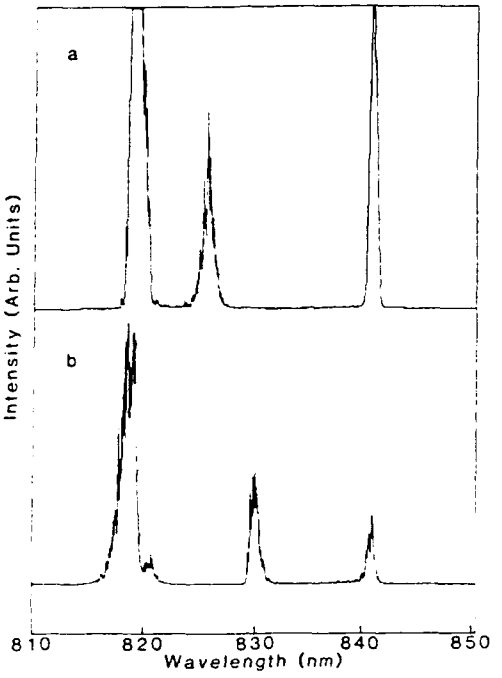

Fig. 10a, b. Emission scans of the 810–850 nm region obtained in **a** a mixed sodium-potassium vapor and **b** in pure sodium, with the laser tuned to 578.66 nm. The oven temperature was ~ 510 C for the pure vapor, and varied with position over the range 370–500 C in the mixed vapor. The buffer gas pressure was ~ 36 and 16 mbar in parts **a** and **b**, respectively. The laser power was ~ 1.2 mJ

Here e and m are the charge and mass of the electron, ω_{ik}, f_{ik}, and γ_{ik} are the frequency, oscillator strength, and half-width (FWHM) of the transition from state i to state k, and we are considering the case of pure sodium vapor. For $n \sim 1$ in a dilute gas, and outside of the resonance linewidths ($|\omega - \omega_{ik}| \gg \gamma_{ik}$), this expression reduces to: [3, 19]

$$n - 1 \approx 2\pi\frac{e^2}{m}\sum_{i,k} N_i \frac{f_{ik}}{\omega_{ik}^2 - \omega^2}. \tag{7}$$

If we now make the assumption that the populations in the excited states are small, we need only consider transitions from the ground state. Thus we can eliminate the sum over i in (7), and replace N_i by the total atom density N. In the case of sodium, the sum over k is just the resonance series of $S \rightarrow P$ transitions. For our situation of six-wave mixing, all photon wavelengths of interest are greater than 578 nm, so the $3S \rightarrow 3P$ transitions at 589.0 and 589.6 nm (which contain over 98% of the total oscillator strength) will dominate the sum. The next largest contribution comes from the $3S \rightarrow 4P$ transitions whose oscillator strengths are a factor of 70 smaller than those of the $3S \rightarrow 3P$ transitions. In addition, the $3S \rightarrow 4P$ transitions lie at higher frequencies ($\lambda \sim 330$ nm), so that their contributions to the right-hand side of (7) are much less than 1%.

Figure 11 shows a qualitative sketch of the function $n - 1$ in the range of interest. Since the two photons near the $4D \rightarrow 4P$ and $4P \rightarrow 3D$ transition wavelengths occur near 2.3 and 9.1 μm, respectively, the last two terms on the right-hand side of (5) will not contribute significantly. In addition, the contribution from the term on the left-hand side involving ω_2 (which will turn out to be in the vicinity of the $3D \rightarrow 3P$ transition at 820 nm), is also very small. Thus, we are left with the simple equation:

$$\omega_1[n(\omega_1) - 1] = 2\omega_L[n(\omega_L) - 1]. \tag{8}$$

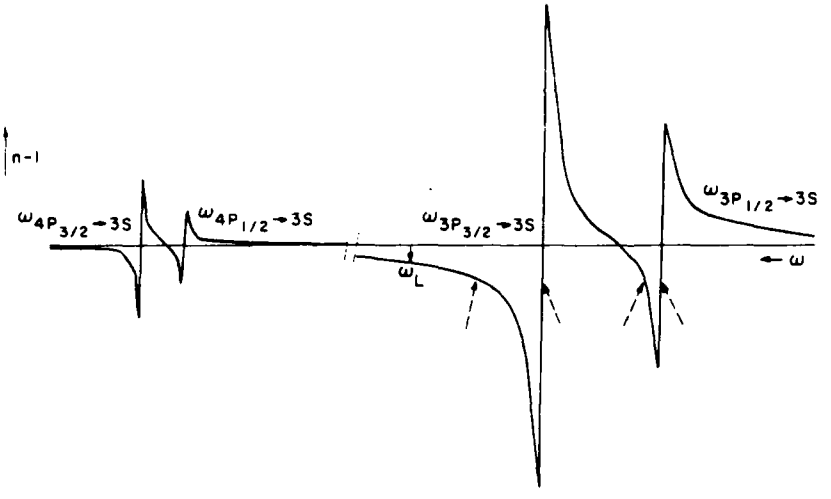

Fig. 11. Qualitative sketch of the function $n - 1$ in the regions around the sodium $3S \rightarrow 3P$ and $3S \rightarrow 4P$ transitions. The laser frequency ω_L is marked by a solid vertical arrow in the figure. The four dashed arrows represent the four points which satisfy (8) for axial phase-matching. The leftmost of the four dashed arrows is the phase-matching point at 584 nm which is also responsible for the 830 nm and 1.16 μm emissions. The figure is not drawn to scale

ω_L is marked in Fig. 11 by the solid arrow. The dashed arrows mark the four points which satisfy (8) for axial phase-matching (see also [9]). Note that two of these points occur very close to the line-centers of the $3P \rightarrow 3S$ fine-structure components. As explained in [8], these are regions of strong absorption, which tends to reduce axial wave-mixing at these frequencies. The third point, between the two $3P \rightarrow 3S$ fine-structure transition frequencies, is responsible for the axially phase-matched six-wave mixing reported in [8]. Since ω_2 is given fairly closely by:

$$\omega_2 = \omega_{3D \rightarrow 3S} - \omega_1 , \tag{9}$$

this process also produces a signal at a frequency between the $3D \rightarrow 3P$ fine-structure components, which can be seen in [Ref. 8, Fig. 5].

It is the final point satisfying (8), marked by the left-most dashed arrow in Fig. 11, that is responsible for the sodium 830 nm emission. Although direct computation from (5) and (7) allows an accurate prediction of the frequencies ω_1 and ω_2 associated with this point, these frequencies can be calculated approximately from the following simple argument. Since the frequency range in the region of interest is not large, the points satisfying (8) correspond very nearly to the points where $n-1$ is simply twice $n(\omega_L)-1$. In addition, for frequency detunings that are large compared to the fine structure splitting, but not so large that $\omega \approx \omega_{3P \rightarrow 3S}$ is not a reasonable approximation, the dispersion is roughly a linear function of frequency [i.e. the frequency denominator of (7) can be approximated as

$$\omega_{3P \rightarrow 3S}^2 - \omega^2 \approx 2\omega_{3P \rightarrow 3S}(\omega_{3P \rightarrow 3S} - \omega)] .$$

Therefore, it can be seen that (8) will be satisfied by one point that is close to midway between the laser and the atomic line frequencies. Since the $3D \rightarrow 3P$ atomic lines at 819 nm are the complement of the $3P \rightarrow 3S$ atomic lines, and the 840 nm emission is the complement of the laser wavelength (i.e. $\omega_{3D \rightarrow 3P} = \omega_{3D \rightarrow 3S} - \omega_{3P \rightarrow 3S}$ and $\omega_{840} = \omega_{3D \rightarrow 3S} - \omega_L$), it can be seen that an axially phase-matched six-wave mixing photon should be emitted with its wavelength almost midway between those of the 840 and 819 nm emissions.

Use of (5) and (7) including all six photons and resonance terms through the $3S \rightarrow 5P$ doublet allows accurate predictions of the axial six-wave mixing photon wavelengths for a given laser wavelength. Wavelengths calculated in this manner are compared to observed wavelengths in Table 1 for the case of pure sodium vapor and for several laser frequencies. For these calculations, energies and oscillator strengths were taken from [18]. Note that while ω_1 and ω_2 shift with the pump laser wavelength (for a shift $\Delta\omega_L$ of the pump frequency, we expect $\Delta\omega_1 \equiv \Delta\omega_{584} \approx \Delta\omega_L/2$ and $\Delta\omega_2 \equiv \Delta\omega_{830} \approx -\Delta\omega_L/2$), it is a different dependence than that predicted for the angle phase-matched 840 nm emission ($\Delta\omega_{840} \approx -\Delta\omega_L$) which has recently been demonstrated experimentally by Wang et al. [6] and Yih et al. [20]. Note also that the axially phase-matched emission frequencies ω_1 and ω_2 are independent of the sodium atom density which cancels out of each term in (5).

In addition, it is clear from Fig. 2 that a similar process should occur under the same conditions for the cascade sequence passing through the $4S$ (rather than the $3D$) state. This latter process is responsible for the 1.16 μm emission. Predicted and observed wavelengths for this process are also presented in Table 1.

Finally, we present what is perhaps the most convincing argument in favor of the axially phase-matched six-wave mixing explanation for the 830 nm emission. According to theory, we expect to observe predictable shifts in wavelength of the various emission peaks as we change the refractive index of the vapor. In particular, when we consider the case of these processes occurring in mixed sodium-potassium vapor, we must include the effects of the potassium on the index of refraction. In this case, and again assuming that only the atomic ground states are significantly populated, (7) becomes:

$$n - 1 \approx 2\pi \frac{e^2}{m}\left[N_{Na} \sum_k \frac{f_{ik}}{\omega_{ik}^2 - \omega^2} + N_K \sum_m \frac{f_{jm}}{\omega_{jm}^2 - \omega^2} \right]. \tag{10}$$

Here, states i and j represent the sodium and potassium ground states, respectively. Since the potassium resonance lines lie at 765 and 770 nm, the second term on the right-hand side of (10) contributes significantly to the dispersion in the vicinity of 830 nm. This pushes the 830 nm emission to shorter wavelengths, with the actual value being determined by the relative sodium to potassium density ratio. Qualitatively, this is what we observe in Fig. 10. Note that the analogous emission near 1.16 μm (involving the $4S$ state cascade channel) is not shifted as much in frequency, since the potassium contributes less to the dispersion of either ω_1 or ω_2 in this case.

It is difficult to determine the sodium-potassium density ratio in the heat-pipe oven, because the two species tend to separate [21]. However, we know that an upper limit to N_K/N_{Na} is ~ 10 which is obtained from vapor pressure curves [22], and a lower limit is clearly zero for complete separation. In Table 2 we present values of the observed positions of the 830 nm and 1.16 μm peaks for two pump wavelengths. These can be compared to tabulated values of the peak positions calculated from (5) and (10) using various values of the ratio N_K/N_{Na}. It can be seen that the shifts agree fairly well with those predicted for $N_K/N_{Na} \sim 3$.

Table 2. Measured and calculated positions of axially phase-matched six-wave mixing signals in mixed sodium-potassium vapors for two pump laser wavelengths. The calculated values are obtained from (5) and (10) using several values for the ratio N_K/N_{Na}. These ratios are given in the last column. Wavelengths are in air, and are given in nm. The experimental conditions were as in Fig. 10, and the experimental uncertainties are given in parentheses

λ_{pump}	3D channel		4S channel		N_K/N_{Na}
	$\lambda(\omega_1)$	$\lambda(\omega_2)$	$\lambda(\omega_1)$	$\lambda(\omega_2)$	
Experimental					
578.66 (±0.05)	–	825.26 (±0.3)	–	1156.75 (±0.5)	
578.86 (±0.05)	–	824.84 (±0.3)	–	1156.31 (±0.5)	
Theoretical					
578.66	584.05	829.24	584.00	1159.69	0
	584.53	828.28	584.22	1158.84	0.5
	584.93	827.48	584.42	1158.06	1.0
	585.56	826.21	584.76	1156.69	2.0
	586.04	825.27	585.07	1155.52	3.0
	586.41	824.54	585.33	1154.50	4.0
	586.70	823.96	585.56	1153.61	5.0
	586.93	823.50	585.76	1152.81	6.0
	587.30	822.79	586.10	1151.49	8.0
	587.55	822.28	586.39	1150.40	10.0
578.86	584.15	829.05	584.10	1159.30	0
	584.61	828.12	584.31	1158.49	0.5
	584.99	827.35	584.50	1157.74	1.0
	585.61	826.12	584.84	1156.43	2.0
	586.08	825.19	585.13	1155.28	3.0
	586.44	824.48	585.38	1154.29	4.0
	586.72	823.92	585.60	1153.42	5.0
	586.96	823.46	585.80	1152.65	6.0
	587.31	822.77	586.14	1151.34	8.0
	587.56	822.27	586.42	1150.28	10.0

This value appears reasonable for the heat-pipe oven. We have also found that variation of the oven temperature and buffer gas pressure can cause the 830 nm peak to move in Na–K mixtures but not in pure sodium. This is because the variation of the mixed-vapor oven operating conditions causes variation in N_K/N_{Na} in the central part of the oven. Clearly, this cannot occur in the pure vapor.

Because of its simple dependence on N_K/N_{Na}, it is possible that the shift of the 830 nm emission can be used as a convenient measure of this ratio in the central region of sodium-potassium heat-pipe ovens. This, and analogous processes in other alkali vapors, might prove useful in determining atom density ratios in various experiments involving spectroscopy of heteronuclear molecules, or the study of collisions between dissimilar atoms.

4. Conclusions and Summary

In the preceding sections, we have presented experimental and theoretical evidence which unambiguously identifies the 830 nm emission, observed under two-photon pumping of the Na $3S \rightarrow 4D$ transition, as an axially phase-matched six-wave mixing process. This evidence includes the observation of coherent emission at 584 nm, which is coupled to the 830 nm emission in the wave-mixing process, and a related emission peak at 1.16 μm, which is due to an analogous six-wave mixing process involving the $4S$ intermediate state. The common nature of these three emissions is documented by the similarity of their excitation spectra and their dependences on laser power. The axial nature of this six-wave mixing process has been demonstrated by angle dependent studies carried out with an aperture. In addition, we have observed dramatic shifts in the wavelengths of these axially phase-matched emissions when we changed the refractive index of the vapor by mixing potassium with the sodium.

These observations can be easily explained by a simple model of axially phase-matched six-wave mixing similar to that presented recently by Moore et al. [8, 9]. We have used this model to predict the wavelengths of the various emissions in pure sodium vapor, and have obtained values which agree with observations to within experimental uncertainties. This

model also qualitatively explains the wavelength shifts observed in sodium-potassium mixtures. The only parameter needed to make these last calculations quantitative is the ratio of the potassium to sodium number densities. In fact, observations of this type may be useful for obtaining atom density ratios in other experiments on mixed alkalis.

Using this simple model, we can also speculate about the origin of the dip in the axially phase-matched six-wave excitation spectra for resonant pumping. When the pumping is well off resonance, the excited state populations remain small, and the indices of refraction are given by (7) with N_i replaced by N and the sum extending over the $3S \rightarrow nP$ resonance series. However, if the laser is tuned onto resonance, this approximation breaks down, and the conditions for axial phase matching are altered considerably. The indices of refraction will change, due to the increase in the number of excited atoms, and to an increase in ionization, and this could disrupt the axial phase-matching process. An alternate explanation of this dip is competition between the 820, 830, and 840 nm emission processes, with the 820 nm processes dominating the resonant excitation case. We believe that another possible explanation, based on a simple depletion of available sodium atoms by two-photon resonant, three-photon ionization, is incorrect, because this would cause a similar dip in the 820 and 840 nm signals which is not observed. We tried to experimentally distinguish between some of these possibilities by studying the pump laser intensity dependence of the 830 nm excitation spectra which is shown in Fig. 8. We thought the resonance dip might be reduced for lower pump power where the excited atom densities are smaller. In fact, the dip does appear to narrow, and the width of the excitation spectrum is reduced as we decrease the laser power. However, we do not believe that any definite conclusions can be reached concerning the resonance dip at this time.

The simple theory presented here only predicts emission wavelengths for a given pump wavelength, and says nothing about intensities. We have not explained the great breadth of the emission spectrum which can occur under certain circumstances (see [Ref. 16, Fig. 4] in particular). We have also not explained the shape and breadth of the excitation spectra other than to mention some possible explanations for the resonance dip. We hope that the present experimental study will stimulate further theoretical work on these processes which might address the questions of excitation lineshapes, and competition between the processes of ASE, axial phase-matched wave-mixing, and angle phase-matched wave-mixing which can occur simultaneously in this system.

Finally, we believe that the evidence presented above makes it impossible to give further support to explanations of the 830 nm emission as Na_2 bound-free $1^3\Sigma_g^+ \rightarrow 1^3\Sigma_u^+$ excimer emission, that have appeared recently in the literature [13, 16]. Such explanations cannot explain the presence of a correlated photon at 584 nm, or the analogous emission at 1.16 μm. In addition, excimer explanations cannot account for the observed shift of the 830 nm emission in Na–K mixtures, both because the shift can be made continuous with variation of the sodium/potassium ratio, and because the analogous excimer bands of the NaK and K_2 molecules occur at wavelengths beyond 1 μm.

Acknowledgements. We are grateful to M. A. Moore, W. R. Garrett, R. N. Compton, and S. J. Bajic for many helpful discussions and for providing us with their results prior to publication. This work was supported by the Army Research Office under grant DAALO3-86-K-0161 and the National Science Foundation under grant PHY-8451279.

References

1. D. Cotter, D.C. Hanna, W.H.W. Tuttlebee, M.A. Yuratich: Opt. Commun. **22**, 190 (1977)
2. W. Hartig: Appl. Phys. **15**, 427 (1978)
3. P.-L. Zhang, Y.-C. Wang, A.L. Schawlow: J. Opt. Soc. Am B **1**, 9 (1984)
4. J. Krasinski, D.J. Gauthier, M.S. Malcuit, R.W. Boyd: Opt Commun. **54**, 241 (1985)
5. S.M. Hamadani, J.A.D. Stockdale, R.N. Compton, M.S Pindzola: Phys. Rev. A **34**, 1938 (1986)
6. Z.G. Wang, H. Schmidt, B. Wellegehausen: Appl. Phys. B **44**, 41 (1987)
7. M.A. Moore W.R. Garrett, M.G. Payne: Opt. Commun. **68**, 310 (1988)
8. M.A. Moore, W.R. Garrett, M.G. Payne: Phys. Rev. A [redacted]
9. M.A. Moore: Ph.D. dissertation, University of Tennessee (unpublished)
10. B. Wellegehausen: IEEE J. QE-**15**, 1108 (1979)
11. K.K. Verma, J.T. Bahns, A.R. Rajaei-Rizi, W.C. Stwalley: J Chem. Phys. **78**, 3599 (1983)
12. J.T. Bahns, K.K. Verma, A.R. Rajaei-Rizi, W.C. Stwalley: Appl. Phys. Lett. **42**, 336 (1983)
13. S.G. Dinev, I.G. Koprinkov, I.L. Stefanov: Opt. Commun. **52**, 199 (1984)
14. D.D. Konowalow, P.S. Julienne: J. Chem. Phys. **72**, 5815 (1980)
15. J. Huennekens, S. Schaefer, M. Ligare, W. Happer: J. Chem. Phys. **80**, 4794 (1984)
16. S.J. Bajic, R.N. Compton, J.A.D. Stockdale, D.D. Konowalow: J. Chem. Phys. **89**, 7056 (1988)
17. D. Veza, J. Rukavina, M. Movre, V. Vujnovic, G. Pichler: Opt. Commun. **34**, 77 (1980)
18. W.L. Wiese, M W. Smith, B.M. Miles: *Atomic Transition Probabilities*, Vol. II. NSRDS-NBS 22 (1969)
19. M. Born, E. Wolf: *Principles of Optics* (Pergamon, Oxford 1980) pp. 87–94
20. T.S. Yih, H.H. Wu, Y.C. Hsu, K.C. Lin: In *Advances in Laser Science* **III**, ed. by A.C. Tam, J.L. Gole, and W.C. Stwalley (American Institute of Physics, New York 1988) pp. 161–163
21. M.M. Hessel, P. Jankowski: J. Appl. Phys. **43** 209 (1972)
22. A.N. Nesmeyanov: *Vapor Pressure of the Elements* (Academic, New York 1963)

Appendix 7

PHYSICAL REVIEW A VOLUME 38, NUMBER 9 NOVEMBER 1, 1988

Excitation-transfer collisions in cesium vapor: $Cs(5D_{5/2})+Cs(6S_{1/2})\rightarrow Cs(5D_{3/2})+Cs(6S_{1/2})$

B. Keramati, M. Masters, and J. Huennekens
Department of Physics, Lehigh University, Bethlehem, Pennsylvania 18015
(Received 25 March 1988)

We report an experimental investigation of the excitation-transfer collision $Cs(5D_{5/2})+Cs(6S)\rightarrow CS(5D_{3/2})+Cs(6S)$. The upper $5D_{5/2}$ state was excited by a cw dye laser tuned to the one-photon, quadrupole-allowed $6S\rightarrow 5D_{5/2}$ transition. Since the direct $5D\rightarrow 6P$ fluorescence could not be detected with our apparatus, we monitored instead the cascade $6P\rightarrow 6S$ fluorescence. The ratio of $6P_{1/2}$ to $6P_{3/2}$ fluorescence contains information on the collisional mixing that takes place in the $5D$ levels but also includes a significant contribution from mixing in the $6P$ levels. This latter contribution could effectively be subtracted out using the results of a second experiment in which a tunable cw diode laser was used to pump the $6P_{3/2}$ state, and the same fluorescence ratio monitored. The $5D$ mixing cross section we obtain, 70 Å^2, is significantly larger than previous indirect determinations.

I. INTRODUCTION

Over the years there has been extensive investigation of transfer of population among alkali atom fine-structure levels in collisions with ground-state alkalis,[1-10] noble-gas atoms,[2,6-7,9-16] and diatomic molecules.[6-7,9-10,14] A complete review of theoretical and experimental work in this area up until 1975 can be found in Ref. 17. These fine-structure-level-changing collisions are important since they are among the simplest atomic-energy-transfer processes and thus represent a fundamental test for theories of atomic interactions. Recently it has also been shown that data on collisions involving transfer among fine-structure levels can provide direct information on interatomic potential curves.[18-20]

From an experimental point of view alkalis have been studied because excited states are easily accessed using tunable dye lasers. Fine-structure-level-changing collisions in various P states have been studied using direct one-photon excitation from the ground state,[3,4,11,13-16] while many D levels have also been investigated by applying two-photon or two-step excitation techniques.[1,2,5-9,12] Such studies, particularly in cesium, have allowed testing of theoretical arguments concerning the scaling of cross sections with effective principal quantum number n^*.

In the present work we report an experimental determination of the thermally averaged rate coefficient for the excitation transfer process

$$Cs(5D_{5/2})+Cs(6S_{1/2})\rightarrow Cs(5D_{3/2})+Cs(6S_{1/2}) . \quad (1)$$

This process has not been directly studied until now because of the long wavelengths involved in both the excitation and detection stages (see Fig. 1). We sidestepped these difficulties by exciting the $5D$ levels via one-photon electric quadrupole transitions and detecting $6P\rightarrow 6S$ cascade fluorescence. Details of these techniques and the derivation of the rate coefficient from the fluorescence signals are presented in Secs. II–IV. Since $5D$ is the lowest-lying D state in cesium, measurement of this fine-structure-level-changing cross section completes this sequence at the low end, and therefore provides the most severe test for the n^* scaling laws. For higher D states in rubidium and cesium it was found that the fine-structure-level-changing cross section roughly scales with the geometric cross section, which was derived from a Rydberg model. For cesium $5D$, $n^*=2.55$, so core effects will presumably be significant.

Additionally, there has been some controversy over the cesium $5D$ fine-structure-level-changing cross section due to disagreement between two very indirect determinations.[21,22] The work of Wu and Huennekens yielded an anomalously low apparent upper limit on the $5D$ level mixing rate coefficient of 10^{-11} cm^3 s^{-1} as a by-product of an experiment studying predissociation of cesium molecules.[21] At about the same time Davanloo *et al.*[22] obtained an apparently conflicting $5D$ mixing rate coefficient of 6.2×10^{-11} cm^3 s^{-1} with error bars of 60%.

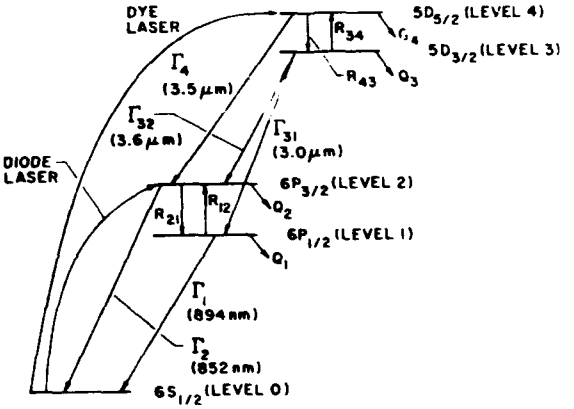

FIG. 1. Partial energy-level diagram of cesium (relative energies not to scale) showing the collisional and radiative processes considered in this work. In the figure the R's represent fine-structure mixing rates, the Q's are collisional quenching rates, and the Γ's are radiative rates. Radiative transitions are also labeled by the corresponding wavelengths.

This result was also a by-product of a photodissociation study of cesium dimers and must also be considered an indirect measurement. The mixing rate coefficient we report here, 2.6×10^{-10} cm^{3}s^{-1}, is actually larger than the Davanloo *et al.* result. In addition, we see no evidence for the very high $5D$ quenching rate coefficient (1.7×10^{-10} cm^{3}s^{-1}) which they also required to fit their data. We still do not fully understand these apparent discrepancies which will be discussed further in Sec. V.

II. EXPERIMENT

Figure 2 shows a schematic diagram of the experimental setup. Pure cesium (no buffer gas) was contained in a 2.54-cm-diameter cylindrical cell made of aluminosilicate glass. The cell was heated to 125–225 °C in a glass oven using nichrome heaters. The cell temperature was monitored by a thermocouple.

Due to the low energy of the cesium $5D$ states, they could not be pumped with the available lasers using either two-photon or two-step excitation. Instead, a tunable cw dye laser, using LDS 722 dye and pumped by 3–5 W all-lines from an argon-ion laser, was used to selectively excite the $5D_J$ levels directly from the ground state via one-photon, dipole-forbidden but electric quadrupole-allowed transitions (see Fig. 1).

Since the $5D$ levels radiate at wavelengths greater than 3 μm, which are beyond the limits of our detectors and the transmission cutoff of our glass cells, we chose to monitor the $5D$ level mixing by observing the cascade $(6P_{1/2}\rightarrow6S)$-to-$(6P_{3/2}\rightarrow6S)$ fluorescence ratio. However, since this ratio contains a contribution from mixing in the $6P$ levels, we were required to carry out a second experiment in which we directly excited the $6P_{3/2}$ state. This was done using a diode laser operating near 852 nm and tunable over a few nanometers by varying the diode current and temperature. Due to radiation-trapping effects described in Sec. IV, it was important that the geometry be identical when using the two different lasers. Thus a translating mirror and a set of apertures were used to ensure that the beam paths of the two lasers through the cell were identical. The stripe of fluorescence along the laser-beam axis through the cell was imaged onto the slits of a monochromator. Again due to radiation trapping, the detection geometry plays a role in the $6P_J$ level fluorescence ratios and this point will be discussed in Sec. IV. Light through the monochromator was detected with either an S-1 or an S-20 photomultiplier. The signal was then processed through either a lock-in amplifier or an electrometer and displayed on a chart recorder. When using the diode laser, the contribution from laser scatter to the $6P_{3/2}\rightarrow6S$ signal was determined by cooling the cell and tuning the laser off resonance. Typically this correction was a few percent.

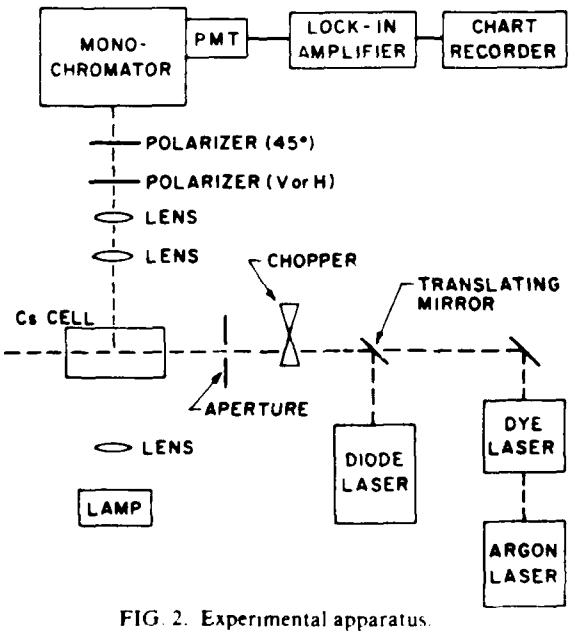

FIG. 2. Experimental apparatus.

A quartz-iodine lamp with known spectral output was used to determine the relative detection efficiency at 852.1 and 894.3 nm using the calibration procedure outlined in Ref. 23. The lamp was also used to determine the cesium-atom density using the absorption-equivalent-width technique. Since the $6P_{3/2}$ fluorescence can be partially polarized, a 45° polarizer (Polaroid HR infrared sheet polarizer) was used in front of the monochromator in conjunction with a second polarizer oriented either vertically or horizontally. This allowed measurement of the two polarization components individually in a manner that was equally sensitive to both.

III. RATE EQUATIONS AND DATA ANALYSIS

The data analysis is based upon a rate-equation approach which includes the relevant collisional and radiative rates shown in Fig. 1. We consider a five-state model including $6S_{1/2}$, $6P_{1/2}$, $6P_{3/2}$, $5D_{3/2}$, and $5D_{5/2}$, which for notational simplicity are labeled states 0, 1, 2, 3, and 4, respectively. For pumping of the $5D_{5/2}$ state we obtain the steady-state rate equations

$$\dot{n}_3=0=-(\Gamma_3+R_{34}+Q_3)n_3+R_{43}n_4\ , \tag{2}$$

$$\dot{n}_2=0=-(\Gamma_2+R_{21}+Q_2)n_2+R_{12}n_1+\Gamma_{32}n_3+\Gamma_4n_4\ , \tag{3}$$

$$\dot{n}_1=0=-(\Gamma_1+R_{12}+Q_1)n_1+R_{21}n_2+\Gamma_{31}n_3\ . \tag{4}$$

Here the n's are the number densities in the different levels, the R's are fine-structure mixing rates, the Q's are quenching rates, and $\Gamma_{31}+\Gamma_{32}\equiv\Gamma_3$ is the total radiative rate out of state 3. Due to radiation trapping, Γ_1 and Γ_2 are effective radiative rates which are much smaller than the $6P\rightarrow6S$ natural radiative rate Γ_N. Note, however, that according to the Holstein theory of radiation trapping, Γ_1 and Γ_2 are independent of density in our range of temperatures.[24,25] The $5D\rightarrow6P$ fluorescence is not trapped since the $6P$ states are only weakly populated by the cw pumping of the forbidden transition. This point is discussed further in Sec. IV. Since we have three equations in four unknown populations, we can solve for all population ratios and thus for the $(6P_{1/2}\rightarrow6S)$-to-$(6P_{3/2}\rightarrow6S)$ fluorescence intensity ratio (which we label I_1/I_2),

$$\left[\frac{I_1}{I_2}\right]_{5D_{5/2}}=\frac{\epsilon_1\lambda_2\Gamma_1 n_1}{\epsilon_2\lambda_1\Gamma_2 n_2}=\frac{\epsilon_1\lambda_2\Gamma_1}{\epsilon_2\lambda_1\Gamma_2}\,\frac{\Gamma_{31}R_{43}(\Gamma_2+R_{21}+Q_2)+R_{21}[\Gamma_4(\Gamma_3+R_{34}+Q_3)+\Gamma_{32}R_{43}]}{(\Gamma_1+R_{12}+Q_1)[\Gamma_4(\Gamma_3+R_{34}+Q_3)+\Gamma_{32}R_{43}]+\Gamma_{31}R_{43}R_{12}}\ . \tag{5}$$

Here λ_1 and λ_2 are the transition wavelengths needed to convert from photons/sec to energy/sec, and ϵ_1/ϵ_2 is the measured relative detection system efficiency at the two wavelengths. The subscript $5D_{5/2}$ on I_1/I_2 reminds us of the particular pumping scheme.

We will argue in Sec. IV that the quenching rates can be ignored compared to the fine-structure mixing rates, so that after some algebra we can write

$$\left[\frac{I_1}{I_2}\right]^{\text{no quenching}}_{5D_{5/2}}=\frac{\epsilon_1\lambda_2}{\epsilon_2\lambda_1}\,\frac{(\Gamma_4\alpha_2+\Gamma_3)(R_{43}/\Gamma_4)(R_{21}/\Gamma_2)+\Gamma_{31}(R_{43}/\Gamma_4)+\Gamma_3(R_{21}/\Gamma_2)}{(\Gamma_3+(\Gamma_4\alpha_2+\Gamma_{32})(R_{43}/\Gamma_4)+(\Gamma_2/\Gamma_1)(R_{21}/\Gamma_2)\{\Gamma_3\alpha_1[1+(R_{43}/\Gamma_4)]+\Gamma_4\alpha_1\alpha_2(R_{43}/\Gamma_4)\}}\ . \tag{6}$$

Here

$$\alpha_1\equiv R_{12}/R_{21}=(g_2/g_1)e^{-(E_2-E_1)/kT}$$

and

$$\alpha_2\equiv R_{34}/R_{43}=(g_4/g_3)e^{-(E_4-E_3)/kT}$$

from the principle of detailed balance.

The situation in the diode-laser case is complicated by the fundamental difference between Rayleigh scatter and true fluorescence when the laser is tuned slightly off resonance. In fact, the diode laser is always off resonance because its low power (~ 8 mW) is not sufficient to burn through the vapor at line center. The complication arises because the Rayleigh scatter occurs at the laser frequency, where it is not as severely trapped as the collisionally redistributed fluorescence. Thus the Rayleigh component is characterized by one radiative rate, Γ_R, while the fluorescence is characterized by Γ_2. In general $\Gamma_2<\Gamma_R<\Gamma_N$. However, the $6P_{3/2}\rightarrow 6S$ signal with diode-laser pumping is always the sum of the Rayleigh and fluorescence components since they cannot be resolved by our monochromator. To properly account for the different effective radiative rates, we introduce rate equations based on Fig. 3,

$$\dot{n}_2=0=\Gamma_c n_R+R_{12}n_1-(\Gamma_2+R_{21}+Q_2)n_2\ , \tag{7}$$

$$\dot{n}_1=0=R_{21}(n_R+n_2)-(\Gamma_1+R_{12}+Q_1)n_1\ . \tag{8}$$

Here the laser is assumed to populate a virtual level R, which can radiate at a rate Γ_R (Rayleigh scatter) or collisionally transfer population to state 1 or state 2. The collisional rate to state 1 is R_{21} (the state $2\rightarrow$ state 1 mixing rate), while the rate to state 2 is Γ_c, the collisional redistribution or line-broadening rate. This virtual-level model ignores coherences created between states 0 and 2 by the laser, but a correct dressed-level treatment (see Ref. 26) yields the same results as this intuitive model and demonstrates that the collisional-rate assignments used here are correct.

It can be shown from Eqs. (7) and (8) that the measured quantity $I_1/(I_2+I_R)$ is given by

$$\left[\frac{I_1}{I_2+I_R}\right]_{6P_{3/2}}=\frac{\epsilon_1\lambda_2}{\epsilon_2\lambda_1}\,\frac{\Gamma_1R_{21}(\Gamma_c+\Gamma_2+R_{21}+Q_2)}{\Gamma_2[\Gamma_c(\Gamma_1+R_{12}+Q_1)+R_{12}R_{21}]+\Gamma_R[R_{12}(\Gamma_2+Q_2)+(\Gamma_1+Q_1)(\Gamma_2+R_{21}+Q_2)]}\ . \tag{9}$$

Since $\Gamma_c\gg R_{21}$ always (collisional dephasing cross sections are always much larger than those of any other collisional process), we can derive the following equation valid in the limit of no quenching:

$$\left[\frac{I_1}{I_2+I_R}\right]^{\text{no quenching}}_{6P_{3/2}}=\frac{\epsilon_1\lambda_2}{\epsilon_2\lambda_1}\,\frac{(R_{21}/\Gamma_2)(1+\Gamma_2/\Gamma_c)}{1+\alpha_1(\Gamma_2/\Gamma_1)(R_{21}/\Gamma_2)+(\Gamma_R/\Gamma_c)\{1+(R_{21}/\Gamma_2)[1+\alpha_1(\Gamma_2/\Gamma_1)]\}}\ . \tag{10}$$

Equations (6) and (10) are the basic expressions used to analyze our data. However, it is instructive to look at the low-density limits of these expressions where collisional rates can be neglected compared to radiative rates (i.e., $\Gamma_1\gg R_{12}$, $\Gamma_2\gg R_{21}$, $\Gamma_3\gg R_{34}$, $\Gamma_4\gg R_{43}$),

$$\left[\frac{I_1}{I_2}\right]^{\text{low density}}_{5D_{5/2}}=\frac{\epsilon_1\lambda_2}{\epsilon_2\lambda_1}\left[\frac{R_{21}}{\Gamma_2}+\frac{\Gamma_{31}}{\Gamma_3}\,\frac{R_{43}}{\Gamma_4}\right], \tag{11}$$

$$\left[\frac{I_1}{I_2+I_R}\right]^{\text{low density}}_{6P_{3/2}}=\frac{\epsilon_1\lambda_2}{\epsilon_2\lambda_1}\,\frac{R_{21}}{\Gamma_2}\left[\frac{1+(\Gamma_2/\Gamma_c)}{1+(\Gamma_R/\Gamma_c)}\right], \tag{12}$$

These expressions are linear in cesium density over the range of temperatures where Γ_2 is independent of density, and amount to neglect of the back-transfer terms. The first term within the square brackets in Eq. (11) represents the mixing which occurs in the $6P$ levels, while the second term represents the $5D$ level mixing (Γ_{31}/Γ_3 is simply a radiative branching factor). The term in large parentheses on the right-hand side of Eq. (12) represents the effects of the Rayleigh scattering. It can be seen that this term becomes equal to unity when $\Gamma_R=\Gamma_2$, which occurs in the optically thin case where $\Gamma_2=\Gamma_R=\Gamma_N$, but also when trapping of the Rayleigh scatter is comparable to that of the fluorescence (i.e., for excitation on resonance). When it is justified to replace this bracket by unity, a particularly simple result can be obtained for the

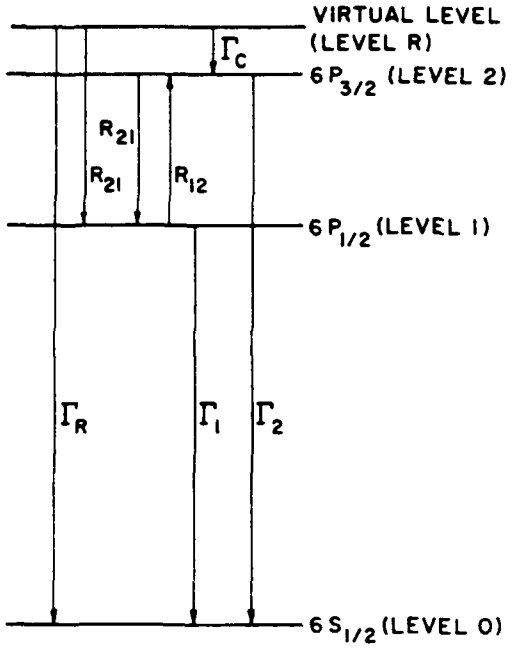

FIG. 3. Simplified model used for constructing the rate equations (7) and (8). The level "R" is a virtual level populated by the laser. See text for a complete description.

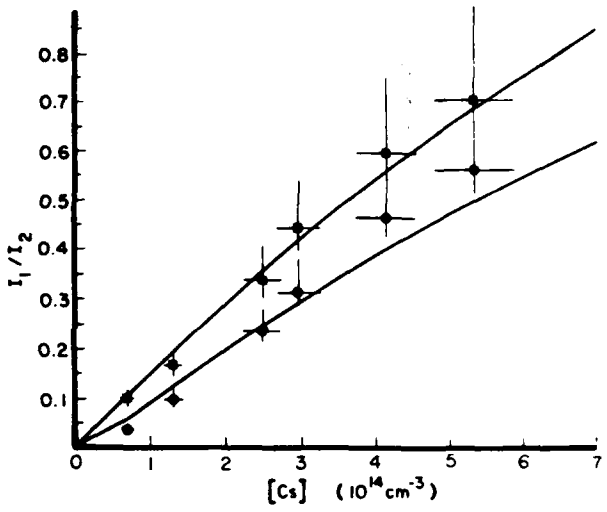

FIG. 4. Plot of $(I_1/I_2)_{5D_{5/2}}$ and $[I_1/(I_2+I_R)]_{6P_{3/2}}$, represented by squares and circles, respectively, vs cesium density. The solid curves are least-squares best fits of Eqs. (6) and (10) to the data. Error bars have been given for each point.

$5D_{5/2} \rightarrow 5D_{3/2}$ mixing rate,

$$R_{43} = k_{43}[\mathrm{Cs}] = \frac{\Gamma_4 \Gamma_3}{\Gamma_{31}} \frac{\epsilon_2 \lambda_1}{\epsilon_1 \lambda_2} \left[\left[\frac{I_1}{I_2} \right]_{5D_{5/2}} - \left[\frac{I_1}{I_2 + I_R} \right]_{6P_{3/2}} \right], \quad (13)$$

where [Cs] is the cesium atom density and k_{43} is the mixing rate coefficient. In this form it is easy to see that taking measurements using the two different pumping schemes allows a straightforward subtraction of the effects of $6P$ state mixing.

Figure 4 shows a plot of our measured values of

$$\left[\frac{I_1}{I_2} \right]_{5D_{5/2}}$$

and

$$\left[\frac{I_1}{I_2 + I_R} \right]_{6P_{3/2}}$$

versus cesium density. As can be seen, most of our data is within the linear regime. Nevertheless, the back-transfer terms cannot be ignored without introducing errors of the order of 30%, so that Eqs. (6) and (10) were used for the analysis. The procedure was to carry out a least-squares fit of Eq. (10) to our measured values of $[I_1/(I_2+I_R)]_{6P_{3/2}}$ versus cesium density. This yielded a best value for $k_{21}/\Gamma_2 \equiv R_{21}/(\Gamma_2[\mathrm{Cs}])$. This value was in turn used in a least-squares fit of Eq. (6) to our measurements of $(I_1/I_2)_{5D_{5/2}}$ versus density.

The only difficulty which remained to be overcome in order to carry through this procedure was to obtain values for Γ_R/Γ_c and Γ_2/Γ_1 to use in Eq. (10). Now $\Gamma_R < \Gamma_N = 3.26 \times 10^7$ sec^{-1} (from Ref. 27) and $\Gamma_c = 7.51 \times 10^{-7}$[Cs] (from Ref. 28). Therefore, over the density range of our experiment, 7×10^{13} to 6×10^{14} cm^{-3}, the Γ_R/Γ_c term contributes between 7% and 62% to the denominator of Eq. (10). In fact, Γ_R can be estimated reasonably accurately since the diode-laser frequency was set to maximize the sensitized fluorescence signal at 894.3 nm. This maximum occurs approximately when the laser power absorbed in the observation region is maximized. This point is found by maximizing the function $I_0(e^{-k_\nu L} - e^{-k_\nu(L+\Delta L)})$ with respect to k_ν, which is the absorption coefficient at frequency ν. I_0 is the incident intensity, and the observation zone extends from L to $L+\Delta L$ with respect to the entrance window. The laser detuning which peaks the fluorescence will be such that

$$k_\nu = (\Delta L)^{-1} \log_e[(L+\Delta L)/L] .$$

For our typical values of L and ΔL we find $k_\nu \sim 0.31$ cm^{-1}. The escape probability at this frequency is $e^{-k_\nu R}$ where R is the cell radius. Thus $\Gamma_R \sim \Gamma_N e^{-k_\nu R} \sim 2.36 \times 10^7$ s^{-1} at all densities. Γ_2/Γ_1 can be calculated accurately from the Holstein theory of radiation trapping[24,25], which has been verified for similar situations in sodium.[29,30] Thus we obtain $\Gamma_2/\Gamma_1 = 0.993$, independent of density. Note that because the trapped radiative rates depend critically on the excitation and detection geometry as well as on the atom density, it is crucial that both the diode- and dye-laser experiments be carried out with identical geometries (see also Sec. IV). Under these conditions, Γ_2 and Γ_1 will be independent of the state that is pumped. Note also that Γ_2/Γ_c can always be neglected in Eq. (10) under our conditions.

IV. RESULTS

Finally, from the least-squares fit of the $(I_1/I_2)_{5D_{5/2}}$ data and radiative rates from Ref. 27 we obtain our best value of k_{43}, which is the thermally averaged rate coefficient at $T \sim 425$ K,

$$k_{43} = 2.6 \times 10^{-10} \text{ cm}^3 \text{ s}^{-1} \pm 40\% \ . \tag{14}$$

Using the mean thermal velocity

$$\bar{v} = \left| \frac{8RT}{\pi} \frac{M_1 + M_2}{M_1 M_2} \right| \sim 3.67 \times 10^4 \text{ cm s}^{-1}$$

we can calculate an average cross section defined by

$$\sigma_{43} \sim k_{43}/\bar{v} = 70 \text{ Å}^2 \pm 40\% \ . \tag{15}$$

Before proceeding to a discussion of these results a few additional comments concerning radiation trapping, Rayleigh scatter, and quenching are required, followed by a short discussion about the uncertainty estimates.

A. Radiation trapping and Rayleigh scatter

Radiation trapping in alkali vapors has been studied extensively in recent years.[29,30] These studies have shown that the Holstein theory[24,25] gives accurate analytic expressions for effective radiative decay rates under certain well-defined circumstances. However, trapping is very sensitive to geometry and care must be exercised when applying the Holstein theory to actual experiments. Not only is the cell geometry important, but so too is the excitation and detection geometry.

In our experiment the cesium densities were sufficiently high that the Holstein pressure-broadening limit was always appropriate, and the theory yields $6P \rightarrow 6S$ radiative decay rates $\Gamma_{\text{eff}} \sim 8 \times 10^4$ sec^{-1} independent of density.[29] This decay rate corresponds to a "fundamental-mode" excitation scheme which is realized with an unfocused laser beam roughly filling the cell cross section. Use of focused laser beams as in this experiment results in longer decay times or slightly smaller decay rates. Nonetheless, Γ_{eff} should be approximately constant with density so that k_{21}/Γ_2 should be constant. The approximate linearity of the $[I_1/(I_2+I_R)]_{6P_{3/2}}$ data in Fig. 4 demonstrates that this is reasonable. We have found two previous measurements of the $6P_{3/2}+6S \rightarrow 6P_{1/2}+6S$ cross section.[31,32] Bunke and Seiwert[31] obtained $\sigma_{21} = 13$ Å^2, while Czajkowski and Krause[32] obtained $\sigma_{21} = 31$ Å^2. Using these two values in our expression for $k_{21}/\Gamma_2 = 1.40 \times 10^{-15}$ cm^3 obtained from the fit of the $[I_1/(I_2+I_R)]_{6P_{3/2}}$ data in Fig. 4, we obtain $\Gamma_2 \sim 3.4 \times 10^4$ and 8.1×10^4 s^{-1}, respectively. Thus we can conclude that the trapping problem is being handled in a reasonable fashion. However, our calculation of Γ_2 under these conditions is not sufficiently precise to establish a preference for one or the other previous values of σ_{21}.

The measured intensity ratios are also sensitive to detection geometry. Photons take longer to diffuse to locations further from the laser axis, and therefore the probability that a fine-structure-level-changing collision has occurred is also greater further out. Thus I_1/I_2 increases with offset of the detection region from the laser axis. However, as long as the $5D \rightarrow 6P$ fluorescence remains untrapped, and the diode- and dye-laser beams follow the same path, the value of k_{43} obtained from our measurements should be independent of detection position.

During the course of our measurements we realized that detection of light from a strip-shaped region perpendicular to the laser beams would result in intensity ratios that were far less sensitive to small offsets between the two beams. Only our data taken using this detection scheme are plotted in Fig. 4. Earlier data taken when we imaged a strip oriented along the laser beams must be fit using a smaller value of k_{21}/Γ_2 (since Γ_2 was larger). Nevertheless, the less accurate value of k_{43} obtained from these earlier data is consistent with our reported value from the later measurements to within combined error bars.

Although the $5D \rightarrow 6P$ fluorescence is produced by pumping a forbidden transition with a weak cw laser, it is important to verify that the slight radiation trapping on these transitions is not effecting our results. To do this we must first calculate the $6P_j$ level populations corresponding to the case of dye-laser pumping. The $6P$ populations can be obtained in the diode-laser case from the known laser power absorbed; i.e.,

$$n_{6P} = (P/h\nu)/(\Gamma_{\text{eff}} V_{\text{eff}}) \ .$$

Here $P = P_0(1 - e^{-k_\nu L})$ is the laser power absorbed in the cell of length L, and V_{eff} is the "trapping volume." We have already shown that $k_\nu \sim 0.31$ cm^{-1} for diode-laser pumping and $\Gamma_{\text{eff}} \sim 8 \times 10^4$ s^{-1} for all cesium densities studied. We use $V_{\text{eff}} \sim \pi r_{\text{eff}}^2 L$ with $r_{\text{eff}} = 0.3$ cm. This value, which represents the spatial extent of the $6P$ atoms, is intentionally small in order to calculate a maximum $5D \rightarrow 6P$ trapping effect. In this way we obtain $6P$ atom densities of $\sim 2.6 \times 10^{11}$ cm^{-3} with diode-laser pumping. The $6P_j$ level populations with dye-laser pumping are obtained by comparing the $6P_j$ level fluorescence with that obtained using the diode laser. In this manner, we obtain a maximum $6P_{3/2}$ density of 2.7×10^{10} cm^{-3} using the dye laser. We then used these calculated $6P_j$ densities to determine trapping factors from the Milne theory,[33] which has been shown to provide accurate values in the low-optical-depth case.[34] The $6P$ density is maximum for the highest cesium density where our calculation yielded a trapping correction of 22%. Note that this is a worst case (other data points are affected by substantially smaller amounts), and that the calculation was carried out using approximations that deliberately overestimated the effect.

Although the calculation above provides an upper limit to the effects of $5D \rightarrow 6P$ fluorescence trapping, we were able to show experimentally that such effects could be neglected under our conditions. We measured I_1/I_2 as a function of laser power for both diode- and dye-laser pumping. Each component is linear in laser intensity and therefore the ratios are obviously independent of intensity. Since $5D \rightarrow 6P$ trapping decreases with decreasing in-

tensity, it is clear that any effect this trapping might have on our results is small, in agreement with the preceding calculation. For these reasons, no attempt was made to correct our results for $5D \rightarrow 6P$ trapping.

We indicated in Sec. III how the radiative rate appropriate to Rayleigh scatter could be estimated, and how this value was approximately independent of density because the diode laser frequency was always set to maximize the sensitized fluorescence. In general, errors in Γ_R are not critical since $\Gamma_R/\Gamma_c \lesssim 0.25$ for $[\mathrm{Cs}] > 1.25 \times 10^{14}$ cm^{-3} where most data was taken. However, the Rayleigh scatter is also partially polarized and is therefore anisotropic. Additionally, the fluorescence is anisotropic due to trapping. The detection system was made equally sensitive to both polarizations as described in Sec. II, and the anisotropies calculated as described in Refs. 4 and 26. For Rayleigh scattering and fluorescence, the enhancement of intensity in the detection direction (relative to an isotropic distribution) is 18% and 14–27 %, respectively, and therefore the two effects almost cancel. We estimate that these effects (which we did not correct for) bias our results by less than 10%.

Intensities were always recorded for both the vertical and horizontal polarizations. In all cases reported intensities represent the sum of these two components.

B. Quenching

Quenching terms have been neglected in Eqs. (6) and (10) despite fairly large quenching rates reported for higher D levels.[1,35,36] This is because the $5D$ and $6P$ levels are quite isolated (each is more than 2700 cm^{-1} away from the nearest level). Thus quenching by ground-state cesium atoms, where the excitation energy can only couple to translational motion, should be negligible in this case where $kT \lesssim 300$ cm^{-1}. The fact that the data can be well fit without quenching terms is indicative that this approximation is justified.

Quenching by Cs_2 molecules in processes such as

$$Cs_2(X\,^1\Sigma_g^+) + Cs(6P,5D) \rightarrow Cs_2^* + Cs(6S) \qquad (16)$$

(where Cs_2^* is an excited molecule) must be considered since the rate coefficients can be almost gas kinetic [$k \sim 3\times 10^{-9}$ cm^{3}s^{-1} for the analogous process in Na_2 (Ref. 37)]. However, for $T = 225$ °C, which is roughly the highest temperature at which we took data, $[Cs_2]$ is only 10^{13} cm^{-3} according to the Nesmeyanov relation.[38] Thus quenching by Cs_2 molecules could not compete with radiative decay from the $5D$ levels. Due to trapping, radiative decay from the $6P$ levels is slower, but still the quenching terms remain insignificant over our range of temperatures. Even at higher temperatures, $6P$ state quenching would affect both laser-pumping situations equally and would therefore effectively cancel.

Excited-atom–excited-atom collisions such as

$$Cs(5D_{3/2}) + Cs(6P_{1/2}) \rightarrow Cs(8P_{3/2}) + Cs(6S)\,, \qquad (17)$$

which is out of resonance by only 17 cm^{-1}, and collisions involving two $6P$ atoms must also be considered here, even though we are pumping with a weak cw laser. Such collisions could change the $5D$ and $6P$ atom decay rates or change the fluorescence ratio I_1/I_2 through cascade contributions. Contributions from these effects can be calculated using the $6P_J$ level populations obtained in Sec. IV A on radiation trapping. $5D$ level populations are smaller than those of the $6P$ levels by the ratio $\Gamma_{6P\,\mathrm{eff}}/\Gamma_{5D}$. Using an extreme value for the excited-atom–excited-atom collision cross section of 10^{-13} cm^2, we can show that the fluorescence ratio I_1/I_2 cannot change by more than 10% except for diode-laser pumping at the lowest cesium density studied. For this one point the effect could be 20%. However, these calculation assume the very large excited-atom–excited-atom cross section given above, and that all more highly excited atoms produced by such processes cascade down through the $6P$ levels. For dye-laser pumping, excited-atom populations are substantially smaller than in the diode-laser case and all such effects can be shown to be negligible.

Just as in the case of $5D \rightarrow 6P$ fluorescence trapping, a calculation is used to provide an upper limit to the effect of excited-atom–excited-atom collisions. However, laser power dependences give experimental verification that these processes can be neglected here. In particular, we observe that all signals are linear in laser power, whereas any contribution from excited-atom–excited-atom collisions would scale quadratically.

Finally, since we are using sealed cells, we must worry about quenching by impurities; especially diatomic molecules. We can immediately state that any such effects are small, since we can calculate the $6P$ state decay rates from our measured fluorescence ratios and the known values of the $6P_{3/2} + 6S \rightarrow 6P_{1/2} + 6S$ cross section.[31,32] These values are in good agreement with decay rates obtained from radiation-trapping theory. In fact, the $6P$ state decay rates calculated from our data clearly provide an upper limit to the quenching rates. Note that quenching of $6P$ levels by impurities will not affect our results in any event, as long as the quenching is the same for both excitation conditions. If we assume similar quenching cross sections for the $5D$ levels we then establish that the relatively short $5D$ state lifetime is affected by less than 10% due to quenching. In addition, we can argue against quenching by permanent gases in the cell, since such gases would also cause fine-structure-level mixing which would result in nonzero y axis intercepts in Fig. 4. Quenching by species that outgas from the cell walls when they are heated is a more difficult effect to eliminate from consideration. The densities of such gases would probably scale differently with temperature than that of cesium, and thus probably could be detected by significant nonlinearity of the data of Fig. 4. To experimentally test for effects of impurities, we had a second sealed quartz cell made commercially. We observed no systematic differences in fluorescence ratios measured in the two cells. Since it is unlikely that impurity concentrations would be the same in the two cells, it seems reasonable to conclude that impurities cause no significant quenching in either cell.

C. Determination of cesium density

The cesium-atom number density was measured directly using the absorption-equivalent-width technique on both the $6S_{1/2} \rightarrow 6P_{1/2}$ and $6S_{1/2} \rightarrow 6P_{3/2}$ transitions. Since we operated in the pressure-broadening limit, we used the self-broadening rate Γ_c calculated by Carrington *et al.*[28] These calculations for $J = \frac{1}{2}$ to $J = \frac{1}{2}, \frac{3}{2}$ transitions were found to be accurate to within 15% experimental uncertainties in the analogous Na case.[4] Densities obtained from equivalent widths were self-consistent and agreed with those obtained from the Nesmeyanov vapor pressure formula to within about a factor of 2. This discrepancy is not considered significant since the vapor-pressure technique is notoriously unreliable for determining alkali densities. In particular, this technique may suffer from serious errors in the vapor-pressure formula itself, or the temperature measured may not be that of the coldest point in the cell. The equivalent-width technique is a direct measurement which only depends on well-known line-broadening parameters. Thus we believe that densities determined from equivalent width measurements are more reliable than those obtained from vapor-pressure formulas and, in particular, are less likely to suffer from systematic errors.

D. Uncertainties

An estimate of the uncertainty in our measured rate coefficient can be obtained by looking at Eqs. (10) and (6). Starting with Eq. (10), we estimate that the ratio of detection efficiencies is accurate to $\sim 5\%$, while the uncertainty in Γ_2/Γ_1 from the Holstein theory is probably on the order of 10%. Since the $6P_{3/2} + 6S \rightarrow 6P_{1/2} + 6S$ excitation-transfer process is exothermic by 554 cm^{-1}, which is not small compared to $kT \sim 300$ cm^{-1}, there will not in general be a Boltzmann velocity distribution in the $6P_{1/2}$ state. Therefore

$$\alpha_1 \equiv (g_2/g_1) e^{-(E_2 - E_1)/kT}$$

in the back-transfer term should be described by an effective temperature rather than the cell temperature. Since we have no reasonable method for estimating this effective temperature, which is also a function of atom density, we use the cell temperature to compute α_1 but assign it a relatively large uncertainty of a factor of 2. We consider this to be a conservative overestimate of the error since the 554 cm^{-1} heat liberated in the collision will be shared by the two colliding atoms, and additional thermalizing collisions will further reduce the effective temperature. Since the cell temperature is a lower bound on the effective temperature in α_1, the assigned uncertainty in α_1 is (+100%, −0%). This is the cause of the asymmetry in our error bars in Fig. 4.

The Rayleigh term Γ_R/Γ_c involves both the broadening rate and our calculation of the trapping at the diode-laser frequency. Thus we estimate the uncertainty in this term at $\sim 20\%$. Finally the fluorescence ratio itself is accurate to $\sim 5\%$. We assign a random error of 10% to our determination of the cesium density (the systematic error in this quantity could be more like 20%). In this way we assign an overall statistical error to each measured value of $[I_1/(I_2 + I_R)]_{6P_{3/2}}$ in Fig. 4. These are shown as error bars in both x and y for each point in Fig. 4.

The value of k_{21}/Γ_2 obtained from our fitting routine has a statistical error of 4%. We use this uncertainty in Eq. (6) and estimate the errors in α_1, Γ_2/Γ_1, ϵ_1/ϵ_2, and the measured fluorescence ratio as before. α_2 is probably accurate to 10% since the $5D$ state fine-structure splitting is only about $0.3kT$. Γ_4 and the Γ_3's were taken from Warner,[27] and we estimate them to be accurate to $\sim 10\%$. Ratios of the Γ's are expected to be much better. We thus obtain an overall error for each $[I_1/I_2]_{5D_{5/2}}$ point. Our fitting procedure then yields an uncertainty of $\sim 40\%$ in k_{43}. We believe this is sufficiently large to also account for the systematic errors in the density determination and the relative detection efficiency, etc.

V. DISCUSSION

The cesium $5D_{5/2} \rightarrow 5D_{3/2}$ fine-structure-level-changing collision rate coefficient reported here (2.6×10^{-10} $cm^3 s^{-1}$) is significantly larger than the upper limit obtained from the work of Wu and Huennekens[21] (10^{-11} $cm^3 s^{-1}$), and somewhat larger than the value 6.2×10^{-11} $cm^3 s^{-1}$ obtained by Davanloo *et al.*[22]

In the experiment of Wu and Huennekens, cesium molecules were pumped with fixed frequency lines from an argon-ion laser. Some of the excited molecules then predissociated or collisionally transferred excitation to produce excited atoms in the $5D_{5/2}$ and $5D_{3/2}$ levels. The $5D$ level populations were then detected by monitoring the quadrupole-allowed $5D \rightarrow 6S$ fluorescence. At all temperatures studied (representing cesium densities up to 10^{17} cm^{-3}), the ratio of $5D_{5/2} \rightarrow 6S$ fluorescence to $5D_{3/2} \rightarrow 6S$ fluorescence was approximately 2:1. However, the expected thermal equilibrium fluorescence ratio is 1.1:1. To verify that the discrepancy did not result from incorrect transition probabilities, the experiment was also carried out in a cell containing $\frac{1}{2}$ atm. of neon buffer gas. In this case the ratio of 1.1:1 was obtained. The implication of these results is that the collisional mixing rate $R_{43} = k_{43}[\mathrm{Cs}]$ is less than the radiative rate $\Gamma_4 = 8.4 \times 10^5$ s^{-1} for $[\mathrm{Cs}] < 10^{17}$ cm^{-3}. This yields the upper limit given above. In the present work we also observed the $5D$ quadrupole transitions following pumping of the cesium vapor with the argon-ion laser lines 488 and 514 nm in order to verify the previous results in our cell and under our experimental conditions. Again we saw the fluorescence ratio of 2:1 reported by Wu and Huennekens. At present, we are at a loss to reconcile the 2:1 fluorescence ratio (independent of density) with our current measurements of the $5D$ fine-structure mixing.

Davanloo *et al.*[22] obtained a value for the $5D$ state fine-structure mixing rate coefficient of 6.2×10^{-11} $cm^3 s^{-1}$. This measurement also involved pumping of cesium molecules and observing dissociation to the $5D$ levels. in this case, however, the excitation was with a high-power, pulsed laser. The $5D_J$ level populations as a function of time were monitored by using a second (de-

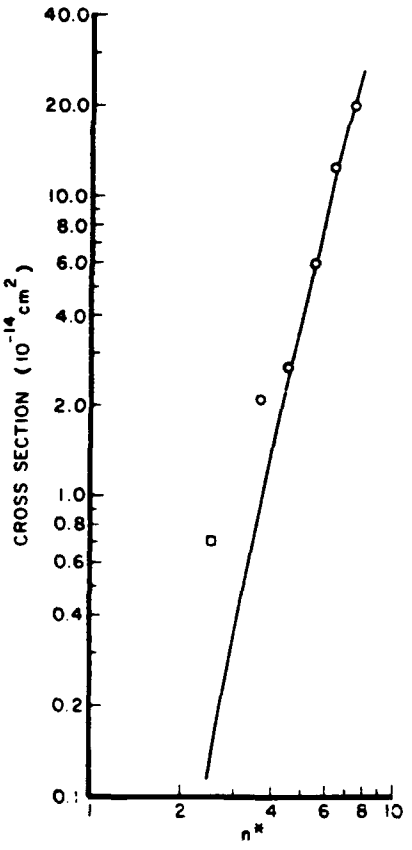

FIG. 5. Plot of cross sections for the fine-structure-level-changing collisions $Cs(nD_{5/2})+Cs(6S)\rightarrow Cs(nD_{3/2})+Cs(6S)$ vs effective principal quantum number n^*. The data for $n=6-10$ (circles) are taken from Ref. 1, while the $n=5$ case (square) is from the present work. The solid line is a plot of r^2 from Eq. (18).

layed) pulsed laser to pump to high-lying Rydberg F levels that would subsequently field ionize. The high intensity of the two pulsed lasers can cause several nonlinear processes to occur, including stimulated emission on the $5D\rightarrow 6P$ transitions, various wave-mixing processes, etc. (which are not likely in the low-power cw measurements). These types of processes could rapidly depopulate the $5D$ levels in a manner that might be indistinguishable from quenching. Thus such nonlinear processes may be the cause of the larger apparent quenching rate determined in the pulsed experiment.[22]

Figure 5 shows a log-log plot of the fine-structure changing cross sections σ_{43} as a function of effective principal quantum number n^*. This figure is the same as Fig. 4 of Ref. 1, except that our result for the $5D$ levels has been added. The data for the $6D-10D$ states is that of Tam *et al.*[1] The geometric cross section can be approximated by the hydrogenic expectation value of the square of the orbit radius given by[39]

$$r^2=\tfrac{1}{2}n^{*2}[5n^{*2}+1-3l(l+1)]a_0^2 . \tag{18}$$

Tam *et al.* found that for $n=7-10$, $\sigma_{43}\approx r^2$, while for $n=6$ the cross section was 2.6 times larger than r^2. Equation (18) is plotted in Fig. 5 as a solid curve. For the $5D$ levels, where $n^*\approx 2.55$, we calculate $r^2=14$ Å^2. Our measured value is about 5 times larger. Thus our current measurement seems consistent with the trend shown by the $6D$ mixing rate.

VI. CONCLUSIONS

In this paper we have reported an experimental value for the $Cs(6S)+Cs(5D_{5/2})\rightarrow Cs(6S)+Cs(5D_{3/2})$ fine-structure-level-changing collisional rate coefficient. The measurement was carried out by pumping the one-photon quadrupole-allowed $6S\rightarrow 5D_{5/2}$ transition, and monitoring the cascade $(6P_{1/2}\rightarrow 6S)/(6P_{3/2}\rightarrow 6S)$ fluorescence ratio. Since mixing can also take place between the $6P$ fine-structure levels, a second experiment was carried out in which the $6P_{3/2}$ level was pumped and the same fluorescence ratio measured. This process allowed a rather direct correction for the effects of radiation trapping and collisional mixing in the $6P$ levels. The value we obtained for the $5D$ state mixing cross-section in the present work is approximately 4 times larger than the value reported by Davanloo *et al.*[22] and 25 times larger than the upper limit that can be derived from the results of Wu and Huennekens.[21] We have presented some possible explanations for the discrepancies with the pulsed measurements. However, at present, we are unable to reconcile our present $5D$ fine-structure mixing cross section with the argon-ion-laser data.

ACKNOWLEDGMENTS

We are grateful to S. McClain and E. Rothenheber who worked on this experiment in its preliminary stages, and to Dr. Will Happer and Dr. Frank Feigl for loans of several key pieces of equipment. This work was supported by the National Science Foundation under Grant No. PHY-8451279 and the Army Research Office under Grant No. DAAL03-86-K-0161.

[1] A. C. Tam, T. Yabuzaki, S. M. Curry, M. Hou, and W. Happer, Phys. Rev. A **17**, 1862 (1978).
[2] J. Wolnikowski, J. B. Atkinson, J. Supronowicz, and L. Krause, Phys. Rev. A **25**, 2622 (1982).
[3] M. Harris and E. L. Lewis, J. Phys. B **15**, L613 (1982).
[4] J. Huennekens and A. Gallagher, Phys. Rev. A **27**, 1851 (1983).
[5] J. W. Parker, H. A. Schuessler, R. H. Hill, Jr., and B. G. Zollars, Phys. Rev. A **29**, 617 (1984).
[6] J. Supronowicz, J. B. Atkinson, and L. Krause, Phys. Rev. A **30**, 112 (1984).
[7] J. Supronowicz, J. B. Atkinson, and L Krause, Phys. Rev. A **31**, 2691 (1985).

[8]L. Sirko and K. Rosiński, J. Phys. B **18**, L221 (1985).
[9]L. Sirko and K. Rosiński, J. Phys B **19**, L279 (1986).
[10]L. Sirko and K. Rosiński, J. Phys. B **20**, L487 (1987).
[11]P. Munster and J. Marek, J. Phys. B **14**, 1009 (1981).
[12]B. G. Zollars, H. A. Schuessler, J. W. Parker, and R. H. Hill, Jr., Phys. Rev. A **28**, 1329 (1983).
[13]J. Pascale. J. M. Mestdagh, J. Cuvellier, and P. de Pujo, J. Phys. B **17**, 2627 (1984).
[14]R. Düren, E. Hasselbrink, and G. Hillrichs, Chem. Phys. Lett. **112**, 441 (1984).
[15]R. W. Berends, W. Kedzierski, and L. Krause, J. Quant. Spectrosc. Radiat. Transfer **37**, 157 (1987).
[16]J. M. Mestdagh, P. de Pujo, J. Pascale, J. Cuvellier, and J. Berlande. Phys. Rev. A **35**, 1043 (1987).
[17]L. Krause, in *The Excited State in Chemical Physics*, edited by J. W. McGowan (Wiley, New York, 1975), pp. 267–316.
[18]L. L. Vahala, P. S. Julienne, and M. D. Havey, Phys. Rev. A **34**, 1856 (1986).
[19]M. D. Havey, F. T. Delahanty, L. L. Vahala, and G. E. Copeland, Phys. Rev. A **34**, 2758 (1986).
[20]A. Ermers, T. Woschnik, and W. Behmenburg, Z. Phys. D **5**, 113 (1987).
[21]Z. Wu and J. Huennekens, J. Chem. Phys. **81**, 4433 (1984).
[22]F. Davanloo, C. B Collins, A. S. Inamdar, N. Y. Mehendale, and A. S. Naqvi, J. Chem. Phys. **82**, 4965 (1985).
[23]R. Stair, W. E. Schneider, and J. K. Jackson, Appl. Opt. **2**, 1151 (1963).
[24]T. Holstein, Phys. Rev. **72**, 1212 (1947).
[25]T. Holstein, Phys. Rev. **83**, 1159 (1951).
[26]J. Huennekens, Ph.D. thesis, University of Colorado, 1982
[27]B. Warner, Mon. Not. R. Astron. Soc. **139**, 115 (1968).
[28]C. G. Carrington, D. N. Stacey, and J. Cooper, J. Phys. B **6**, 417 (1973).
[29]J. Huennekens and A. Gallagher, Phys. Rev. A **28**, 238 (1983).
[30]J. Huennekens, H. J. Park, T. Colbert, and S. C. McClain, Phys. Rev. A **35**, 2892 (1987).
[31]H. Bunke and R. Seiwert, *Optik u. Spektroskopie aller Wellenlängen* (Akademie Verlag, Berlin, 1962).
[32]M. Czajkowski and L. Krause, Can. J. Phys. **43**, 1259 (1965).
[33]E. Milne, J. London Math. Soc. **1**, 40 (1926).
[34]B. P. Kibble, G. Copley, and L. Krause, Phys. Rev. **153**, 9 (1967).
[35]J. S. Deech, R. Luypaert, L. R. Pendrill, and G. W. Series, J Phys. B **10**, L137 (1977).
[36]S. Nakayama, M. Kelly, and G. W. Series, J. Phys. B **14**, 835 (1981).
[37]L. K. Lam, T. Fujimoto, A. C. Gallagher, and M. M. Hessel, J. Chem. Phys. **68**, 3553 (1978).
[38]A. N. Nesmeyanov, *Vapor Pressure of the Elements* (Academic, New York, 1963).
[39]H. Bethe and E. E. Salpeter, Handb. Phys. **35**, 88 (1957).